Universitat Ramon Llull

# DOCTORAL THESIS

| | |
|---|---|
| Title | Development of Novel and Multifunctional Polymeric Nanoparticles for Brain Targeted Drug Delivery |
| Presented by | Primiano Pio Di Mauro |
| Centre | IQS School of Engineering |
| Department | Bioengineering |
| Directed by | Dr. Salvador Borrós |

*C. Claravall, 1-3*
*08022 Barcelona*
*Tel. 936 022 200*
*Fax 936 022 249*
*E-mail: urlsc@sec.url.es*
*www.url.es*

## Summary

Controlled release systems have become an innovative technique to treat diseases like cancer by the targeted delivery to individual cells and tissues. There is an urgent need to achieve efficacious and safe delivery with minimal nonspecific uptake by healthy tissues. Among the polymer-based nanoparticulate systems for drug delivery, nanoparticles (NPs) have represented a promising opportunity as delivery system due to their degradation in water-soluble compounds that enter the normal metabolic pathways of the organism and their capacity to modify pharmacokinetics and the drug tissue distribution profile.

An engineered and versatile targeted nano-platform for the delivery of paclitaxel (PTX) across the blood brain barrier (BBB) with the aim to improve its therapeutic effect on human glioma cells has been developed. A novel biodegradable polymer has been synthetized and custom tailored NPs have been obtained. The method allows to modify the targeted drug delivery for efficiently transport and release of active drug molecule across the BBB. Aiming a dual-targeting strategy, functionalization with ligands known to be efficiently transported across BBB by a membrane receptor that also is over-expressed on human glioma cells has been employed to shuttle PTX from blood to brain and then target glioma cells. In vivo properties of the NPs have been explored to assess their biological profile and since the pressing need for careful evaluation, new strategies for NPs radiolabeling with the aim to investigate their in vivo fate, specifically stability in biological environments (stealthiness), biodistribution and pharmacokinetic, have been adopted.

## Resumen

Los sistemas de liberación controlada de medicamentos, mediante la administración dirigida individualmente a células y tejidos, se han convertido en una técnica innovadora para tratar enfermedades como el cáncer. Existe una necesidad urgente para lograr una liberación eficaz y segura que incluya una mínima absorción no específica para los tejidos sanos. Entre los sistemas nanopartículados a base de polímeros para la administración de fármacos, las nanopartículas (NPs) han representado una oportunidad prometedora como sistema de suministro. Entre sus ventajas se puede destacar su perfil de degradación en compuestos hidrosolubles y no tóxicos, que se eliminan siguiendo las vías metabólicas normales del organismo. Por otro lado, presentan una elevada capacidad de modificar la farmacocinética y el perfil de distribución del medicamento en los tejidos.

En esta tesis se ha desarrollado una nano-plataforma específica y versátil para la liberación de paclitaxel (PTX) a través de la barrera hematoencefálica (BHE) con el objetivo de mejorar su efecto terapéutico sobre las células de glioma humano.

Se ha sintetizado un nuevo polímero biodegradable gracias al cual se han obtenido NPs personalizadas a medida. El método permite modificar el tipo administración dirigida de los fármacos para conseguir un transporte y una liberación de las moléculas de principio activo eficiente y segura. Se ha desarrollado el objetivo de seguir una estrategia de selección dual que consiste en transportar el PTX desde la sangre hasta el cerebro y luego dirigirse a las células de glioma. Para ello se ha empleado la funcionalización con marcadores capaces de atravesar eficientemente la BHE a través de un receptor de membrana que también está sobre-expresado en las células de glioma humano. Para evaluar el perfil biológico de las NPs se han explorado sus propiedades in vivo y dada la urgente necesidad de una evaluación fiable, se han adoptado nuevas estrategias para radiomarcar NPs con el objetivo de investigar su destino in vivo, la estabilidad en entornos biológicos, la biodistribución y la farmacocinética.

# Table of Contents

# Index of Schemes



# Index of Figures

# Index of Tables



# Index of Equations

# List of Abbreviations

**15F:** 15F Peptide
**2P:** Block co-polymer 2P
**3P:** Block co-polymer 3P
**AA:** Amino Acids
**ABC:** Accelerated Blood Clearance
**AcOH:** Acetic Acid
**BBB:** Blood Brain Barrier
**BBMVECs:** Bovine Brain Endothelial Cells
**BCECs:** brain capillary endothelial cells
**CNS:** Central Nervous System
**CO2:** Carbon Dioxide
**CT:** Computed Tomography
**Cys:** Cysteine
**DLS:** Dynamic Light Scattering
**DMEM:** Dulbecco's Modified Eagle Medium
**DMF:** Dimethylformamide
**DMSO:** Dimethyl Sulfoxide
**DSC:** Differential Scanning Calorimetry
**EC:** Endothelial Cells
**EPR:** Enhanced permeability and retention effect
**EtOH:** Ethanol
**FBS:** Fetal Bovine Serum
**GBM:** Glioblastome Multiforme
**Hb:** Hemoglobin
**HCl:** Chlorhydric acid
**HPLC:** High Pressure Liquid Cromatography
**LDLR:** Low Density Lipoprotein Receptor
**LRP:** Lipoprotein Receptor-Related Protein
**LY:** Lucifer Yellow
**MALDI:** Matrix-assisted laser desorption/ionization
**MDR:** Multidrug Resistance
**MPEG:** Methoxy Poly (Ethylene Glycol)
**MS:** Mass Spectroscopy
**NMR:** Nuclear Magnetic Resonance
**NP:** Nanoparticles
**NTA:** Nanoparticle Tracking Analysis
**P*:** Prepolymer
**P:** Block co-polymer P
**PBS:** Phosphate Buffer Solution
**PCL:** Poly (ε-caprolactone)
**PEG:** Poly (Ethylene Glycol)
**PET:** Positron Emission Tomography
**PHA:** Polyhydroxyalkanoates
**PLA:** Polylactide
**PLGA:** Poly (lactide-co-glycolide)
**PTX**: Paclitaxel
**REG:** Regulon Peptide
**RES:** Reticuloendothelial System
**RI:** Refractive Index
**SLN:** Solid Lipid Nanoparticle
**TEER:** Trans-endothelial electrical resistance
**TEM:** Transmission Electron Microscopy
**TFA:** Trifluoroacetic Acid
**THF:** Tetrahydrofuran
**TLC:** Thin Layer Cromatography
**TOF:** Time of Flight
**Tyr:** Tyrosine
**UPLC:** Ultra Performance Liquid Cromatography
**UV:** Ultraviolet

# CHAPTER I.

## Introduction

## 1.1 Introduction

In the recent years, significant advances in the field of nanotechnology, especially in material science and medicine, have been achieved. In particular, the medical application of nanotechnologies, usually termed nanomedicine [1–5] has given a decisive impulse to the development of various types of drug-loaded nanocarriers, usually ranging from 1 to 1000 nm. An extensive variety of nanocarriers or nanoparticulate systems, composed of different materials including lipids, polymers and inorganic materials have been proposed in the biomedical field, resulting in delivery systems that depending on their physiochemical properties will be suitable for different applications (Scheme 1.1). In drug delivery technologies, nanocarriers are designed (i) to protect a drug from *in vivo* degradation; (ii) to enhance drug absorption by facilitating diffusion through epithelium; (iii) to modify pharmacokinetics and drug tissue distribution profile; (iv) to improve intracellular penetration and subcellular distribution. Furthermore, surface modification of pharmaceutical nanocarriers is normally used to control their biological fate in a desirable way. The most important results of such modification include an increased stability and half-life of nanocarriers in the circulation, passive or active targeting into the required pathological zone and responsiveness to local stimuli such as pathology-associated changes in local pH and/or temperature.

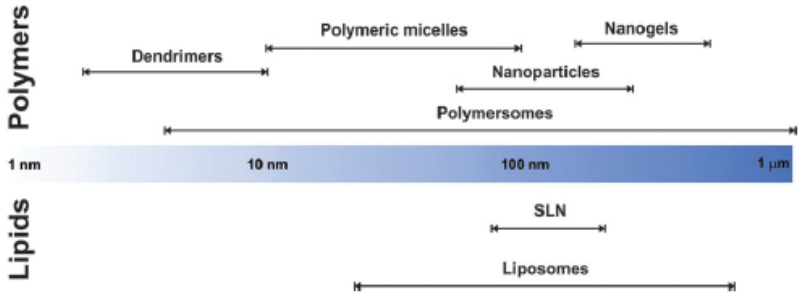


Scheme 1.1 Lipid and polymer-based nanoparticulate systems used in the field of drug delivery and active targeting [6]

The wide application of biodegradable polymers in this field is due to their degradation by chemical or enzymatic processes in water-soluble low molecular weight compounds that enter the normal metabolic pathways of the organism. The most used polymer-based nanoparticulate systems for drug delivery are nanoparticles (NPs), vesicles, polymeric micelles and nanoconjugates. (Scheme 1.2).

**Micelles** are self-assembling nanosized colloidal particles which form spontaneoulsy under certain concentrations and temperatures from amphiphilic or surface-active molecules, which consist of two clearly distinct regions with opposite affinities towards a given solvent. Hydrophobic segments of amphiphilic molecules form the core of a micelle, while hydrophilic fragments form the micelle shell. When used as drug carriers in aqueous media, micelles solubilize poorly soluble and non-polar molecules within the micelle core.[7]

**Polymersomes** are polymer-based vesicular shells that are formed upon hydratation of amphiphilic block copolymers. As the nanocapsules, polymersomes are indeed vesicular systems in which the drug is confined to a reservoir or within a cavity surrounded by a polymer coating. Accurate selection of polymer M, hydrophilic/hydrophobic ratio and chemistry impart polymersomes with a broad and tunable range of carrier properties. These systems are capable of encapsulating a large range of therapeutically water soluble active molecules and biomolecules.[8]

**Polymer–drug conjugates** are macromolecular system where a prodrugs is covalently bound to a water soluble polymeric carrier, normally via a biodegradable linker. Amphiphilic polymer-drug conjugates in aqueous solution can form micelles or micelle-like nanoassemblies in which the lipophilic drug is confined in the internal core of the system.[9]

Finally, **Nanoparticles** are solid colloidal systems in which the drug is physically dispersed, dissolved, or chemically bounded to the polymer chains.[10] Depending on the method employed for their preparation, nanospheres or nanocapsules can be obtained. Nanospheres are matrix-like systems in which the drug can be either entrapped inside the NPs or adsorbed on their surface. On the contrary, nanocapsules are vesicular systems

which are formed by a drug-containing liquid core, composed of oil or water depending on the encapsulated compound and surrounded by a single polymeric membrane[11].

Both types of NPs can be prepared from a variety of materials such as proteins, polysaccharides and synthetic biodegradable polymers, depending on many factors such as i) size of the desired NPs, ii) properties of the drug to be encapsulated (aqueous solubility, stability, etc.), iii) surface characteristics and functionality, iv) degree of biodegradability and biocompatibility, and v) drug release profile of the final product.

The methods to prepare NPs can be divided into two main categories depending on if the formulation requires a polymerization reaction or is obtained by preformed prepolymers. In the last year, due to the Food and Drug Administration (FDA) approval for human use, there has been a significant interest in employing synthetic polymers like poly(ethyleneglycol) (PEG) [12], polylactide (PLA)[13], and poly(D,L-lactide–co-glycolide)[14] (PLGA).

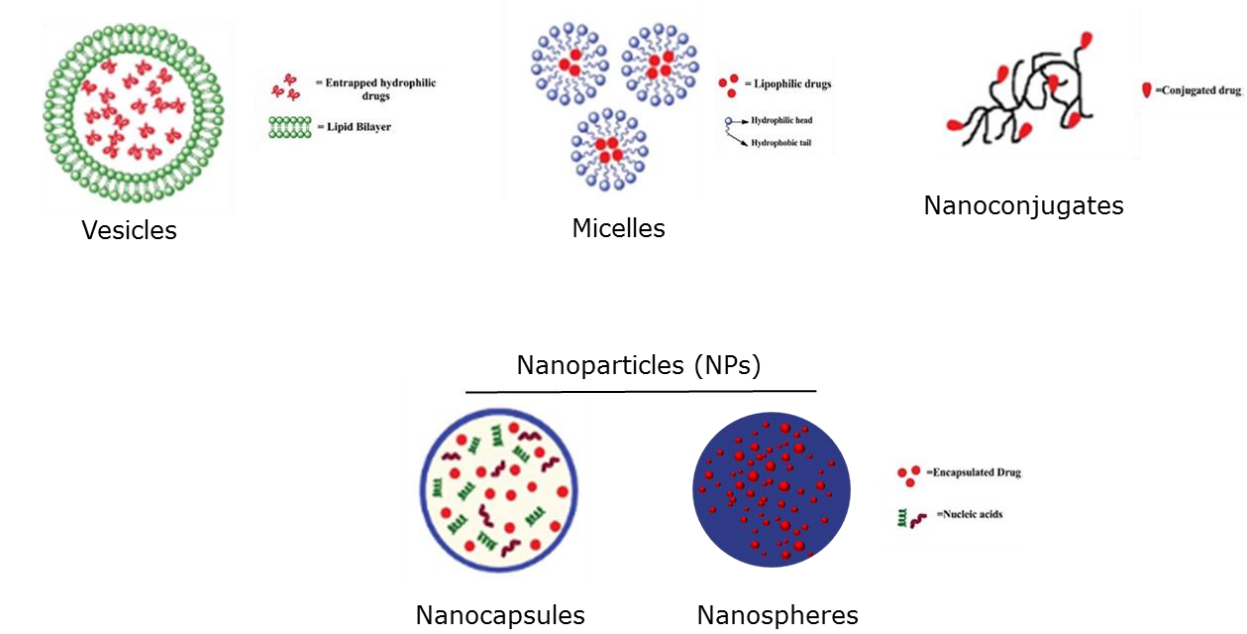


Scheme 1.2 Polymeric nanoplatforms for drug delivery[15]

Many of the described polymer-based nanoparticulate systems developed for solid tumor treatment, have proved to be efficacious cancer therapeutics[16]. Cancer in its myriad forms affects millions of people worldwide and is growing at an alarming rate to become the world's deadliest disease of all times.[17] With more than ten million people diagnosed annually, cancer is a major cause of mortality. It is known that cancer develops via a multistep carcinogenesis process involving numerous cellular physiological systems such as cell signaling and apoptosis, making it a highly complex disease.[18]

Treatment of brain cancer remains one of the biggest challenges in oncology. Anaplastic astrocytomas and glioblastoma multiforme (GBM) are the most aggressive brain tumors with median survival of patients of 24 and 9 months, respectively.[19] Moreover GBM is the most frequent primary central nervous system tumor, and represents the second cause of cancer death in adults less than 35 years of age.[20] Because of its aggressiveness, due to rapid proliferation, high angiogenic level and tendency to infiltrate the surrounding healthy tissues, it is impossible to make the complete removal of the tumor by surgical methods. Despite many advances in conventional treatment such as chemotherapy, surgery and radiation, cancer therapy is still far from optimal because it is plagued by some drawbacks. Challenges encountered by current cancer therapies are non-specific systemic distribution of antitumor agents, inadequate drug concentrations in the tumor site, limited ability to monitor therapeutic responses and development of MDR. The therapeutic effects of present chemotherapy for GMB treatments are very limited mainly because of the presence of the blood-brain barrier (BBB) that separates the blood from the cerebral parenchyma and functions as a tremendously effective barrier for the delivery of potential neurotherapeutics into the brain parenchyma.[21,22] Virtually, all large molecule drugs, more than 98% of small molecule candidate drugs and the majority of novel protein and peptide are unable to reach the brain tissue due to their poor permeability across the BBB.

The BBB is formed by brain endothelial cells that line the cerebral microvessels. It is supported by other cell types surrounding the endothelium, such as astrocytes and

pericytes (Figure 1.1).[23] These surrounding cells contribute to the induction of many barrier characteristics of the endothelium, such as tight junctions (Figure 1.1), which closely join the endothelial cells together. Next to being a "physical barrier", the BBB is also a "transport barrier", since it contains numerous transporter proteins and transcytosis mechanisms that mediate the uptake and efflux of molecules. Third, a "metabolic barrier" is formed by the expression of metabolizing enzymes such as peptidases, cytochrome P450 enzymes and monoamine oxidases.[24] All of these barrier functions control and regulate both inward and outward transfer of molecules between blood and the brain.

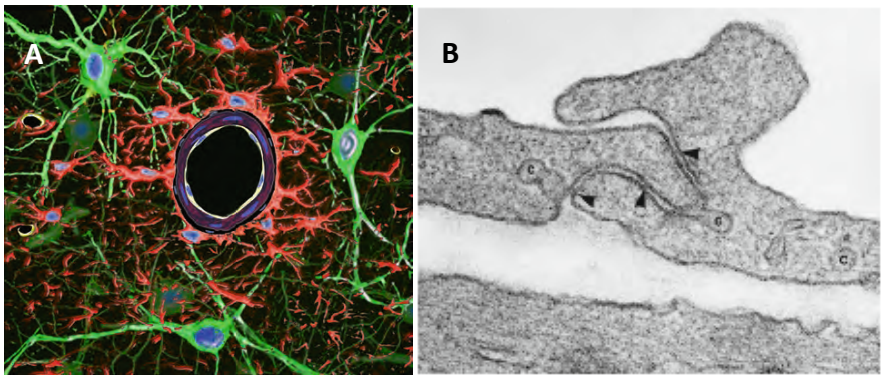


Figure 1.1 Neurovascular unit. (A) a modified merged confocal image of an arteriole consisting of endothelial and smooth muscle, surrounded by astrocytic processes (red) and some of the neuronal processes (green); (B) a segment of arteriolar endothelium shows tight junctions (arrowheads) along the interendothelial space[25]

There are several routes for the transport of molecules across the BBB (Scheme 1.3). Paracellular transport of hydrophilic molecules is highly restricted by the tight junctions between brain endothelial cells. Lipid-soluble molecules with relatively small molecular weight (<400 Da), adequate lipophilicity, neutral or uncharged nature, low hydrogen bonding potential and sufficiently high unbound plasma fraction are able to achieve passive transcellular lipophilic diffusion across endothelial cells of the BBB. For a variety of molecules that are essential for brain function, such as amino acids, glucose, peptides, and

proteins, specific endogenous BBB transporters exist. These are expressed at both the luminal and the basolateral membranes of the endothelium.[24] These transporters can be either defined as carriers or receptors. Carriers are membrane-restricted systems which are generally responsible for the transport of small molecules with a fixed size and mass smaller than 600 Da. Carrier-mediated transcytosis is used for the delivery of nutrients such as glucose, amino acids, and purine bases to the brain. This type of transport is substrate-selective, and only drugs that closely mimic the endogenous carrier substrates will be taken up.[26] On the other hand, receptor-mediated endocytosis is initiated by the binding of a receptor-specific ligand. Following binding, the substance is internalized and transported via the early endosome to the lysosome, or transcytosed to the plasma membrane.[26] The only way for larger molecules and particles such as antibodies, lipoproteins, proteins and NPs to be transported into the brain is via receptor mediated endocytosis.[27] Finally, endocytosis at the BBB can occur also through adsorption binding. Adsorptive-mediated endocytosis is initiated by the binding of polycationic substances to negative charges on the endothelial plasma membrane and the substance is internalized and transported. Next to these influx systems, many efflux mechanisms exist at the BBB, including P-glycoprotein, multidrug resistance (MDR)-related protein, ABC transporters, and several others.[28] They restrict entry of drugs virtually able to access the brain by promoting luminal release of compounds and are important in removing harmful substances from the brain. Substrates for efflux transporters include peptides, lipids, cholesterol, hormones, CNS drugs and metabolites.[29]

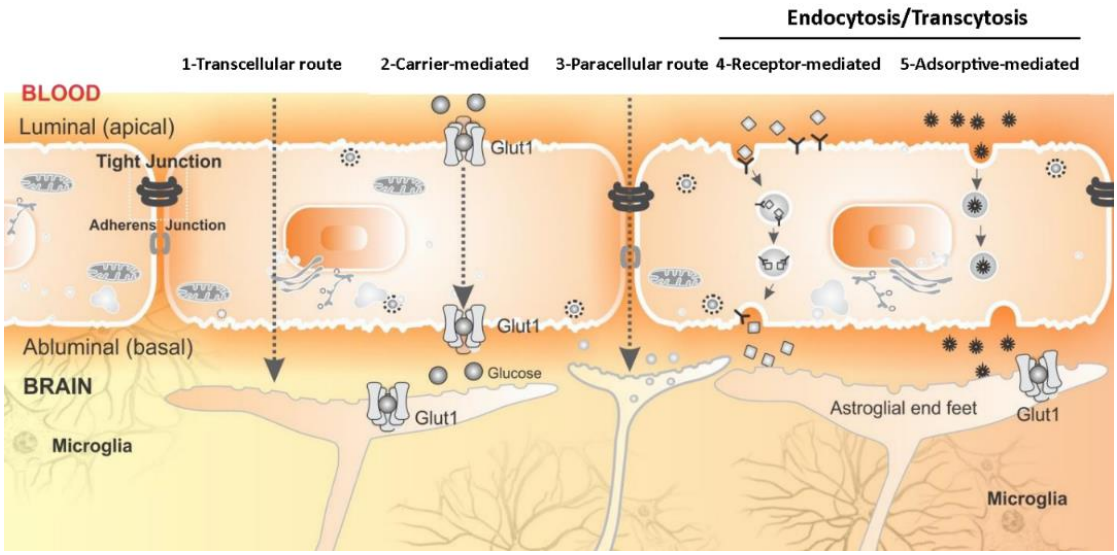


Scheme 1.3 Transport mechanism at the BBB site for shuttling of endogenous and/or exogenous substrates [30]

The use of the receptor-mediated transport, highly expressed on the BBB luminal side, have become an attractive strategy for drug design in attempt to shuttle drug molecules across the BBB. It is reported that various receptors are present on the luminal endothelial plasma membranes, including the transferrin receptor, the insulin receptor, endothelial grow factors receptor, and low-density lipoprotein receptor-related protein (LRP).[31] LRP, a member of the low-density lipoprotein receptor family (LDLR), is highly expressed on BBB [32] and mediate the transcytosis of multiple ligands across the BBB such as lactoferrin [33] and melanotransferrin. Moreover, LRP is also over-expressed on human glioma cells [34], making LRP a potential targeted receptor for brain tumor drug delivery systems, with dual-targeting capability for both BBB and glioma cells.

Although many advances in conventional treatments for cancer therapy, to make further progress it is necessary to put emphasis on other existing, but still under appreciated, therapeutic approaches. An increased interest is being focused on nanotechnological approaches in cancer treatment based on the concept that the therapeutic effects of

many anticancer drugs could be significantly improved if delivery of the drug occurred specifically to tumors, achieving a reduction of toxic side effects.[35] The key point to develop targeted drug delivery systems able to selectively recognize specific cells or tissues, can be found in the words of Paul Ehrlich, Nobel Prize for Medicine in 1908, who suggested the concept of "magic bullet": a drug that selectively destroys diseased cells but is not harmful to healthy cells.[36]

There has been intense interest in identifying polymeric NPs that are best suited for oncology applications. Nanoparticles carriers are capable of addressing several drug delivery problems, which could not be effectively solved in the past and include overcoming MDR phenomenon and penetrating cellular barriers that may limit drug accessibility to intended targets. Pharmacokinetics of the NPs is crucial and depends on several physiochemical characteristics of the carrier such as size, surface charge, shape, nature and density of coating, composition, stability, steric stabilization, dose and route of administration.[37,38]

Further advantages of NPs result from the ability to incorporate hydrophobic drugs at concentrations greater than their intrinsic water solubility[39], the possibilities to greatly modify their composition, their circulation time, the drug release profile and the target ability.[40] Nevertheless, multiple obstacles must be overcome in order to have an effective injectable drug delivery system.[41] The major challenges include overcoming clearance in the body and increasing the uptake into target tissue/cells. Natural elimination processes include both renal clearance and uptake by the Mononuclear Phagocyte System (MPS). Renal clearance of intravascular agents is a process involving glomerular filtration, tubular secretion and finally elimination of the molecule through urinary excretion. Filtration of particles through the glomerular capillary wall is highly dependent on molecule size and is referred to as the filtration-size threshold. Molecules with a diameter of less than 6 nm are typically filtered, while those bigger than 8 nm are not typically capable of undergo glomerular filtration.[42] MPS uptake proceeds quickly and must be avoided in order to have an acceptable circulation time for nanocarriers. The MPS, also referred to as the

reticuloendothelial system (RES), is the main natural clearance system for particles not filtered by the kidneys acting via phagocytosis. Recognition by the MPS is aided by opsonization, which consists in the binding of blood opsonins to nanocarriers' surface thus inducing its phagocytosis and accumulation in the liver (Kuppfer cells). The liver acts as a reservoir toward nanocarriers conditioning their rapid first-phase disappearance from the blood and, in case of biodegradable systems, their second-phase escape from the body under degraded and excretable form. In order to overcome the opsonization of nanocarriers, a number of widely used and effective methods have been investigated to make nanocarriers "invisible" to the immune system, creating long-circulating NPs, known also as stealth NPs. Interestingly, by coating the NPs surface with hydrophilic polymers, such as PEG, poloxamers, or hydrophilic polysaccharides, it is possible to create a hydrated water barrier that prevents the interaction with blood components and therefore the attack of phagocytes.[43,44] Furthermore, a steric stabilization limits also aggregation between particles themselves in the blood and contribute to system stability in biological environments. Stealth NPs exhibit decreased levels of uptake by the MPS and, consequently, a prolonged circulation time in the blood, and are able to accumulate in solid tumors passing through their leaky vasculature (*passive targeting)*. Indeed, all nanoparticles in general benefit from enhanced permeation and retention (EPR) that allows for passive tumor targeting.[45,46] The EPR effect (Scheme 1.4) describes the accumulation of NPs in tumor tissues, due to fenestrations in the blood vessel's endothelial layer and a significantly reduced lymphatic drainage in the tumor tissue.[47] Therefore, passive targeting mediated by the EPR effect is the most common mechanism used for the uptake of NPs or polymers at oncological target sites.[48,49] This explains why the PEGylation strategy appears to be a key nanotechnological advance, allowing PEGylated nanocarriers to exhibit a prolonged circulation time, thus leading to an increased opportunity to reach its site of action. Gref et al [50] were the first to report the advantages of PEGylation on PLGA-PEG NPs, resulting in a substantial increase in blood residence time. The chain length, shape, and density of PEG on the particle surface have been shown to be the main parameters affecting NPs surface hydrophilicity and

phagocytosis. Most research indicates that a PEG chain with molecular weight of 1500 Da or greater is required to achieve increased MPS-escape. This minimum MW is most likely due to the loss in flexibility of shorter PEG chains. Also, it has been shown that as molecular weight is increased, the blood circulation half-life of the PEGylated particles is also increased, which may be due in part to the increased chain flexibility of higher $M_W$ PEG polymers. In addition to chain molecular weight, surface chain density and conformation are also critical factors to achieve improved stealth characteristics, although these two aspects are much more interrelated.[51] A high surface coverage ensures that the entire surface of NP is covered but also decreases the mobility of the PEG chains and thus decreases the steric hindrance properties of the PEG layer.

On the basis of this scenario, the vast majority of nanomedicines developed for drug targeting to tumors rely on the EPR effect. These primarily include long-circulating liposomes, polymers and micelles. Examples of passively targeted nanomedicines approved for clinical use are Myocet®, Doxil®, Daunoxome®, Abraxane® and Genexol-PM®. Several additional passively tumor-targeted nanomedicines are currently in clinical trials, and a large number of other ones are in early- and late-stage of preclinical development.

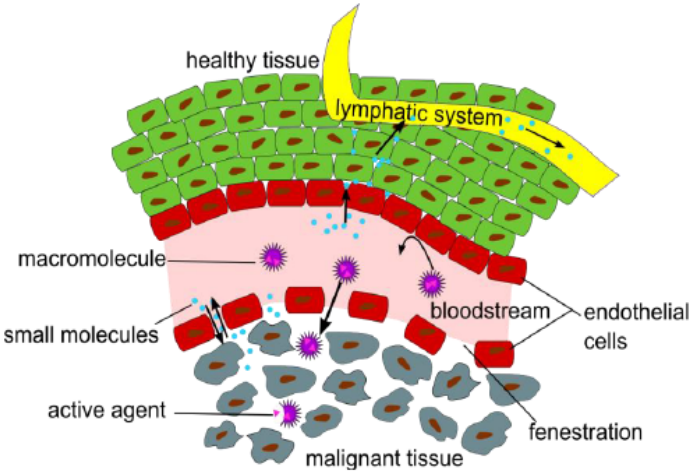


Scheme 1.4 Enhanced Permeation and Retention (EPR) effect of macromolecular structures as drug delivery systems in malignant tissue. [52]

Nevertheless, the EPR effect is not suited for all tumors because the degree of tumor vascularization and porosity of tumor vessels can vary with the tumor type and status. Moreover, the occurrence of the so-called "accelerated blood clearance (ABC) phenomenon" produced by PEGylation, explains the urgent need for nanoparticulate systems able to serve as efficient therapeutic tools against disease.[35,40,53] Engineered polymer-based colloids represent one of the most promising opportunities for treatment of many diseases. The possibility to load them with a drug and to functionalize them with targeting ligands, intended to be recognized by particular cells, paved the way to the so-called active targeting [54–56]. Ideally, for anticancer drugs to be effective in cancer treatment, they should first (after administration) be able to reach the desired tumor tissues through the penetration of barriers in the body with minimal loss of activity in the bloodstream. Second, after reaching the tumor tissue, drugs should be released from the carrier at optimal rate (e.g., 3-10% per day), because a too slow release results in insufficient concentrations at sites of action. Otherwise, a release that is too rapid would lead to a high concentration of free drug in circulation (no accumulation in the tumor), resulting in a considerably lower therapeutic effect and undesired systemic toxicity. A thorough careful engineering of polymeric NPs, including functionalization with targeting ligand, is needed to promote the cellular uptake through the binding of the NPs with the receptors expressed at the surface of cancer cells or blood vessels. A variety of ligands including folate, transferrin, antibodies, amino acids, peptides and protein can be conjugated to polymeric nanoparticles to target receptors commonly overexpressed on a number of cancer types[57–59]. Efficient binding and internalization requires that receptors are expressed exclusively on target sites relative to normal cells.

At present, many delivery systems are under clinical trials but the actively targeted nanomedicines several times failed to demonstrate benefit at the preclinical level. It can likely be mostly attributed to the fact that there are quite a number of anatomical and physiological barriers that need to be overcome to finding the target cells. In this scenario,

new delivery systems need to be explored for the therapeutically active drug molecule to be able to reach the site of action, without affecting healthy organs and tissues [60]. Developing novel tailored nanocarriers in terms of polymer and functionalization, which may influence the pharmacokinetic profile, biodistribution and antitumor activity of the resulting delivery system, demands to be examined. This is the motivation of the thesis.

## 1.2 Aims

The main objective of this thesis is to develop multifunctional polymeric nanoparticles capable of efficient and brain targeted drug delivery.

In particular, the goals of the present thesis can be summarized in the following points:

- To develop and optimize a modified nanoprecipitation method in order to obtain customized NPs with increased drug loading and evaluate its release profile (Chapter II).

- To achieve functionalized NPs for the potential use as drug delivery vectors for efficiently transport and release of PTX into the brain and evaluate their *in vitro* efficiency (Chapter III).

- To explore the *in vivo* characteristics of the NPs and assess their biological profile in terms of physicochemical properties, pharmacokinetics and bio-distribution by means of novel radiolabeling strategies (Chapter IV).

## 1.3 Content of this Dissertation

To overcome the limitations of the conventional drug delivery methods, an engineered and versatile targeted nano-platform is presented in this work. It consisted in designing and developing novel biodegradable polymeric NPs for the delivery of PTX across the BBB with the aim to improve its therapeutic effect on human glioma cells and minimize side effects.

First, a novel biodegradable block co-polymer (P) is synthetized in order to be employed for developing a custom tailored polymeric drug delivery system. In this line, Chapter II exploits the obtained novel polymer to fabricate PTX loaded NPs and optimize a modified nanoprecipitation method, achieving a clear correlation between NPs characteristics and formulation parameters. It grants the possibility to obtain entirely customized NPs in terms of physiochemical properties such as size, zeta-potential, drug loading and release profile.

Chapter III describes how obtained NPs can be converted into effective target drug delivery system for efficiently transport and release of active drug molecule. The developed strategy allows to select the target by functionalizing NPs with the appropriate family of peptides. The strategy assessed for coupling NPs and peptides is the crosslinking via sulfhydryl groups because the reaction is very selective and crosslinking at these sites does not significantly modify the peptide structure. This part of the thesis is focused in developing a nanoparticulate system for PTX release with dual-targeting capability. Functionalization was carried out employing a family of peptides known to be efficiently transported across BBB by a membrane receptor (LRP-1) that also is over-expressed on human glioma cells. In this work the dual-targeting effect, consisting of shuttle PTX from blood to brain and then target glioma cells, is optimized and the effectiveness of the

system is evaluated *in vitro* by cellular assays. In particular, to assess transendothelial transport of PTX, an *in vitro* BBB model is developed and a study on the internalization mechanism is carried out. Moreover, cellular uptake and the cytotoxic effect on glioma cells are also evaluated.

The last part of this thesis is focused in the *in vivo* characterization of the developed nanocarriers. Relevant *in vivo* properties of the NPs are explored to assess their biological profile in view of their application as a target anticancer delivery system. Although the current investigations on targeted polymeric nanoparticles are encouraging, there is a pressing need for careful evaluation in terms of physicochemical properties *in vivo*, pharmacokinetics and bio-distribution. Thus, Chapter IV explores new strategies for NPs radiolabeling with the aim to investigate their *in vivo* fate, focusing on stability in biological environments (stealthiness), biodistribution and brain uptake. Rate constants related to the influx of the radiolabeled NPs across BBB are also studied. This work was mainly performed in the Radiochemistry and Nuclear Imaging Laboratory at Centro de Investigación Cooperativa en Biomateriales (CIC biomaGUNE) in San Sebastian (Spain) in collaboration with Dr. Jordi LLop, group leader of molecular imaging and radiochemistry group.

## 1.4 References


1. D. Brambilla, B. Le Droumaguet, J. Nicolas, S. H. Hashemi, L.-P. Wu, S. M. Moghimi, P. Couvreur and K. Andrieux, Nanotechnologies for Alzheimer's disease: diagnosis, therapy, and safety issues., Nanomedicine 7**,** 521–40 **(2011)**

2. I. Brigger, C. Dubernet and P. Couvreur, Nanoparticles in cancer therapy and diagnosis., Adv. Drug Deliv. Rev. 54**,** 631–51 **(2002)**

3. O. C. Farokhzad and R. Langer, Impact of Nanotechnology on Drug, 3**,** 16–20

4. K. Riehemann, S. W. Schneider, T. a Luger, B. Godin, M. Ferrari and H. Fuchs, Nanomedicine--challenge and perspectives., Angew. Chem. Int. Ed. Engl. 48**,** 872–97 **(2009)**

5. W. R. Sanhai, J. H. Sakamoto, R. Canady and M. Ferrari, Seven challenges for nanomedicine., Nat. Nanotechnol. 3**,** 242–4 **(2008)**

6. P. Couvreur and C. Vauthier, Nanotechnology: intelligent design to treat complex disease., Pharm. Res. 23**,** 1417–50 **(**2006**)**

7. V. P. Torchilin, Micellar nanocarriers: pharmaceutical perspectives., Pharm. Res. 24**,** 1–16 **(2007)**

8. D. E. Discher and F. Ahmed, Polymersomes., Annu. Rev. Biomed. Eng. 8**,** 323–41 **(2006)**

9. X. J. Xiuli Hu, Biodegradable amphiphilic polymer–drug conjugate micelles, Expert Opin. Drug Deliv. 6**,** 1079–1090 **(2009)**

10. H. H. and P. Couvreur, Polymers in Drug Delivery,, 101 **(**2006**)**

11. K. Letchford and H. Burt, A review of the formation and classification of amphiphilic block copolymer nanoparticulate structures: micelles, nanospheres, nanocapsules and polymersomes., Eur. J. Pharm. Biopharm. 65**,** 259–69 **(2007)**

12. et al. Cheng L, He W, Gong H, Wang C, Chen Q, PEGylatedmicelle nanoparticles encapsulating a non-fluorescent near-infrared organic dye as a safe and highly-effective photothermal agent for in vivo cancer therapy, Adv. Funct. Mater. **(2013)**

13. H. X. Jabbari E, Yang X, Moeinzadeh S, Drug release kinetics, cell uptake, and tumor toxicity of hybrid VVVVVVKK peptide-assembled polylactide nanoparticles., Eur J Pharm Biopharm 8 4**,** 49–62. **(2013)**

14. P. D. Verderio P, Bonetti P, Colombo M, Pandolfi L, Intracellular drug release from curcumin-loaded PLGA nanoparticles induces G2/M block in breast cancer cells., Biomacromolecules 14**,** 672–682 **(2013)**

15. K. R. Xu Q, Kambhampati SP, Nanotechnology approaches for ocular drug delivery, Middle East Afr J Ophthalmol. 20**,** 26–37 **(2013)**

16. S. K. Parveen, S. and Sahoo, Polymeric nanoparticles for cancer therapy, J. Drug Target. 16**,** 108–123 **(2008)**

17. C. Facts, Cancer Facts & Figures, **(2011)**

18. A. Gupta, P. Avci, M. Sadasivam, R. Chandran, N. Parizotto, D. Vecchio, W. C. M. a de Melo, T. Dai, L. Y. Chiang and M. R. Hamblin, Shining light on nanotechnology to help repair and regeneration., Biotechnol. Adv. 31**,** 607–31 **(2013)**

19. E. M. Kemper, W. Boogerd, I. Thuis, J. H. Beijnen and O. van Tellingen, Modulation of the blood-brain barrier in oncology: therapeutic opportunities for the treatment of brain tumours?, Cancer Treat. Rev. 30**,** 415–23 **(2004)**

20. M. Wrensch, Y. Minn, T. Chew, M. Bondy and M. S. Berger, Epidemiology of primary brain tumors : literature 1, 278–299 **(2001)**

21. J. Nicolas, S. Mura, D. Brambilla, N. Mackiewicz and P. Couvreur, Design, functionalization strategies and biomedical applications of targeted biodegradable/biocompatible polymer-based nanocarriers for drug delivery., Chem. Soc. Rev. 42**,** 1147–235 **(2013)**

22. W. M. Pardridge, Blood-brain barrier drug targeting: the future of brain drug development., Mol. Interv. 3**,** 90–105, 51 **(2003)**

23. W. M. Pardridge, Blood-brain barrier biology and methodology., J. Neurovirol. 5**,** 556–69 **(1999)**

24. I. van Rooy, S. Cakir-Tascioglu, W. E. Hennink, G. Storm, R. M. Schiffelers and E. Mastrobattista, In vivo methods to study uptake of nanoparticles into the brain., Pharm. Res. 28**,** 456–71 **(2011)**

25. J. M. Walker, The Blood-Brain and Other Neural Barriers, **(**2011**)**

26. A. G. de B. and P. J. Gaillard, Drug Targeting to the Brain, Annu. Rev. Pharmacol. Toxicol. 47**,** 325–335 **(2007)**

27. W. M. Pardridge, The blood-brain barrier: bottleneck in brain drug development., NeuroRx 2**,** 3–14 **(2005)**

28. W. M. Pardridge, Blood-brain barrier delivery., Drug Discov. Today 12**,** 54–61 **(2007)**

29. N. J. Abbott, A. a K. Patabendige, D. E. M. Dolman, S. R. Yusof and D. J. Begley, Structure and function of the blood-brain barrier., Neurobiol. Dis. 37**,** 13–25 **(2010)**

30. W. M. Pardridge, Drug transport across the blood-brain barrier., J. Cereb. Blood Flow Metab. 32**,** 1959–72 **(2012)**

31. M. W. Smith and M. Gumbleton, Endocytosis at the blood-brain barrier: from basic understanding to drug delivery strategies., J. Drug Target. 14**,** 191–214 **(2006)**

32. R. D. Bell, A. P. Sagare, A. E. Friedman, G. S. Bedi, D. M. Holtzman, R. Deane and B. V Zlokovic, Transport pathways for clearance of human Alzheimer's amyloid beta-peptide and apolipoproteins E and J in the mouse central nervous system., J. Cereb. Blood Flow Metab. 27**,** 909–18 **(2007)**

33. C. Fillebeen, L. Descamps, M.-P. Dehouck, L. Fenart, M. Benaissa, G. Spik, R. Cecchelli and a. Pierce, Receptor-mediated Transcytosis of Lactoferrin through the Blood-Brain Barrier, J. Biol. Chem. 274**,** 7011–7017 **(1999)**

34. L. Maletínská, E. A. Blakely, K. A. Bjornstad, L. L. R. Protein, L. Maletı, D. F. Deen, L. J. Knoff and T. M. Forte, Human Glioblastoma Cell Lines : Levels of Low-Density Lipoprotein Receptor and Low-Density Lipoprotein Receptor-related Protein Human Glioblastoma Cell Lines : Levels of Low-Density Lipoprotein Receptor and, 2300–2303 **(2000)**

35. D. Peer, J. M. Karp, S. Hong, O. C. Farokhzad, R. Margalit and R. Langer, Nanocarriers as an emerging platform for cancer therapy., Nat. Nanotechnol. 2**,** 751–60 **(2007)**

36. K. Strebhardt and A. Ullrich, Paul Ehrlich's magic bullet concept: 100 years of progress, Nat Rev Cancer 8**,** 473–480 **(2008)**

37. S. E. A. Gratton, P. A. Ropp, P. D. Pohlhaus, J. C. Luft, V. J. Madden, A. Mary E. Napier and J. M. DeSimone, The effect of particle design on cellular internalization pathways, Proc. Natl. Acad. Sci. U. S. A. 105**,** 11613–11618 **(2008)**

38. M. Wang and M. Thanou, Targeting nanoparticles to cancer, Pharmacol. Res. 62**,** 90–99 **(2010)**

39. J. Liu, Y. Xiao and C. Allen, Polymer-drug compatibility: a guide to the development of delivery systems for the anticancer agent, ellipticine., J. Pharm. Sci. 93**,** 132–43 **(2004)**

40. F. Caruso, T. Hyeon and V. Rotello, Nanomedicine themed issue, **(2012)**

41. B. M. Webster DM, Sundaram P, Injectable nanomaterials for drug delivery: carriers, targeting moieties, and therapeutics, Eur J Pharm Biopharm 84**,** 1–20 **(2013)**

42. M. G. B. & J. V. F. Hak Soo Choi, Wenhao Liu, Preeti Misra, Eiichi Tanaka, John P Zimmer, Binil Itty Ipe, Renal clearance of quantum dots, Nat. Biotechnol. 25**,** 1165–1170 **(2007)**

43. J. S. Moghimi, S.M., Stealth liposomes and long circulating nanoparticles: critical issues in pharmacokinetics, opsonization and protein-binding properties, Prog. Lipid Res. 42**,** 463–478 **(2003)**

44. S. M. Moghimi, a C. Hunter and J. C. Murray, Long-circulating and target-specific nanoparticles: theory to practice., Pharmacol. Rev. 53**,** 283–318 **(2001)**

45. M. R. Dreher, W. Liu, C. R. Michelich, M. W. Dewhirst, F. Yuan and A. Chilkoti, Tumor vascular permeability, accumulation, and penetration of macromolecular drug carriers., J. Natl. Cancer Inst. 98**,** 335–44 **(2006)**

46. H. Maeda, J. Wu, T. Sawa, Y. Matsumura and K. Hori, Tumor vascular permeability and the EPR effect in macromolecular therapeutics: a review., J. Control. Release 65**,** 271–84 **(2000)**

47. R. Sinha, G. J. Kim, S. Nie and D. M. Shin, Nanotechnology in cancer therapeutics: bioconjugated nanoparticles for drug delivery., Mol. Cancer Ther. 5**,** 1909–17 **(2006)**

48. Y. Matsumura, H. Maeda and A. Smancs, A New Concept for Macromolecular Therapeutics in Cancer Chemotherapy : Mechanism of Tumoritropic Accumulation of Proteins and the Antitumor Agent Smancs A New Concept for Macromolecular Therapeutics in Cancer Chemotherapy : Mechanism of Tumoritropic Accum, 6387–6392 **(1986)**

49. R. Duncan, The dawning era of polymer therapeutics, Nat Rev Drug Discov 2**,** 347–360 **(2003)**

50. R. Gref, M. Lück, P. Quellec, M. Marchand, E. Dellacherie, S. Harnisch, T. Blunk and R. . Müller, "Stealth" corona-core nanoparticles surface modified by polyethylene glycol (PEG): influences of the corona (PEG chain length and surface density) and of the core composition on phagocytic uptake and plasma protein adsorption, Colloids Surfaces B Biointerfaces 18**,** 301–313 **(2000)**

51. S. . Jeon and J. . Andrade, Protein—surface interactions in the presence of polyethylene oxide: II. Effect of protein size, J. Colloid Interface Sci. 142**,** 159–166 **(1991)**

52. K. Stockhofe, J. M. Postema, H. Schieferstein and T. L. Ross, Radiolabeling of Nanoparticles and Polymers for PET Imaging., Pharmaceuticals (Basel). 7**,** 392–418 **(2014)**

53. T. Ishida and H. Kiwada, Accelerated blood clearance (ABC) phenomenon upon repeated injection of PEGylated liposomes., Int. J. Pharm. 354**,** 56–62 **(2008)**

54. M. E. K. L. Wooley, Design of polymeric nanoparticles for biomedical delivery applications, Chem Soc Rev 41**,** 2545–2561 **(2012)**

55. N. Kamaly, Z. Xiao, P. M. Valencia, A. F. Radovic-Moreno and and O. C. Farokhzad, Targeted polymeric therapeutic nanoparticles: design, development and clinical translation, Chem. Soc. Rev2 41**,** 2971–3010 **(2012)**

56. D.-E. Lee, H. Koo, K. K. In-Cheol Sun, Ju Hee Ryu and and I. C. Kwon, Multifunctional nanoparticles for multimodal imaging and theragnosis, Chem. Soc. Rev . 41**,** 2656–2672 **(2012)**

57. C. Deng, Y. Jiang, R. Cheng, F. Meng and Z. Zhong, Biodegradable polymeric micelles for targeted and controlled anticancer drug delivery: Promises, progress and prospects, Nano Today 7**,** 467–480 **(2012)**

58. J.-P. B. & C. P. Ngoc Trinh Huynh, Emilie Roger, Nolwenn Lautram, The rise and rise of stealth nanocarriers for cancer therapy: passive versus active targeting, Nanomedicine2 5**,** 1415–1433 **(10AD)**

59. S.-H. Lee, Y. Hoshino, A. Randall, Z. Zeng, P. Baldi, R.-A. Doong and K. J. Shea, Engineered synthetic polymer nanoparticles as IgG affinity ligands., J. Am. Chem. Soc. 134**,** 15765–72 **(2012)**

60. O. M. Koo, I. Rubinstein and H. Onyuksel, Role of nanotechnology in targeted drug delivery and imaging: a concise review., Nanomedicine 1**,** 193–212 **(2005)**

# CHAPTER II.

# Synthesis and Characterization of Customizing Polymeric NPs for PTX Release

## 2.1 Introduction

According to the actual needs in tumor treatment, in this initial part of the thesis, a novel biodegradable block co-polymer (P) was synthetized to develop long circulating NPs for anticancer drug delivery. As it has been introduced in Chapter I, a wide variety of polymers offers the possibility to develop new nanoparticulate systems, mostly because of their flexibility, properties and biodegradation process. Synthetic polymers, especially linear polyesters such as poly (ε-caprolactone) (PCL), polylactide (PLA) and poly (lactide-co-glycolide) (PLGA), have been widely utilized as the polymeric matrix materials of drug delivery systems [1–3]. Many methods have been developed for preparing NPs; these methods can be divided into two main categories depending on if the formulation requires a polymerization reaction or is obtained by preformed polymer [4]. The nanoprecipitation technique was first developed by Fessi and co-workers [5]. This technique uses interfacial preformed polymer deposition followed by solvent displacement and the NPs formation is instantaneous and the entire procedure is carried out in only one step (Scheme 2.1) [6]. In this work Paclitaxel loaded nanoparticles (PTX-NPs) were prepared by a modified nanoprecipitation method and emulsification-solvent evaporation method.

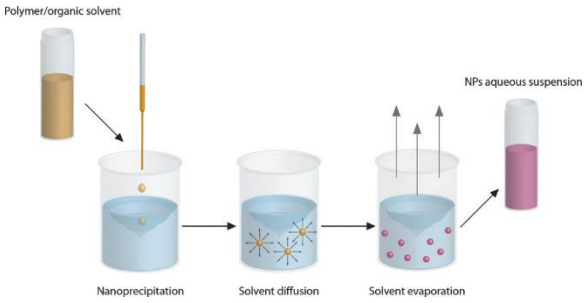


Scheme 2.1 Preparation of polymeric nanocarriers by nanoprecipitation [7]

In the last years there has been an intensive research on the development of biodegradable nanoparticles (NPs) as a suitable means for controlled drug release and targeting [8]. As discussed in Chapter I, the major goals in designing NPs as a delivery system are to control surface properties, particles size, drug loading and release of pharmacologically active agent[1,9]. In this sense, a great deal of effort on customizing NPs

was put to find a precise correlation between NPs characteristics and different experimental parameters so as to obtain completely customized NPs in terms of size, zeta-potential, drug content and release profile. Surface properties plays a key role on the therapeutic efficacy of NPs. To minimize the adsorption of opsonins and thereafter the clearance from the blood, stealthy or long-circulating NPs are achieved by introducing flexible hydrophilic coating (Figure 2.1) [10]. Moghimi D. S. et al. have demonstrated that the effect of size on NPs biodistribution is non-linear and organ specific [11]. This is due to physical and physiological barriers that systematically administered NPs encounter in organs [12]. For a suitable *in vivo* biodistribution the size of NPs should typically be controlled at less than 200 nm with narrow polydispersities [13]. For this reason, the work is carried out with the aim to obtain a very monodisperse NPs population in which NPs could be equipped with an optimal external hydrophilic coating (PEG-corona).

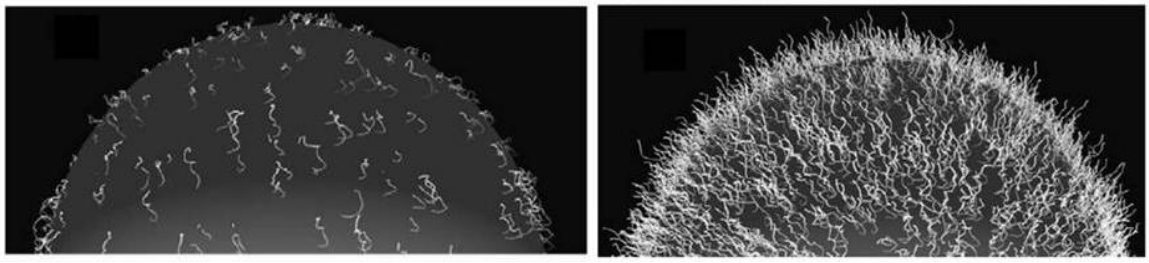

Figure 2.1 Representations of PEG conformations, obtained through incorporation onto surfaces at different densities.(Left) Low surface coverage levels of PEG lead to the “mushroom” configuration and (Right) High surface coverage levels restrict the mobility of the PEG chains and lead to the “brush” configuration [14]

An important parameter for NPs intended to use in clinical is drug loading [15]. High drug loaded polymeric nanosphere remains as an unmet need, indeed, at lower drug content, larger amounts of delivery vehicles need to be administered. This chapter optimizes the encapsulation of PTX into NPs increasing considerably the payload and by differential scanning calorimetry assess if a physical state change of the drug occurs. To complete characterization of the developed NPs, an *in vitro* release profile of PTX was also carried out, with the aim to customize the system in order to achieve a slower and more controlled release for a prolonged period of time. To achieve effective drug delivery, a

controlled release profile is also important in order to reach site-specific action of the drug at therapeutically optimal rate and dosage regimen. PLA NPs, typically prepared via nanoprecipitation[1] tend to give NPs with various formulation challenges that remain to be addressed. Moreover, PLA NPs typically show ‘‘burst’’ drug release profiles in aqueous solution, with 80–90% of the encapsulated drug rapidly released during the first few hours[16].

Biodegradable NPs have been used as sustained release vehicles for administering active agents such as natural or synthetic organic or inorganic entities, proteins, peptides and nucleic acids. The active agent is either dissolved, entrapped, encapsulated, or attached to the NPs matrix [17].

Among the encapsulated drugs, PTX, a semisynthetic taxane (Scheme 2.2), is a successful chemotherapeutic agents that has been approved to effectively kill a wide variety of solid tumors. The anticancer mechanism of PTX as a potent inhibitor of cancer cell replication is related to its ability to block cancer cells in the late G2-mitotic phase of the cell cycle by stimulating microtubule polymerization and suppressing their dynamics. In analogy to many other anticancer drugs, the difficulties in clinical applications of PTX are due to the poor water solubility. Commercial formulation of PTX for clinical treatment is constituted with ethanol and Cremophor EL, which has been associated with acute hypersensitivity reaction [18] and side effects including neutropenia, cardiac arrhythmias, dose-related myalgia, neuropathy and serious killing of normal cells [19]. To achieve desired therapeutic performance of PTX, various formulations were proposed, among them liposomes, which can reduce the side effects but also have some disadvantages such as low entrapment efficiency [20]. As a result, this chapter seeks to solve some of these restrictions and achieve optimized NPs not only by tailoring their physicochemical properties but also by

evaluating their biocompatibility and anti-proliferative efficiency against glioblastoma cells lines.

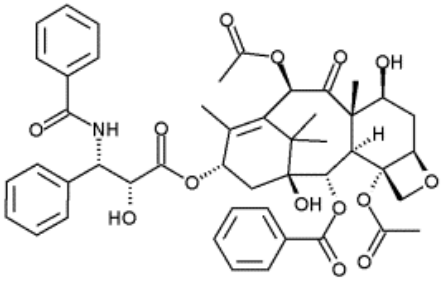


Scheme 2.2 Chemical structure of PTX

## 2.2 Experimental Section

### 2.2.1 Materials

1.8-Octanediol (98%) and PEG ($M_W$ 1.5 KDa) were purchased from Sigma (USA). Glutaric acid (99%) was obtained from Alfa Aesar (USA). PTX (≥ 97%) was provided by Yunnan Hande Bio-Tech CO, LTD, P.R. China. FBS was purchased from Lonza, L-Glutamine and Penicillin/Streptomycin were provided by Labclinics. All other chemicals of analytical grade were purchased from Sigma (Sigma–Aldrich, Germany).

### 2.2.2 Synthesis of Block Co-polymer (P)

Block co-polymer (P) constituted by rigid and flexible alternating blocks was synthetized by the esterification of 1.8-Octanediol with glutaric acid and subsequently with PEG 1500. Glutaric acid (6 g, 45 mmol) and 1.8-Octanediol (5.53 g, 37 mmol) were reacted in a microwave reactor (Discovery CEM) at a power of 100 W for 1 hour. The reaction was performed under vacuum (100 mbar) with continuous stirring and cooling the system with compressed air to maintain the temperature constant at 120º C. Once the glutaric acid exceeding prepolymer or rigid block was generated, it was subsequently reacted with PEG 1500 which is added in a 1:1 weight ratio with the prepolymer. The polymerization

reaction was performed in the microwave reactor with the conditions above described. The resulting block co-polymer (P) was dried at room temperature and used for NPs preparation without further treatment.

### 2.2.3 Characterization of Block Co-Polymer (P)

To determinate the molecular structure of block co-polymer P a Fourier Transform Infrared (FTIR) analysis was performed using a Thermo Scientific Nicolet iS10 spectrophotometer. The composition of the P co-polymer was determined by proton nuclear magnetic resonance $^{1}$H-NMR in $CDCl_3$ at 300 MHz (Varian 400 MR). The weight-averaged molecular weight and molecular weight distribution of the obtained polymers were determined using a gel permeation chromatography (GPC) LaChrome Elite from Hitachi, with pump and refractive index (RI) detector from Hitachi. The following conditions were adopted: the column was Shodex KF-603, the mobile phase was THF HPLC grade, and flow rate was 0.5 ml/min. The samples were dissolved in THF, filtered, and then 20 µl were injected. The molecular weights of the copolymers were determined relative to the standards curve, prepared using a series of Shodex SM-105 polystyrene standards.

### 2.2.4 Formulation of NPs

#### Nanoprecipitation

NPs were prepared according to a modified nanoprecipitation method (or solvent displacement method)[5]. 20 mg of P and a specified quantity of PTX were dissolved in acetone, a suitable organic solvent pharmacologically accepted with regard to toxicity, to form the diffusing phase. This phase was then added to dispersing phase in which the polymer is insoluble, by means of a syringe, controlled by a syringe-pump (KD scientific), positioned with the needle directly in the medium, under a magnetic stirring of 120 rpm and at room temperature. The resulting NPs suspension was allowed to stir uncovered at room temperature until complete evaporation of the organic solvent. Drug free NPs were prepared according to the same procedure. To investigate the influence of formulation

parameters on NPs formation, size and zeta potential the following variables were studied:

- methanol, ethanol and water were used as dispersing phase (no-solvent)
- for each no-solvent, the ratio S/NS was varied from 1:2 to 1:20 (v/v)
- polymer concentration in the organic phase was increased from 10 to 50 mg/ml
- a range of drug dissolved in the organic phase (theoretical drug loading) from 0% to 25% was used

In each set of experiment only one formulation variable was changed at a time while the other parameters were kept constant. The NPs were processed as above in triplicate. NPs were purified by centrifugation (Hettich Centrifuge, EBA 21, 4000 g, 45 min.) with ultra-centrifugal device (Amicon Ultra-15, Ultracel membrane with 100,000 MWCO, Millipore, USA). The supernatant containing the dissolved free drug was discarded and the pellet freeze-dried (Telstar, LyoAlfa 6) for 48 hours. Freeze-drying was carried out without lyoprotectant. The nanoparticle recovery was calculated using Equation 2.1

$$\text{NPs recovery } (\%) = \frac{\text{Mass of NPs recovered } \times 100}{\text{Mass of polymer and drug used in formulation}}$$

Equation 2.1

## Emulsion

To demonstrate the capability of block co-polymer P to be employed as a drug delivery system, NPs were also prepared by a modified emulsification by sonication-solvent evaporation [21]. This method involved the use of an organic phase consisting of polymer at 10 mg/ml concentration and selected amounts of PTX, dissolved in 1 ml DCM. This organic phase was added to an aqueous phase to form an emulsion, which was broken down into

nanodroplets by applying external energy through a 10 seconds pulsing (2"on/2"off) sonication at 100% amplitude. Upon the solvent evaporated whit magnetic stirring at 300 rpm and under atmospheric conditions for 4 hours, a colloidal suspension of PTX-NPs was obtained. NPs were purified as described above and freeze-dried with cryoprotectant to ensure optimal re-suspension.

### 2.2.5 Characterization of NPs

#### Determination of NPs Size and polydispersities

The NPs size distributions and polydispersity were measured by Dynamic Light Scattering (DLS) (Malvern Zeta Sizer Nano Series) at 25ºC and at scattering angle of 90º using sample appropriately diluted with mQ water. For each sample the intensity-weighted mean value was recorded as the average of three measurements. The results were expressed as mean ± S.D for two replicate sample. Further measurements were performed by Nanoparticles Tracking Analysis (NTA) (Nanosight LM 10, Laser Module LM 14C), with a 532 nm laser beam passed through a prism-edged optical flat and validating all data with video files of the NPs moving under Brownian motion to determinate NPs size distribution and monodispersity.

#### Surface Charge and morphology

NPs were also characterized with respect to zeta (ζ) potential, the analysis was performed in triplicate on Malvern ZetaSizer (Nano Series) with a Smoluchowsky constant F ($K_a$) of 1.5 to achieve zeta potential values from electrophoretic mobility. For each sample the mean zeta potential was recorded as the average of three measurements. The results were expressed as mean ± S.D for two replicate sample. The size and morphology of the NPs were observed by Transmission Electron Microscopy (TEM) (Jeol Jem 2011). A drop of the NPs suspension (10 µl) was placed on carbon electron microscopy grids (Holey Carbon Film) and air-dried before analyze at an acceleration voltage of 200 kV without negative staining.

## Thermal Characterization

The physical state (crystalline *versus* amorphous) and miscibility of PTX in the NPs were characterized by Differential Scanning Calorimetry (DSC) (Mettler Toledo DSC821e) on the glass transition temperature ($T_g$) or melting point ($T_m$). As a control pure PTX, empty NPs and the physical mixture of PTX with empty NPs (1:1 w/w) was also analyzed. Approximately 4-5 mg of each sample, sealed in a standard aluminum pan, was purged with dry nitrogen at a flow rate of 50 ml/min while the sample was heated from 50ºC to 300ºC at a rate of 10ºC/min.

## Drug Incorporation Efficiency

Freeze-dried NPs loaded with PTX were dissolved in acetonitrile and the amount of entrapped drug was detected by Ultra Performance Liquid Chromatography (UPLC) (Waters ACQUITY UPLC H-Class). A reverse phase BEH C18 column (1.7 µm 2.1 x 50 mm) was used. The mobile phase consisted of a mixture of acetonitrile and water (60:40 v/v) and was delivered at a flow rate of 0.6 ml/min. PTX was quantified by UV detection (λ=227 nm, Waters TUV detector). A calibration curve of standard PTX solution was used to obtain the PTX concentration, which was linear over the range of 60.5 – 0.47 µg/ml with a correlation coefficient of $R^2$=0.9998. Drug incorporation efficiency was expressed as drug content (D.C. % w/w) and encapsulation efficiency (E.E. %); represented by Equation 2.2 and Equation 2.3, respectively. For each sample the mean value was recorded as the average of three measurements. The results were expressed as mean ± S.D for two replicate.

$$\text{Drug Content}\left(\%\,\frac{w}{w}\right) = \frac{\text{Mass of drug in NPs } \times 100}{\text{Mass of NPs recovered}}$$

Equation 2.2

$$\text{Encapsulation Efficiency}(\%) = \frac{\text{Mass of drug in NPs } \times 100}{\text{Mass of drug used in formulation}}$$

Equation 2.3

### *In vitro* Drug Release Analysis

*In vitro* drug release from PTX loaded NPs was performed using a modified dialysis-bag diffusion technique, as reported by Kim et al. and Averineni et al. (22, 23). Specifically, a known amount of freeze-dried PTX-NPs, corresponding to 0.3 mg of PTX, was suspended in a dialysis bag (regenerated cellulose tubular membrane, Cellu SEP® T2, nominalMWCO 6000‑ 8000, membrane filtration products, Inc, TX) containing 15 ml of release PBS solution (0.1 M at pH 7.4 and 0.3% v/v of Tween-80). The bag containing NPs suspension was placed in a 50 ml Eppendorf® Tube (Fisher Scientific Company, Houston, TX) containing 30ml of release medium (PBSsolution and 0.3% v/v of Tween-80). The whole system was then placed in an orbital shaking incubator (LM-450D, Yihder Co., Ltd) at 37°C and at shaking speed of 200 rpm. At pre-decided time points 1 ml aliquots of release medium was withdrawn and replaced with an equal volume of fresh medium to maintain the sink conditions. The withdrawn aliquots were filtered through a 0.2 µm syringe filter directly into UPLC vials and immediately capped. The amount of PTX released in each time interval was determined by UPLC with a reverse phase BEH C18 column (1.7 µm 2.1×50 mm). The mobile phase consisted of a mixture of Acetonitrile/Ammonium Acetate Buffer (20 mM, pH 4.5) = 60/40 delivered at a flow rate of 0.6 ml/min. PTX was quantified by UV detection (λ=227 nm, Waters TUV detector); the reported values are averages ± S.D. of three replicates. The percent drug release was calculated as percentage of the total encapsulated drug. For the polymer degradation studies an UPLC (Waters ACQUITY UPLC H-Class) equipped with a TOFMS detector was used, using the same UPLC conditions above described.

## 2.2.6 Cell experiment

### *In vitro* immunological assay

Hemocompatibility of PTX-NPs was evaluated diluting NPs in PBS (0.1 M pH 7.4) at concentrations of 10 and 100 µg/ml. Hemocompatibility test was carried out after blood exposure. Interaction of NPs with blood was analyzed using normal human plasma

collected under citrate 15 minutes before starting blood exposure during 15 minutes at 37ºC and at atmospheric pressure. First analysis was the hemolysis test and according to Drabkin's method, when free hemoglobin <2% NPs were considered non haemolyitic; 2-5% slightly haemolytic and >5% haemolytic. Further experiments were blood cell counting and quantification of complement activation adopting the determination of the C3a concentration (ELISA kit). Finally, analysis of the activation of the coagulation either by the intrinsic (TCA test) or the extrinsic (Quick) pathways was performed.

## *In vitro* anti-proliferative efficiency

In order to evaluate the cytotoxicity of the PTX-NPs on U-87 MG cells, the cells were grown in DMEM supplemented with 10% FBS, 1% L-Glutamine and 1% Penicillin/Streptomycin and plated in 96-well plates at a cellular density of 30.000cells/ml. After 24 h, medium was aspirated and substituted with 100 µl of various PTX concentration (10, 20 nM) of 3, 5 and 8% theoretical loaded PTX-NPs suspensions. Empty NPs were also examined with the concentration corresponding to that of 10 nM of PTX. One column, cells with PTX at 10 and 20 nM, was used as positive control; one column, cells without NPs, was used as the control; another column, without cells, was used as the blank. After 1, 4, 6, 8 and 11 days, cell viability was assessed via MTS (CellTiter 96® AQueous One Solution Cell Proliferation Assay, Promega Corporation, USA) following the manufacturer instructions. Briefly, cells were washed with PBS and incubated with a solution of the MTS reagent and complete media at 37ºC. The absorption (A), which represented cell viability was measured via a microplate reader (Spectramax M2$^{e}$) at the wavelength of 490 nm. Cell viability was calculated by Equation 2.4 and the errors bar were obtained from triplicate samples.

$$\text{Cell viability (\%)} = \frac{\mathrm{A}_{sample} - A_{blank}}{\mathrm{A}_{control} - A_{blank}} \times 100$$

Equation 2.4

## 2.3 Results and Discussion

### 2.3.1 Synthesis and Characterization of Block Co-polymer (P)

Block co-polymer P constituted by flexible blocks (PEG 1500) and rigid blocks (1.8-Octanediol and Glutaric Acid), was synthetized by polycondensation in a microwave reactor, under vacuum, at 120ºC and 100 W (Scheme 2.3). The identity and purity (with respect residual monomers) of the co-polymer P were determined by FTIR. Figure 2.2 shows a representative FTIR spectrum of P, which is consistent with the structure of the expected polymer. It shows that the strong band at 1732 $cm^{-1}$ is assigned to C=O stretch of the ester band. The absorption band at 3449 $cm^{-1}$ is attributed to the terminal hydroxyl group and that at 1500-1045 $cm^{-1}$ is due to the C–O stretching of the ester band. C-H stretch of $CH_2$ is observed at absorption band 2919-2850 $cm^{-1}$. The composition of P co-polymer is confirmed by $^1$H-NMR (Figure 2.3). One of the prominent features is a large peak at 3.64 ppm (peak b), corresponding to the methylene groups of the PEG 1500. The multiplets at 4.06 and at 1.61 ppm (peak a and e) correspond to the $CH_2$ protons of 1.8-octanediol. The multiplets at 2.37 and 1.94 ppm (peak c and d) are assigned to the glutaric acid methylene protons in α and β position relative to carbonyl group, respectively. The weight-averaged molecular weight and molecular weight distribution of the obtained prepolymer and P co-polymer were determined by means of GPC. The molecular weight were found to be 1069 and 2335 for the prepolymer and P co-polymer, respectively. The PDI was narrow, which was around 1.8 for the prepolymer and 2.01 for the P co-polymer.

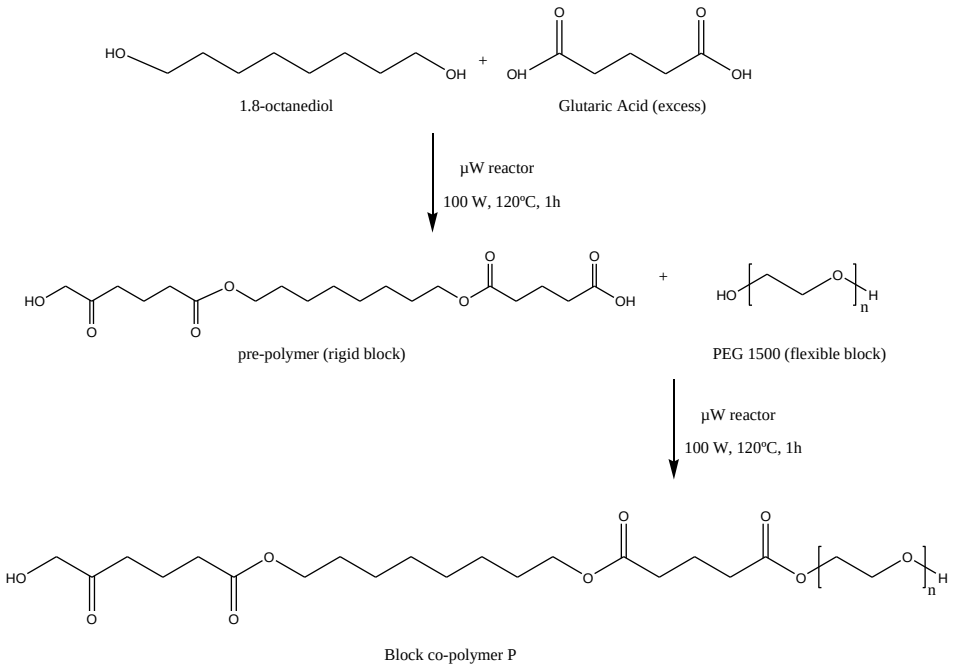


Scheme 2.3 Synthesis of block-co polymer P by polycondensation

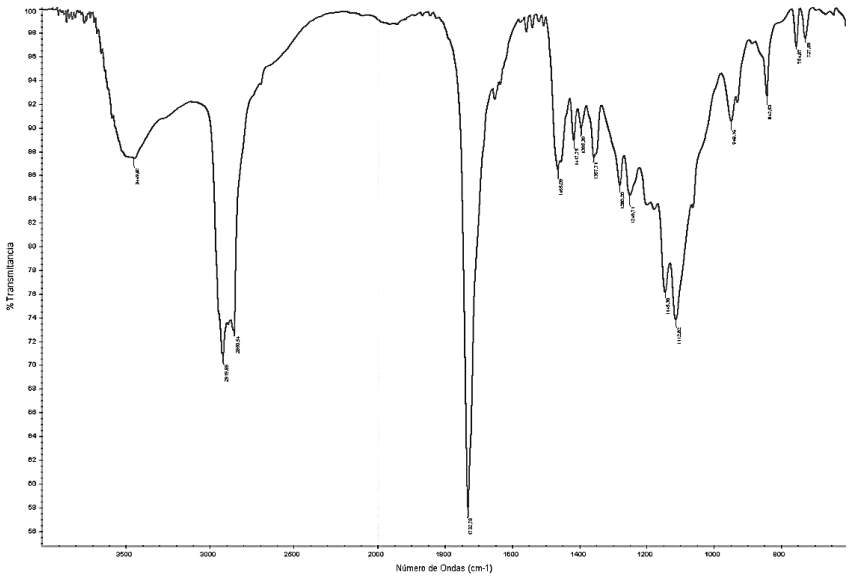


Figure 2.2 FTIR spectra of the P co-polymer

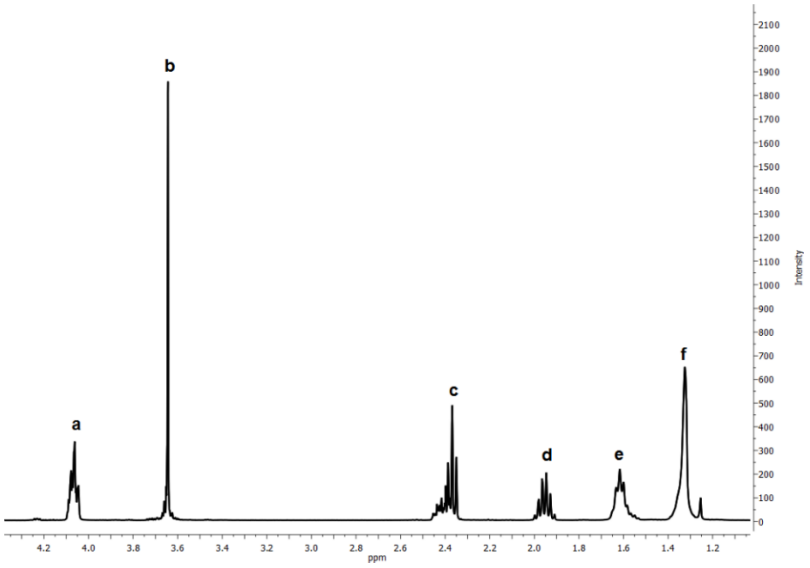


Figure 2.3 $^{1}$H-NMR spectra of P co-polymer in $CDCl_3$

### 2.3.2 Preparation and Characterization of NPs

## Effects of varying formulation parameters to control NPs size and zeta potential

NPs with and without PTX loading and based on different formulation parameters were prepared by a modified nanoprecipitation method [5]. An experimental design of NPs fabrication was selected to investigate how formulation variables (no-solvent type, solvent/no-solvent ratio and polymer concentration) could affect NPs characteristics. The experiments were designed with the ultimate goal of tailoring NPs in terms of size and zeta potential. As a starting point for controlling NPs characteristics, we first studied the effect of different no-solvent types used to disperse organic phase. Senichev et al. have demonstrated that a solvent/no-solvent (S/NS) system affects the diffusion rate and thus the NPs size [22]. To analyze the impact of a S/NS system we studied the affinity of the solvent (acetone) for the no-solvent by means of the interaction parameter (χ). This interaction is expressed as:

$$\chi = \frac{V_{NS}}{RT}(\delta_S - \delta_{NS})^2$$

Equation 2.5

Where $V_{NS}$ is the molar volume of the non-solvent (here, methanol 40.7 $cm^3$/mol, ethanol 58.5 $cm^3$/mol and water 18.016 $cm^3$/mol) and δ is the Hildebrand solubility parameter. The calculated interaction parameters (Table 2.1) were then plotted against NPs size and presented in Figure 2.4. As expected, the higher the interaction parameter, the larger the NPs. We chose to investigate the relationship between NPs size and S/NS miscibility and observed a dependence of NPs size on the solubility parameter. As shown in Figure 2.5 an increase of S/NS miscibility (decrease in Δδ, as indicated by the arrow shown in Figure 2.5) led to a decrease in the mean NPs size, with all other formulations parameters held constant.

Table 2.1 Non-solvent properties. Miscibility and calculated interaction parameters χ of solvent/non-solvent binary mixture

| **Non-Solvent** | **Solubility parameter, δ $(MPa)^{1/2}$** | **Δδ** | **Interaction parameter [a, b] χ** |
|---|---|---|---|
| Water | 48 | 28.3 | 5.14 |
| Methanol | 29.7 | 10 | 1.44 |
| Ethanol | 26.2 | 6,5 | 0.87 |

[a] Solvent: Acetone, [b] Calculated using equation Equation 2.5 and for T=25ºC (298 K). Polymer was not take into account

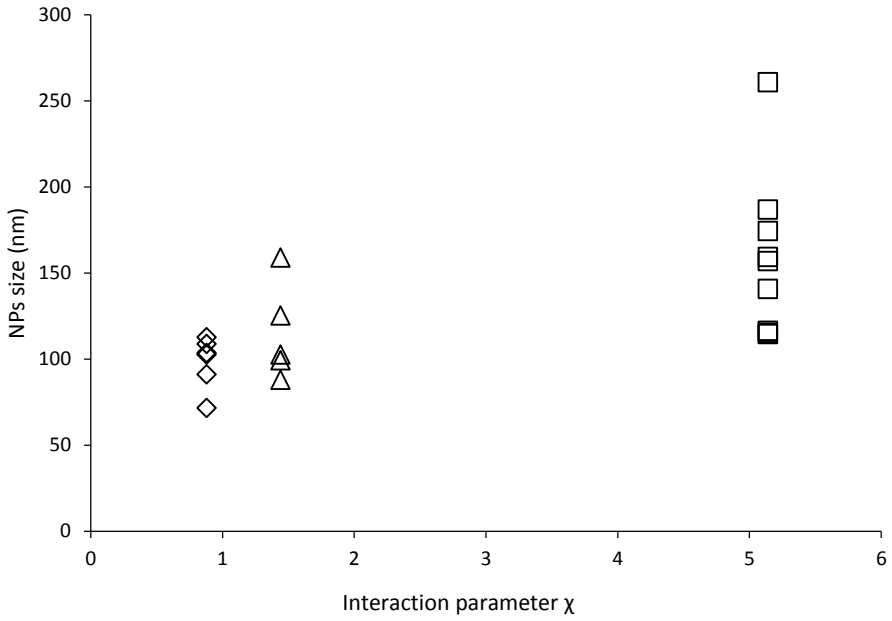


Figure 2.4 Relationship between calculated interaction parameter χ of binary S/NS mixture and NPs size (◊ Ethanol, Δ Methanol, □ Water). NPs size determined by DLS

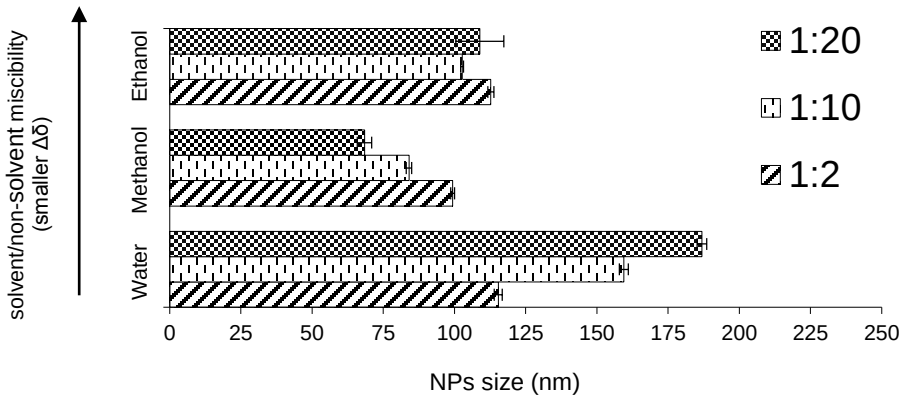


Figure 2.5 Effect of varying formulation parameters on NPs size: modifying the non-solvent type and the acetone/non-solvent ration (1:2, 1:10, 1:20). NPs size determined by DLS; data represented mean ± SD (n=3)

Concurrently with the investigation of the effect of S/NS, we studied the effect of altering the S/NS ratio during nanoprecipitation. When the ratio of diffusion of the acetone into the non-solvent was varied for a fixed polymer concentration (Figure 2.5), a correlation of

NPs size with S/NS ratio was observed. This correlation was remarked for all polymer concentrations and for two of the non-solvent types tested (Figure 2.6). In water, for example, at 10 mg/ml polymer concentration, NPs size increased from 116.5 ± 0.9 to 174.4 ± 1.2 nm as the ratio S/NS decreased from 0.5 to 0.05, respectively (mean ± SD, n=3 for each formulation; $p>0.05$). For methanol the correlation is inverse than water, it was found that the higher solvent/non-solvent ratio, the bigger NPs; for example, at 50 mg/ml polymer concentration, NPs size decrease from 125.4 ± 1.7 to 73.63 ± 0.15 nm as the ratio S/NS decrease from 0.5 to 0.05, respectively. For the ethanol, no clear correlation between the NPs size and S/NS ratio was found. On the other hand, a clear dependence of the NPs size from polymer concentration in the diffusing phase, was observed for all the non-solvent types tested. When polymer concentrations were varied during NPs fabrication at a fixed S/NS ratio, an increasing NPs size with increasing polymer concentration is observed (Figure 2.6). For example, at 1:10 acetone/ethanol ratio, NPs sizes were 84.8 ±2.5, 102.7±0.47, 134.8±1.7 nm when the polymer concentration were 10, 20, 50 mg/ml, respectively. Similar trends were observed in all other solvents investigated. Regarding polymer concentration has to be taken into consideration that a too high polymer concentration in the solvent prevented nanoprecipitation. This effect is probably due to the high viscosity of the polymeric solution that prevents an appropriate diffusion of the solvent toward the non-solvent. Other authors found also that the higher the polymer concentration in the solvent, the higher loss of polymer; they explained this effect in terms of the intrinsic viscosity and interaction constants [23]. Also we studied the effects of varying formulations parameters on ζ potential. This is an important index for the stability of the NPs suspension. High absolute value of zeta potential indicates high electric charge on the surface of the NPs, which can cause strong repellent forces among particles to prevent aggregation [24]. All NPs batches were found negatively charged with a value depending on the S/NS ratio and polymeric concentration. As shown in Figure 2.6 the zeta potential ranged ~ 20 mV for water, ~ 12 mV for methanol and ~ 7 mV for ethanol. A clear correlation of ζ potential with formulation parameters was found for water; for a fixed polymer concentration, the lower the ratio S/NS, more negative the zeta potential.

When polymer concentration were varied during NPs fabrication at a fixed S/NS ratio, it was found that the higher polymeric concentration, less negative NPs. Higher negative value (-32 mV) was obtained at 10 mg/ml polymeric concentration and 1:20 S/NS ratio. Methanol exhibited the same correlation with ζ potential values moving in a narrow range. Lower negative value (-5 mV) was obtained at 50 mg/ml polymeric concentration and 1:2 S/NS ratio. As though for the size, no clear correlation between zeta potential and formulation parameters was found for ethanol. A ζ potential in this range is often observed in polyester nanoparticles and a value of about – 25 mV ensures a high-energy barrier that stabilizes the nanosuspension [25].

.

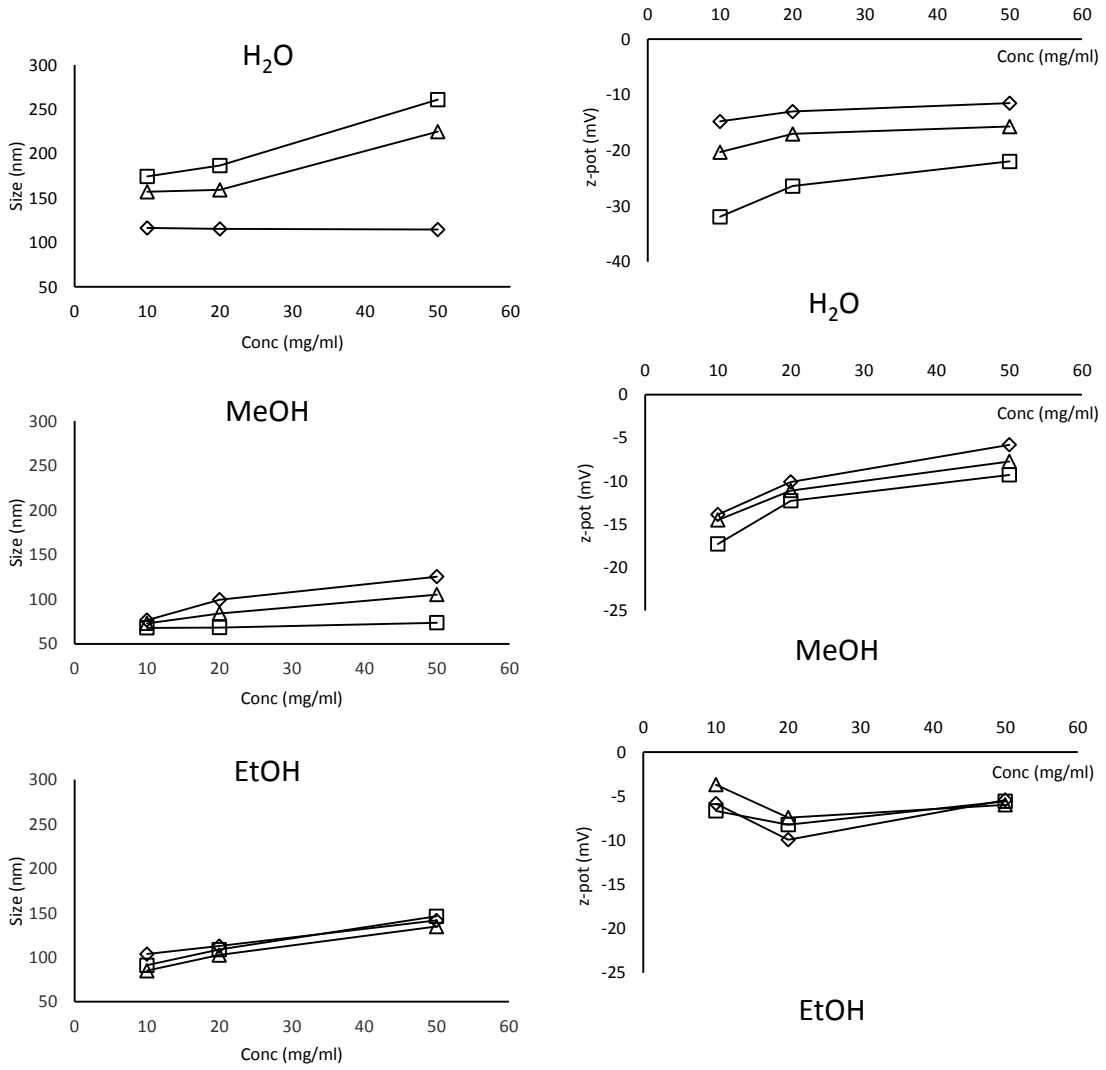


Figure 2.6 Correlation of polymer concentration with NPs size and zeta potential (left and right column, respectively) at different solvent/non-solvent ratio (□ 1:20, Δ 1:10, ◊ 1:2) and for three non-solvent type. NPs size and z-potential determined by DLS; (n=3; errors bar not shown, SD≤2.5 nm for size and ≤1.8 mV for ζ)

## Size distribution and zeta potential

All formulations formed monomodally distributed NPs in the desire range below 200 nm (Figure 2.6). The NPs size for all three non-solvent and for the investigated concentrations ranged from 70 to 200 nm and the size distribution was narrow with polydispersity in the range from 0.05 to 0.282. All formulations exhibited a net negative charge with ζ potential values ranging from -32 to -3 mV (Figure 2.6).

## Optimized nanoprecipitation variables

The initial approach to obtain PTX loaded NPs involved the choice of acetone and water as components of our nanoprecipitation based system. Acetone is not a concern in terms of toxicity, it belongs to Class 3 according to the ICH solvent toxicity scale (Class 3 solvent present very low risk to human health). Acetone has a low dielectric constant value which destines it a rather lipophilic drug encapsulation. The use of water as diffusing phase is the most appropriate; indeed the presence of the residual solvent is minimized only to residual acetone. In the following studies, the polymer concentration was fixed at 20 mg/ml with acetone/water ratio as 1:20. The optimized NPs were further investigated by NTA and DLS. PTX-NPs size distribution is rather monodisperse with a mean of about 180 nm, confirmed by NTA (Figure 2.7 a, c) and by DLS (Figure 2.7 b). No influence was exerted by PTX on the ζ potential value of NPs (-26 mV).

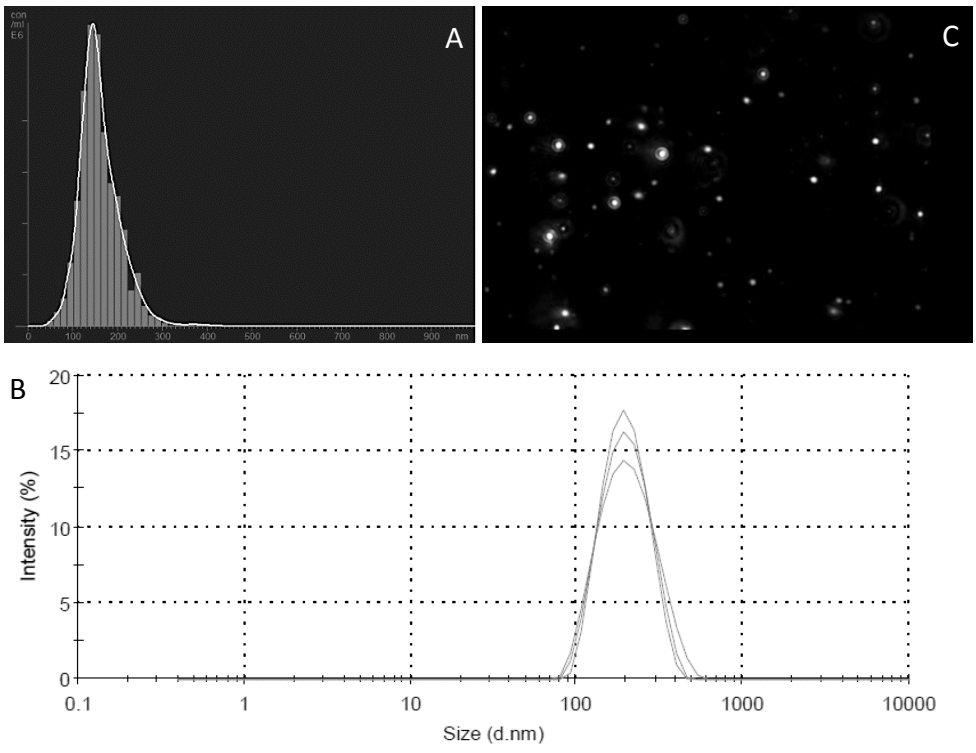


Figure 2.7 PTX-NPs size distribution plots obtained by (A) NTA, (B) DLS and (C) NTA sample video frame of NPs moving under Brownian motion

## Surface morphology

The morphology images of the 3% PTX-NPs obtained from TEM indicate that the NPs can be estimated around 130-180 nm in size and are spherical in shape with a smooth surface. In the TEM photos, "PEG corona" on the NP surface could be observed (Figure 2.8). A further confirmation of the PEG corona surrounding NPs (marked in Figure 2.8 c with white arrow) was obtained by tilting angle experiments. The TEM carbon grid was tilted from 0º (Figure 2.8 c) to 45º (Figure 2.8 d); the PEG corona thickness remained unchanged, excluding a hypothetical aberration caused by the electrons beam interaction with the spherical surface (aberration occurred for the carbon grid spot marked with black arrow in Figure 2.8 c). An optimal external hydrophilic coating can improve stealthy behavior avoiding recognition by the reticuloendothelial system.

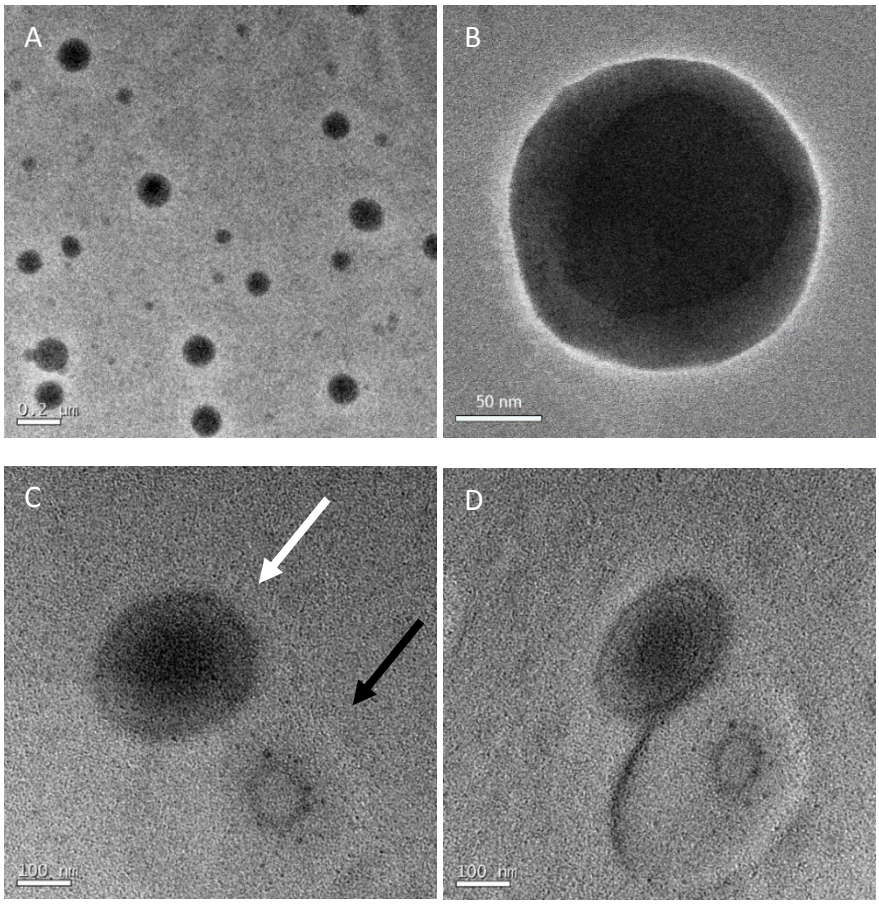


Figure 2.8 TEM images of PTX-NPs (A, B)at different magnification and (C, D) PTX-NPs (white arrow) subjected to tilting angle experiments to assert PEG corona thickness remained unchanged; TEM carbon grid tilted from 0º (C) to 45º (D)

## Drug incorporation efficiency

The influence of the theoretical loading of PTX into P co-polymer NPs was examined. An increase in the theoretical loading from 2 to 20% w/w led to a corresponding increase in drug content from 3.8 ± 0.2 to 24 ± 3.5% w/w (Figure 2.9). Along with drug content, encapsulation efficiency was analyzed and as shown in Figure 2.9, the encapsulation efficiency remains constant approximately at 63 ± 0.7% with increasing theoretical PTX loading. Our results are consistent with those reported by Danhier et al. [26], where 70% PTX E.E. into PLGA NPs was obtained with the nanoprecipitation methods. The results of this study are encouraging, because the drug contents are much higher than other polyester-based NPs [27]. Generally, it was reported that the D.C. of PTX was about 3% in the nanoprecipitated NPs when the initial PTX loading was 4% (w/w) [27]. Emulsioned PEG-PLA NPs reported by Q. Hu et al. [28,29] reach a drug content ranging from 1 to 3 % along with an encapsulation efficiency of about 50%. When PLGA NPs are emulsioned with TPGS, which act as an emulsifier enhancing emulsification efficiency, PTX E.E. increases up to 80%, otherwise PTX D.C. does not exceed 3% [30].

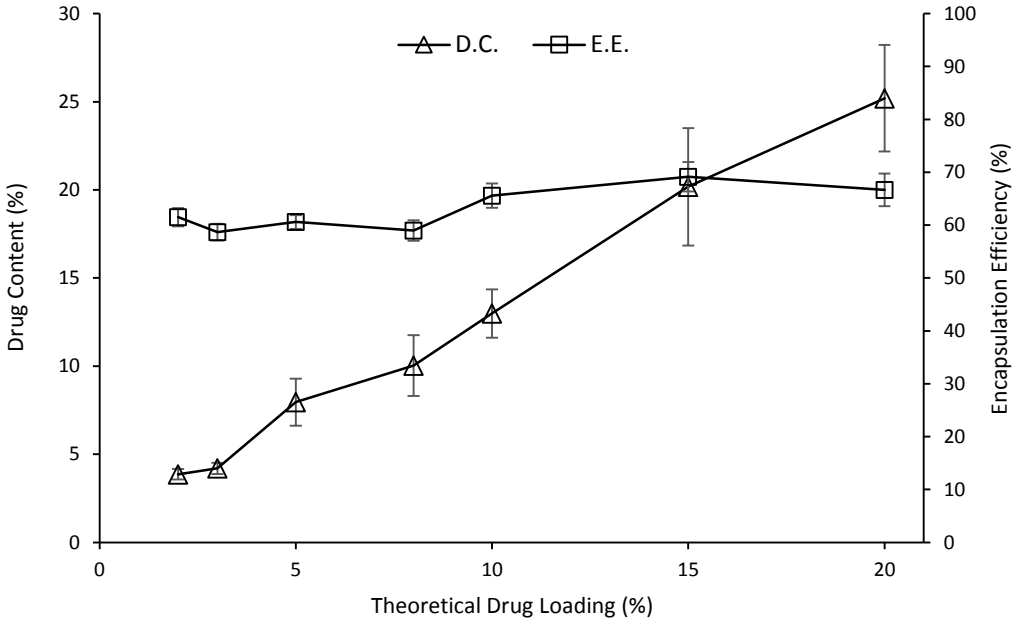


Figure 2.9 Drug Content (DC % w/w) and Encapsulation Efficiency (EE %) of PTX-NPs as a function of theoretical PTX loading

As shown in Table 2.2 moderate NPs recovery yield after freeze-drying was achieved, ranging from 47.5 ± 6.1 to 64.5 ± 7% for lower and higher theoretical PTX loading, respectively.

Table 2.2 NPs recovery (%), D.C. (%) and E.E. (%) as a function of theoretical drug loading

| Theoretical drug loading % (w/w) | NPs recovery (%) ± S.D. | Drug Content % (w/w) ± S.D. | Encapsulation Efficiency (w/w) % |
|---|---|---|---|
| 2 | 49,5 ± 4.2 | 3,8 ± 0.2 | 61,5 ± 1,7 |
| 3 | 47,5 ± 6,1 | 4,2 ± 0.3 | 58,7 ± 1,6 |
| 5 | 48,2 ± 3,9 | 7,6 ± 1.4 | 60,6 ± 1,3 |
| 8 | 57,5 ± 6,7 | 10,4 ± 1.7 | 59 ± 1,9 |
| 10 | 56 ± 7,1 | 13,1 ± 1.3 | 65,6 ± 2,3 |
| 15 | 64,5 ± 7 | 19,8 ± 3.3 | 69,1 ± 2,8 |
| 20 | 60 ± 6,8 | 24 ± 3.5 | 66,7 ± 3,1 |

We hypothesize that high D.C. and PTX depending NPs recovery yield, are most likely due to the arrangement of the hydrophobic P co-polymer regions when forming NPs. Indeed, PTX acting as binding agent facilitates nanoprecipitation probably by increasing lipophilic interaction among hydrophobic P co-polymer blocks. Supposedly, polyester regions of the P co-polymer are in close contact to PTX while PEG groups are directed to NPs surface to interact with water.

## DSC

To determinate the physical status of PTX inside NPs, DSC analysis was performed. The results are shown in Figure 2.10. Pure PTX showed an endothermic melting peak at about 223ºC, shifted to lower temperature (210ºC) in the thermograph of the physical mixture. 3% PTX-NPs did not show a melting peak, such as the free-drug NPs, demonstrating that the polymer inhibited the crystallization of PTX during NPs formation. Therefore, it could be assessed that the PTX in the NPs was in an amorphous or disordered crystalline phase

of a molecular dispersion or a solid solution state in the polymer matrix after the production. Increasing NPs drug content, PTX remains in amorphous phase for theoretical drug loading of 5%. The 15% PTX-NPs showed a sharp melting peak at about 230º C indicating that a fraction of PTX was crystalline and did not dissolve in the P co-polymer matrix. Therefore, while PTX in the 3 and 5% sample completely dissolved in P co-polymer matrix, phase separation between PTX and P co-polymer occurred for the 15% PTX-NPs sample. Our results are consistent with previous findings by Mu et al. [31] that phase separation and crystallization of hydrophobic drugs like PTX can occur in NPs at high drug loading.

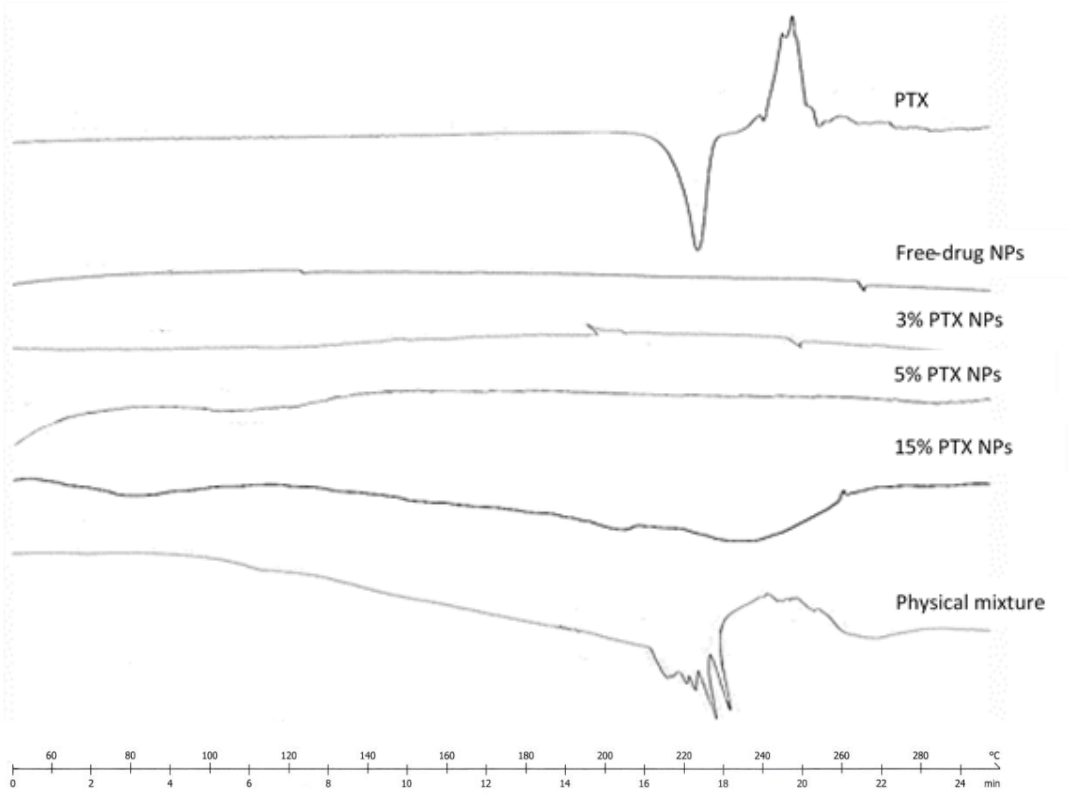


Figure 2.10 Differential Scanning Calorimetry (DSC) thermographs of PTX, free-drug NPs, 3, 5, 15 % PTX-NPs, and NPs/PTX as physical mixture (1:1 w/w)

## In vitro drug release from PTX-NPs

The release profile of PTX from different formulations are presented in Figure 2.11. For the different PTX loaded co-polymer NPs, the release pattern displayed an approximately first-order release, without initial burst and with a drug release reaching completion in approximately 12 days for 3% PTX-NPs. Figure 2.11 also shows PTX release profile in the first hours of test; it's possible to appreciate that the release is very slow and constant with approximately 6.2% of PTX released in 3 hours from 3%-PTX-NPs. NPs with higher drug loading (10, 15 %) showed the same trend with a slower release and around of 60% of PTX was released in 12 days. Since NPs are prepared by the same co-polymer P, the difference in PTX percentage released can be explained as follows. For 10 and 15 % PTX loaded NPs, a considerable amount of drug is present in the bulk. This higher PTX content (w/w) in the polymeric matrix consequently bestow on NPs greater hydrophobic character, leading to slower release. Moreover the initial burst absence and the nearly linear behaviour demonstrate the absence of adsorbed drug on NPs surface. *In vitro* PTX release from polyester-based NPs usually present biphasic profile or very fast complete drug release. PHA (Poly Hydroxyalkanotes) and poly ε-CPL for example, released over 50% of PTX in the first hours [27,32]. On the other hand PDLLA/PLGA PEG NPs exhibited a lower burst effect, but nevertheless the total cargo is released in 2 and 4 days, respectively [27,29], which, generally, is too fast to meet therapeutic needs. With respect to our PTX co-polymer NPs, *in vitro* kinetic shows a release that is proportional to NPs co-polymer matrix degradation and depending on the total cargo, allows PTX to be released in a modulated and controlled way. This may be explained supposing PTX acts as binding agent, thus higher PTX weight content in the matrix material makes the NPs possess greater hydrophobic character, leading to limited water entry into the NPs core.

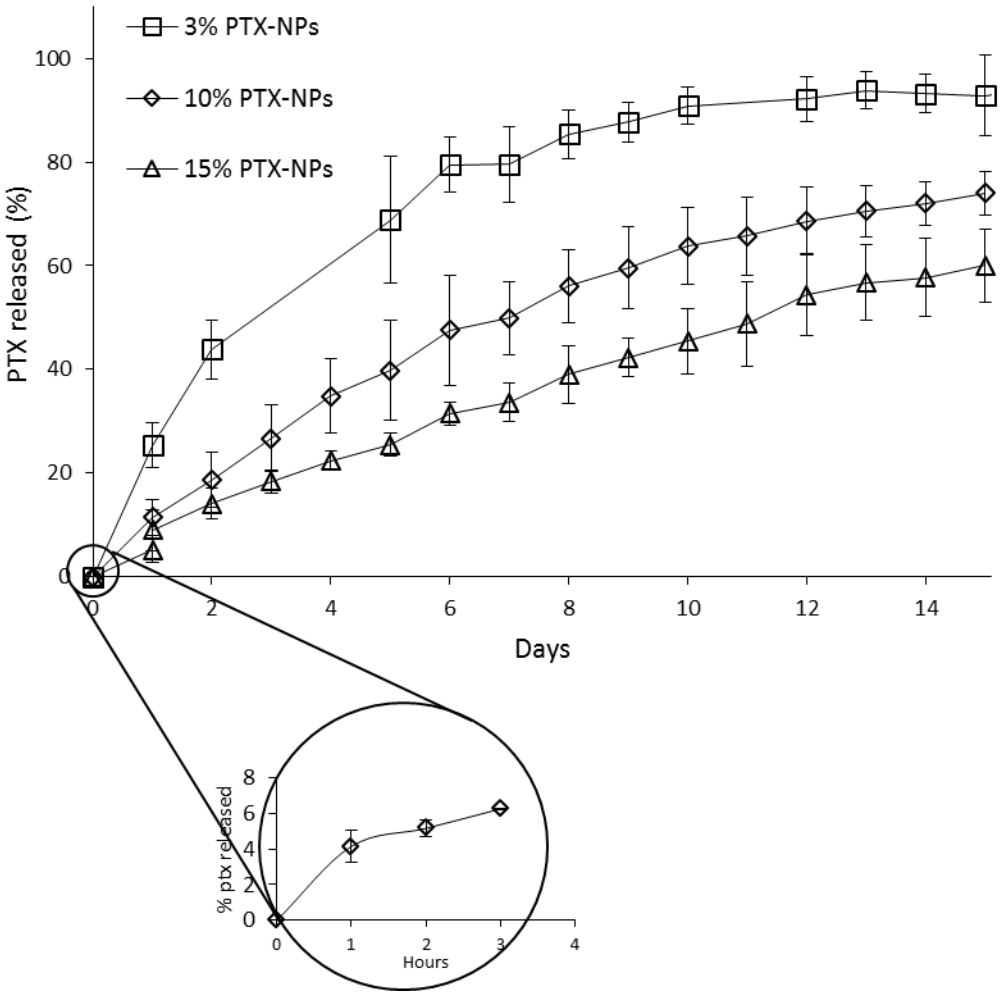


Figure 2.11 In vitro release kinetics of PTX from P co-polymer NPs at 3, 10, 15 % w/w theoretical drug content (PBS 0.1 M with 0.3 % v/v Tween-80, pH 7.4, 37º C) Mean ± SD (n=3)

Along with *in vitro* drug release we also analyzed the degradation products of the NPs. Polyester-based NPs undergoes degradation by hydrolysis or biodegradation through cleavage of its backbone ester linkages into oligomers and, finally monomers. This has been demonstrated in both *in vivo* and *in vitro* [33,34]. The degradation process for polyester-based NPs is mainly through uniform bulk degradation of the matrix only where the water penetration into the matrix is faster than the rate of the polymer degradation. Furthermore, the increase of carboxylic end groups as a result of biodegradation autocatalysis the process. The presence of the drug may alter the degradation mechanism

combining bulk erosion with surface degradation, as well as affect the rate of matrix degradation. We studied the degradation of the NPs in terms of formation of polymer degradation products, to ensure that PTX release was related with polymer degradation, and it could not be attributed to a simple diffusion of the encapsulated drug through the polymer core matrix. Therefore, we tried to indirectly demonstrate that drug release is a good indicator of the polymer degradation. Analyzing the drug release medium by UPLC-TOF-MS, at day 10, two groups of peaks, at high (Figure 2.12) and at low molecular weight (Figure 2.13) can be detected.

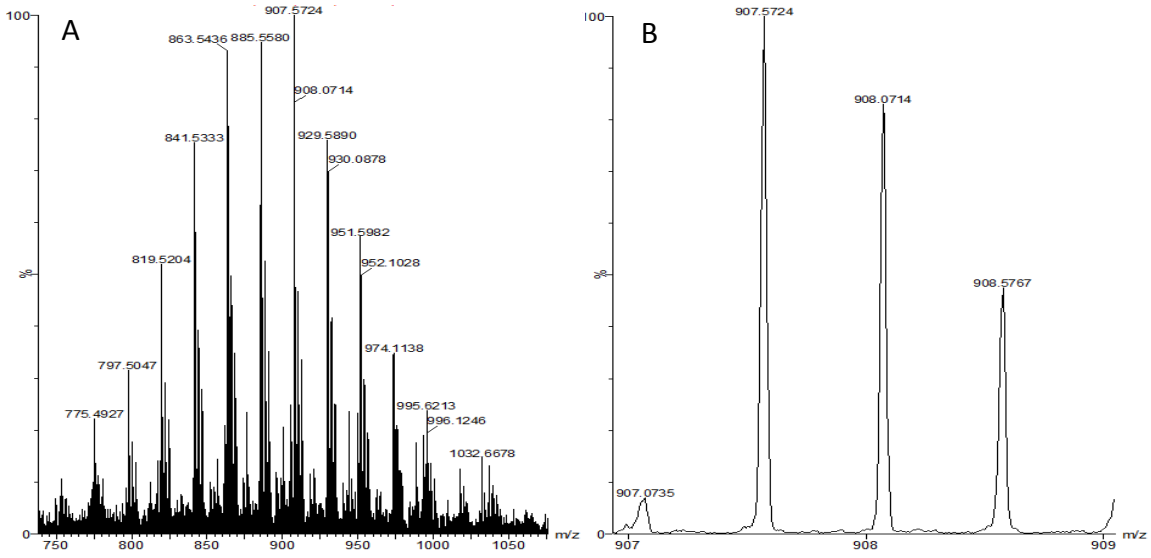


Figure 2.12 UPLC-MS spectrum of release medium at day 10; (A) high-molecular weight distribution; (B) spectrum zoomed on 907.5272 peak

Analyzing the mass spectrum (Figure 2.12 a) the product detected at high molecular weight can be identified as PEG with a molecular weight arount 1500 Da. This fact corroborated that PEG is one of the degradation byproducts of the polymer as expected. Also another family of peaks was identified with a molecular weight of 411.27 Da, as shown in Figure 2.13. This peak was identified as the hydrophobic polymeric chain of the polymer constituting NPs (see Figure 2.13) and confirms that the main mechanism of the polymer biodegradation is the hydrolysis of the polyester bond between the polyester block and the PEG moiety. These two families of degradation products were not found when the release medium was analyzed the first day of the release kinetic experiment.

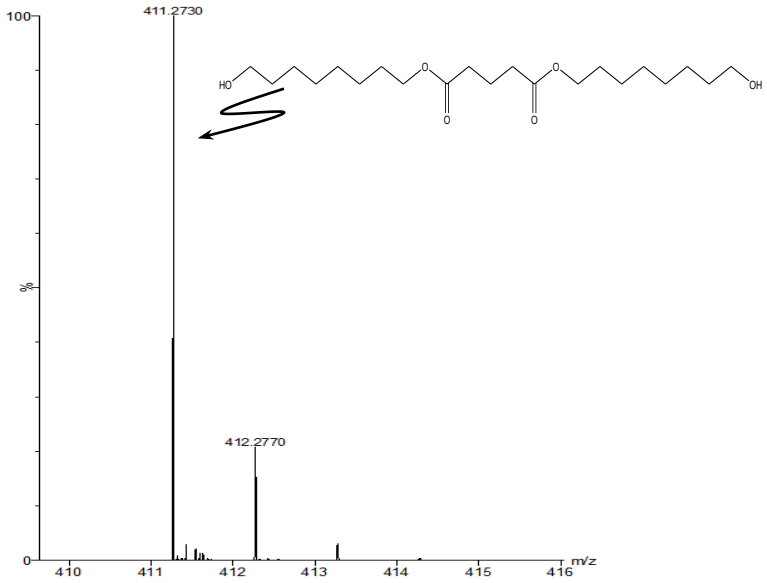


Figure 2.13 UPLC-MS spectrum of release medium at day 10, low molecular weight distribution

## Characterization of emulsion-based PTX NPs

Emulsioned NPs showed a size of 176.4 ± 2.5 nm with a polydispersity of 0.32 ± 0.02 and zeta potential of -39 ± 1.17 mV (Table 2.3). Unlike precipitated NPs, emulsioned NPs required lyoprotectant to assure optimal resuspension in water after freeze-drying. As shown in Table 2.3 various lyoprotectants were used and mannitol at 10% (w/v) allowed to obtain NPs with same characteristics prior to freeze-drying. Drug encapsulation studies showed an increase in drug content from 4 ± 0.4 to 11.7 ± 1 when the initial theoretical drug loading ranged from 3 to 12%. It's important to notice that the drug content was referred to freeze-dried NPs recovered, so the values shown were not taking into account the NPs recovery yield (data not shown). The results were expressed as mean ± S.D. for three replicate samples. The results confirm the versatility of block co-polymer P and demonstrate its capacity to be employed as a drug delivery system. Indeed, satisfactory findings about size, PDI, zeta-potential and drug content were obtained by using nanoprecipitation as though emulsification-solvent evaporation techniques.

Table 2.3 Mean particle size and size distribution (PDI) of emulsioned NPs in the absence or presence of different lyoprotectant

| Lyoprotectant used and concentration % (w/v) | Size (nm) ± S.D. | PDI ± S.D. |
|---|---|---|
| No freeze-dried | 176,4 ± 2,5 | 0,32 ± 0,0 |
| No Lyoprotectant | n.m. | 1 |
| Sucrose, 10 | 220,2 ± 1,1 | 0,31 ± 0,02 |
| Glucose, 10 | 195,1 ± 5,6 | 0,46 ± 0,05 |
| Lactose, 5 | 211,9 ± 3,4 | 0,24 ± 0,00 |
| Mannitol, 10 | 175,5 ± 3,8 | 0,33 ± 0,05 |
| Pva, 2 | 66,5 ± 17 | 0,9 ± 0,1 |

Table 2.4 D.C. (%) of emulsioned NPS

| Theoretical Drug Loading (%, w/w) | Drug Content % (w/w) ± S.D. |
|---|---|
| 3 | 4 ± 0.4 |
| 4 | 6,2 ± 0.6 |
| 8 | 8,2 ± 0.6 |
| 10 | 9,1 ± 1.1 |
| 12 | 11,7 ± 1 |

### 2.3.3 Cell experiments

#### *In vitro* immunological assay

Analyzing microscopic picture of the whole blood after NPs exposure, no change in morphology is observed on RBC's, white cell and platelets (data not shown). Our results highlight that NPs and PTX-NPs are not haemolytic (<2%). In regards to cells counting, no significant change was observed in RBC's, WBC's and platelet counting at the concentration evaluated. Analyzing C3a concentration by ELISA assay, no significant activation of complement is observed in presence of the NPs suspension. Along with complement system, no relevant activation of coagulation by intrinsic or the extrinsic pathway was remarked.

## *In vitro* anti-proliferative efficiency

The *in vitro* anti-proliferative effect of drug-free NPs and PTX-NPs on U-87 MG cells was evaluated using MTS assay and PTX as comparison. As shown in Figure 2.14 a and b no obvious cytotoxicity was observed for the drug-free NPs. The synthetized block co-polymer (P) biocompatibility was confirmed since the drug-free NPs showed no decrease in cellular viability. Cells were incubated with 3, 5 and 8 % PTX-NPs at 10 and 20 nM PTX concentrations. This range of concentrations was selected because it corresponds to plasma levels of the drug achievable in humans. As can be seen in Figure 2.14 a, a marked reduction in cell viability (10%) was observed when U-87 MG cells were incubated 11 days with 3% PTX-NPs at 10 nM. For the same incubation time, PTX showed similar toxicity than 3% PTX-NPs, otherwise for 5 and 8 % PTX-NPs a slighter effect was observed, with 76 and 80% survival rate, respectively. With increasing PTX concentration at 20 nM, a significant reduction in U-87 MG cells viability was achieved in shorter incubation times and for all formulation tested. As shown in Figure 2.14 b, at this concentration the cell growth was strongly inhibited after 4, 8 and 11 days for 3, 5, 8 % PTX-NPs, respectively, with a reduction of approximately 50% in cell viability. Again, PTX at 20 nM showed similar effect on U-87 MG cells than 3% PTX-NPs, indicating that the developed PTX-NPs system did not decrease the PTX activity on tumoral cells and that the cytotoxicity against U87 MG cells was in time- and drug concentration-dependent manner.

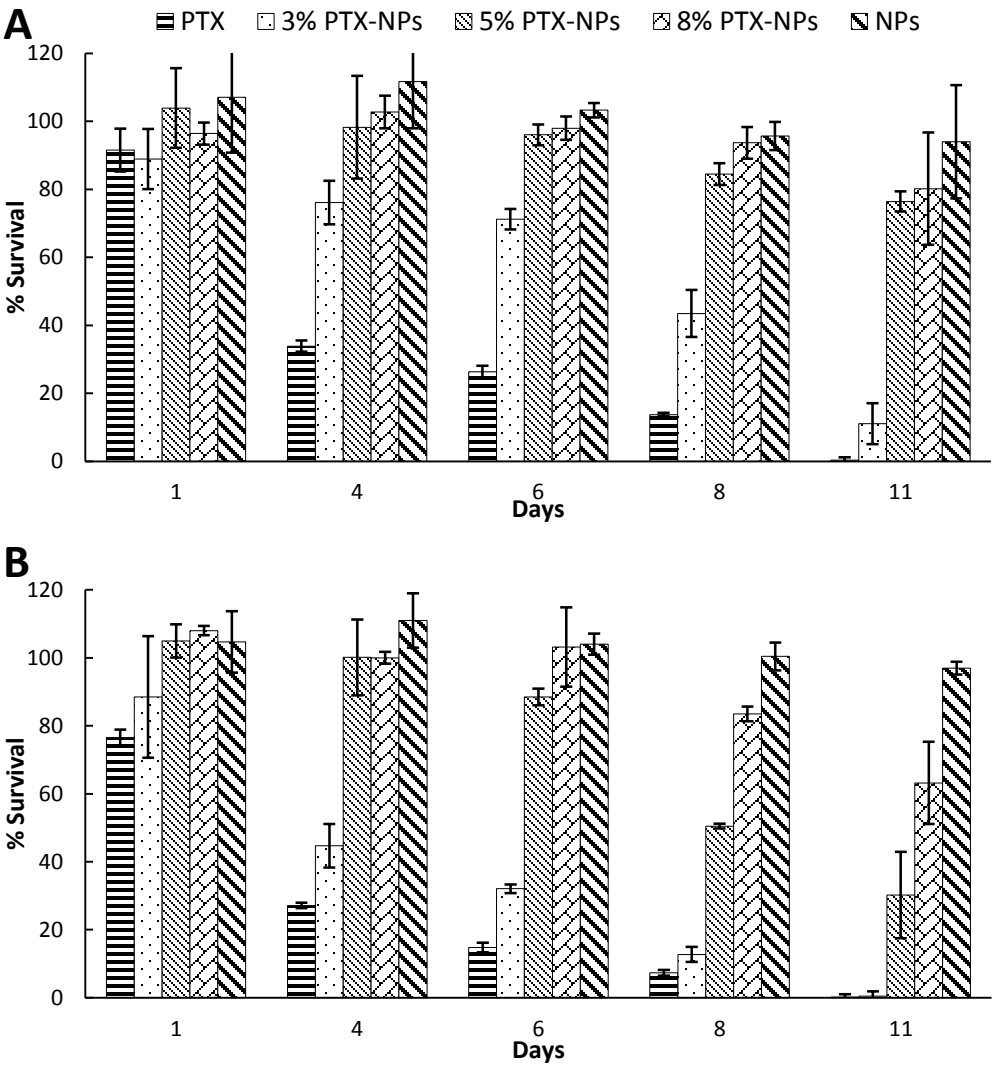


Figure 2.14 Cell viability on U-87 MG incubated with PTX, NPs (drug free) and 3, 5, 8 % PTX-NPs at (A) 10 and (B) 20 nM PTX concentration after 11 days cell culture (n=3)

## 2.4 Concluding Remarks

We have developed a nanoparticluate system for controlled release of the anticancer drug PTX. A novel block co-polymer (P) was successfully synthetized to obtain via nanoprecipitation or emulsification-solvent evaporation method, a very monodisperse PTX-NPs population. A clear correlation between NPs characteristics and formulation parameters was found in order to entirely customize NPs in terms of size, zeta-potential, drug loading and release profile. Selected PTX-NPs showed a spherical shape with particle size of 180 nm, polydispersity of 0.1 and with a surrounding PEG corona on the surface. PTX content of NPs was easily increased up to 24% (w/w) limited only by the physical state change of the drug (amorphous < 15%). High D.C. makes the system suitable for intravenous administration since only low concentrated PTX solutions can be injected due to the side effects related to its vehicle. High D.C. was probably due to strong lipophilic interactions of PTX with hydrophobic inner region of NPs. Consequently, *in vitro* PTX release from NPs, exhibiting an approximately first-order profile, depended on total cargo, with complete release approximately in 12 days for 3% theoretically loaded NPs. Higher PTX loaded NPs, limiting water entry, showed a similar trend, characterized by absence of initial burst release but with a slower release of approximately 54% and 45% for 10% and 15%, respectively, at day 9. *In vitro* cellular studies demonstrated that block co-polymer-based NPs were biocompatible, and the PTX loaded NPs had significant *in vitro* anti-tumoral activity against human primary glioblastoma cell line (U-87 MG). The cytotoxicity against U87 MG for PTX-NPs was time- and drug concentration-dependent. The developed NPs showed to fully accomplish all requirements for a proper drug delivery system but an efficacious targeting is required to improve therapeutic index and avoid the adverse effect of an uncontrolled release. In the next chapter (Chapter III) the suitability of the system for targeting NPs is investigated by functionalizing NPs surface with target-specific ligands.

## 2.5 Rerefences


1. R. Tong and J. Cheng, Ring-opening polymerization-mediated controlled formulation of polylactide-drug nanoparticles., J. Am. Chem. Soc. 131**,** 4744–54 **(2009)**

2. X. D. S. Zhou, J. Xu, H. Yang, Synthesis and characterization of biodegradable poly(e-caprolactone)-polyglycolide-poly(ethylene glycol) monomethyl ether random copolymer., Macromol. Mater. Eng 289**,** 576–580 **(2004)**

3. J. Cheng, B. a Teply, I. Sherifi, J. Sung, G. Luther, F. X. Gu, E. Levy-Nissenbaum, A. F. Radovic-Moreno, R. Langer and O. C. Farokhzad, Formulation of functionalized PLGA-PEG nanoparticles for in vivo targeted drug delivery., Biomaterials 28**,** 869–76 **(2007)**

4. P. Couvreur, C. Dubernet and F. Puisieux, Controlled drug delivery with nanoparticles : current possibilities and future trends, Eur. J. Pharm. Biopharm. 41**,** 2–13 **(1995)**

5. H. Fessi, F. Puisieux, J. P. Devissague1, N. Ammoury and S. Benita, Nanocapsule formation by interfacial polymer deposition following solvent displacement, Int. J. Pharm. 55**,** R1–R4 **(1989)**

6. U. Bilati, E. Allémann and E. Doelker, Development of a nanoprecipitation method intended for the entrapment of hydrophilic drugs into nanoparticles., Eur. J. Pharm. Sci. 24**,** 67–75 **(2005)**

7. J. Nicolas, S. Mura, D. Brambilla, N. Mackiewicz and P. Couvreur, Design, functionalization strategies and biomedical applications of targeted biodegradable/biocompatible polymer-based nanocarriers for drug delivery., Chem. Soc. Rev. 42**,** 1147–235 **(2013)**

8. Y. Li, Y. Pei, X. Zhang, Z. Gu, Z. Zhou, W. Yuan, J. Zhou, J. Zhu and X. Gao, PEGylated PLGA nanoparticles as protein carriers: synthesis, preparation and biodistribution in rats., J. Control. Release 71**,** 203–11 **(2001)**

9. R. Tong and J. Cheng, Paclitaxel-initiated, controlled polymerization of lactide for the formulation of polymeric nanoparticulate delivery vehicles., Angew. Chem. Int. Ed. Engl. 47**,** 4830–4 **(2008)**

10. S. Essa, J. M. Rabanel and P. Hildgen, Effect of polyethylene glycol (PEG) chain organization on the physicochemical properties of poly(D, L-lactide) (PLA) based nanoparticles., Eur. J. Pharm. Biopharm. 75**,** 96–106 **(2010)**

11. D. S. Moghimi SM, Innovations in avoiding particle clearance from blood by Kupffer cells: cause for reflection., Crit Rev Ther Drug Carr. Syst 11**,** 31–59 **(1994)**

12. D. S. Moghimi SM, Porter CJ, Muir IS, Illum L, Non-phagocytic uptake of intravenously injected microspheres in rat spleen: influence of particle size and hydrophilic coating., Biochem Biophys Res Commun 177**,** 861–866 **(1991)**

13. S. M. Moghimi, a C. Hunter and J. C. Murray, Nanomedicine: current status and future prospects., FASEB J. 19**,** 311–30 **(2005)**

14. D. E. Owens and N. a Peppas, Opsonization, biodistribution, and pharmacokinetics of polymeric nanoparticles., Int. J. Pharm. 307**,** 93–102 **(2006)**

15. K. J. Hamblett, P. D. Senter, D. F. Chace, M. M. C. Sun, J. Lenox, C. G. Cerveny, K. M. Kissler, S. X. Bernhardt, A. K. Kopcha, R. F. Zabinski, D. L. Meyer and J. A. Francisco, Effects of Drug Loading on the Antitumor Activity of a Monoclonal Antibody Drug Conjugate Effects of Drug Loading on the Antitumor Activity of a Monoclonal Antibody Drug Conjugate, Clin Cancer Res 10**,** 7063–7070 **(2004)**

16. T. Musumeci, C. a Ventura, I. Giannone, B. Ruozi, L. Montenegro, R. Pignatello and G. Puglisi, PLA/PLGA nanoparticles for sustained release of docetaxel., Int. J. Pharm. 325**,** 172–9 **(2006)**

17. K. S. Soppimath, T. M. Aminabhavi, a R. Kulkarni and W. E. Rudzinski, Biodegradable polymeric nanoparticles as drug delivery devices., J. Control. Release 70**,** 1–20 **(2001)**

18. H. Gelderblom, J. Verweij, K. Nooter and A. Sparreboom, Cremophor EL: the drawbacks and advantages of vehicle selection for drug formulation, Eur. J. Cancer 37**,** 1590–1598 **(2001)**

19. S. M. Spratlin J, Pharmacogenetics of paclitaxel metabolism., Crit Rev Oncol Hematol. 61**,** 222–229 **(2007)**

20. J. Marcel Musteata, F., Pawliszyn, Determination of free concentration of paclitaxel in liposome formulation., J. Pharm. Pharm. Sci. 9**,** 231–237 **(2006)**

21. A. Budhian, S. J. Siegel and K. I. Winey, Haloperidol-loaded PLGA nanoparticles: systematic study of particle size and drug content., Int. J. Pharm. 336**,** 367–75 **(2007)**

22. V. Y. Senichev and V. V Tereshatov, in Handb. solvents edited G. Wypych,ChemTec Publishing 101–214 **(**2001**)**

23. O. Thioune, H. Fessi, J. P. Devissaguet and F. Puisieux, Preparation of pseudolatex by nanoprecipitation: Influence of the solvent nature on intrinsic viscosity and interaction constant, Int. J. Pharm. 146**,** 233–238 **(1997)**

24. L. Mu and S. S. Feng, Vitamin E TPGS used as emulsifier in the solvent evaporation/extraction technique for fabrication of polymeric nanospheres for controlled release of paclitaxel (Taxol)., J. Control. Release 80**,** 129–44 **(2002)**

25. C. Fonseca, S. Simões and R. Gaspar, Paclitaxel-loaded PLGA nanoparticles: preparation, physicochemical characterization and in vitro anti-tumoral activity., J. Control. Release 83**,** 273–286 **(2002)**

26. F. Danhier, N. Lecouturier, B. Vroman, C. Jérôme, J. Marchand-Brynaert, O. Feron and V. Préat, Paclitaxel-loaded PEGylated PLGA-based nanoparticles: in vitro and in vivo evaluation., J. Control. Release 133**,** 11–7 **(2009)**

27. G. Gaucher, R. H. Marchessault and J.-C. Leroux, Polyester-based micelles and nanoparticles for the parenteral delivery of taxanes., J. Control. Release 143**,** 2–12 **(2010)**

28. Q. Hu, X. Gao, G. Gu, T. Kang, Y. Tu, Z. Liu, Q. Song, L. Yao, Z. Pang, X. Jiang, H. Chen and J. Chen, Glioma therapy using tumor homing and penetrating peptide-functionalized PEG-PLA nanoparticles loaded with paclitaxel., Biomaterials 34**,** 5640–50 **(2013)**

29. Q. Hu, G. Gu, Z. Liu, M. Jiang, T. Kang, D. Miao, Y. Tu, Z. Pang, Q. Song, L. Yao, H. Xia, H. Chen, X. Jiang, X. Gao and J. Chen, F3 peptide-functionalized PEG-PLA nanoparticles co-administrated with tLyp-1 peptide for anti-glioma drug delivery., Biomaterials 34**,** 1135–45 **(2013)**

30. G. Wang, B. Yu, Y. Wu, B. Huang, Y. Yuan and C. S. Liu, Controlled preparation and antitumor efficacy of vitamin E TPGS-functionalized PLGA nanoparticles for delivery of paclitaxel., Int. J. Pharm. 446**,** 24–33 **(2013)**

31. L. Mu and S.-S. Feng, PLGA/TPGS nanoparticles for controlled release of paclitaxel: effects of the emulsifier and drug loading ratio., Pharm. Res. 20**,** 1864–72 **(2003)**

32. H. Xin, L. Chen, J. Gu, X. Ren, Z. Wei, J. Luo, Y. Chen, X. Jiang, X. Sha and X. Fang, Enhanced anti-glioblastoma efficacy by PTX-loaded PEGylated poly(ε-caprolactone) nanoparticles: In vitro and in vivo evaluation., Int. J. Pharm. 402**,** 238–47 **(2010)**

33. M. Ramchandani and D. Robinson, In vitro and in vivo release of ciprofloxacin from PLGA 50:50 implants., J. Control. Release 54**,** 167–75 **(1998)**

34. L. C. Amann, M. J. Gandal, R. Lin, Y. Liang and S. J. Siegel, In vitro-in vivo correlations of scalable PLGA-risperidone implants for the treatment of schizophrenia., Pharm. Res. 27**,** 1730–7 **(2010)**

# CHAPTER III.

## NPs' Peptide-functionalization and *In Vitro* evaluation of dual targeting effect

## 3.1 Introduction

The previous chapter (Chapter II) has shown the complete development and characterization of a tailored nanoparticulate system for controlled release of anticancer drug PTX. It has been demonstrated how NPs characteristics can be customized to obtain high PTX loaded NPs that can improve therapeutic index and avoid an uncontrolled release. As discussed in Chapter I, NPs have several advantages as delivery vehicles that make them useful for cancer therapy. The small size for example, allows nanoparticles to overcome many biological barriers, access tumor tissue through porous vasculature [1,2], and achieve cellular uptake [3]. However, a careful engineering of polymeric nanoparticles including functionalization with targeting ligands is needed to promote receptor mediated uptake into the cancer cells.

In addition to NPs' surface engineering to increase blood circulation and influence biodistribution [4], in recent years different investigations about targeting ligands attached to the surface and their effect on the uptake by target tissue have been carried out [5]. Encapsulation of chemotherapeutic drugs inside targeted nanoparticles can further increase the therapeutic index by delivering an elevated dose directly to a tumor while limiting systemic toxicity [6]. As described in Chapter I and II, NPs consist of several components (Scheme 3.1) that can be engineered based on the desired application. Considerations of each component are necessary when designing a delivery system because each component affects the overall performance of the system. In addition to the components discussed in the previous chapter (core, corona, and payload), this chapter describes the use of targeting ligands with the aim to enhance cellular uptake through binding and endocytosis.

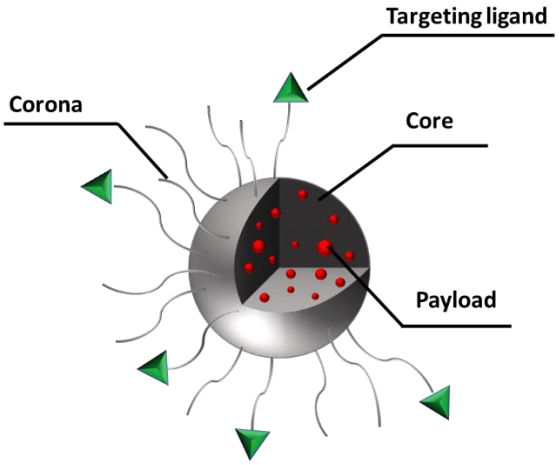


Scheme 3.1 Components of a nanoparticle delivery system

The global market for drugs for the central nervous system (CNS) is greatly underpenetrated and would have to grow by over 500% just to be comparable to the global market for cardiovascular drugs [7]. As it has been described in Chapter I, the main reason for this under-development of the global brain drug market is that the great majority of drugs do not cross the brain capillary wall, which forms BBB *in vivo*. There are only a few diseases of the brain that consistently respond to lipide-soluble-low MW small-molecule therapeutics [7–9]. In contrast, many other serious disorders of the brain, including neurodegenerative diseases, do not respond to conventional therapeutics. Alzheimer's disease, Parkinson's disease, amyotrophic lateral sclerosis and brain tumors are now representing the largest and fastest growing area of unmet medical needs. Glioblastoma multiforme (GBM), one of the most malignant brain tumors, accounting for about 40% of all brain tumors, remains a big challenge due to its highly proliferative, infiltrative and invasive property. Advances in neuroscience have resulted in development of new therapeutic agents for potential use in the central nervous system (CNS). Unfortunately, the therapeutic effect of brain disorders by drug treatment (such as chemotherapy, essential in the auxiliary treatment of glioma) is limited by the presence of the BBB, which protects the CNS from potentially harmful molecules to ensure optimal environment for brain function, but at the same time, excludes more than 98% of small molecule candidates drugs and almost 100% of large molecule drugs [10,11]. BBB

permeability is the rate-limiting factor for the penetration of pharmacological agents into CNS [12]. The BBB is mainly formed by brain capillary endothelial cells (EC) that are closely sealed by tight junctions. Receptor-mediated endocytosis is one of the mechanism through which drug carriers cross the BBB. Different transporters and receptors present at the BBB have been described as playing roles in maintaining the integrity of the BBB and brain homeostasis. Among them, low-density lipoprotein receptor-related protein (LRP), a member of the low-density lipoprotein receptor family (LDLR), highly expressed on BBB [13], has been reported to possess the ability to mediate transport of ligands across EC of the BBB [13–15]. Furthermore, LRP is also over-expressed on human glioma cells [16,17], making LRP a potential targeted receptor for brain tumor drug delivery systems, with dual-targeting capability for both BBB and glioma cells.

The anticancer drug paclitaxel (PTX), isolated from the bark of *Taxus brevifolia*, has been proved effective in the treatment of a wide variety of tumors, among them GBM [18]. However, the application of PTX is compromised due to its poor aqueous solubility and serious adverse effects associated with the solvent Cremophor EL-ethanol [19]. Furthermore, nonspecific systemic distribution of PTX commonly gives rise to dose-dependent toxic effects and poor therapeutic outcomes.

To overcome these disadvantages, various drug delivery systems, such as liposomes [20], nanoparticles (NPs) [21,22], polymer drug conjugates [23] and micelles [24], have been developed from different viewpoints. Among them, biodegradable polymeric NPs in the range 70-200 nm, due to their loading capacity for highly insoluble drugs, have been successfully utilized to entrap PTX, achieving less PTX-associated side effects as well as better therapeutic benefits over commercial Taxol [25]. Furthermore, surface modifications through physical absorption of a hydrophilic polymer synthesis or amphiphilic co-polymers were widely applied in order to develop long-circulating NPs, minimizing the absorption of opsonins and thereafter the removal from the blood [5,26]. A series of hydrophilic polymers

have been attempted to decorate the NPs surface, such as poly(ethylene glycol) PEG [27,28] or methoxy poly(ethylene glycol) (MPEG) [29].

As a result, this chapter seeks to convert NPs into an effective target drug delivery system for efficiently transport and release active drug molecules. The developed strategy allows to select the target by functionalizing NPs with a family of peptides containing cysteine (Cys, C) residues, thus allowing an efficacious and targeted delivery with minimal systemic side effects due to nonspecific uptake by healthy tissues. In this chapter, a dual-targeting drug delivery system was developed by functionalization with a family of peptides, known to be efficiently transported across the BBB by LRP-mediated transcytosis, to shuttle drug from blood to brain, and then target glioma cells.

In addition to the block co-polymer P discussed in Chapter II, a novel biodegradable block co-polymer 2P was synthetized. A nanoprecipitation technique with modification of a previously described (Chapter II) method was developed to obtain dual-targeting functionalized NPs with monodisperse particles size, external hydrophilic coating and high drug content for the anticancer drug PTX delivery.

The physicochemical characterization involves *in vitro* release profile, cellular uptake and anti-glioma effect on human primary glioblastoma cell line (U-87 MG) and Bovine Brain Endothelial Cells (BBMVECs). Moreover, to confirm the dual-targeting effect, BBB crossing properties *in vitro* were investigated by transendothelial transport experiments in an *in vitro* BBB model, developed from the expertise of our group.

## 3.2 Experimental Section

### 3.2.1 Materials

1.8-Octanediol (98%) 2.2'-Dithiodipyridine (≥97%) and PEG ($M_w$ 1.5 KDa) were purchased from Sigma (Sigma-Aldrich, USA). Glutaric acid (99%) was obtained from Alfa Aesar (USA). AGBBB015F (CGGKTFFYGGSRGKRNNFKTEEY) and Regulon (HKKWQFNSPFVPRADEPARKGKV HIPFPLDNITCRVPMAREPTVIHGKREVTLHLHPDH) peptides fluorescently labeled with carboxyfluorescein and 5-Tamra, respectively, were synthesized by Innovagen AB (Sweden). PEG Thiol acid, α-Thio-ω-carboxy poly (ethylene glycol) ($M_W$ 3.000 Da) was supplied by Iris Biotech GmbH (Germany). PTX (≥ 97%) was provided by Yunnan Hande Bio-Tech CO, LTD, P.R. China. FBS was purchased from Lonza (Spain), L-Glutamine and Penicillin/Streptomycin were provided by Labclinics. All other chemicals of analytical grade were purchased from Sigma (Sigma–Aldrich, Germany).

### 3.2.2 Synthesis of peptide-conjugate Block Co-Polymer 2P

#### Synthesis of Linker

To an oven dried one-necked flask under nitrogen at RT equipped with a stir bar, 2,2'-dithiodipyridine ($M_W$:220.31, 66.4 mg, 2.14 mmol) in 5 ml THF and 0.5 ml AcOH purged with nitrogen was added. To this mixture, α-Thio-ω-carboxy poly (ethylene glycol) ($M_W$ 3317 Da, 500 mg, 1.07 mmol) dissolved in few ml of THF was added dropwise. The solution turned yellow and was allowed to stir for three days. After completion of the reaction, TLC analysis was performed, using 90% DCM and 10% MeOH to verify the presence of non-reacted 2,2'-dithiodipyridine. The product was then precipitated in 100 ml of hexane under low magnetic stirring. The solution was refrigerated overnight at 8-10°C and placed in conical tubes, and after a short vortex agitation two centrifuge cycles were performed, at 2700 g for 15' and at 1300 g for 20', respectively. After each cycle the supernatant was removed and analyzed by TLC, the same amount of hexane was added and a short vortex agitation to redisperse the pellet was performed. Residual solvent was

removed under vacuum and to yield the product as a yellow solid (0.5165 g), which was analyzed using TLC under the above-mentioned conditions.

## Synthesis of 15F and Reg Peptide-Targeted Linker

Sulfhydryls is present in AGBBB015F (15F) and REG peptides in the side-chain of cysteine (Cys, C) AA. Pairs of cysteine sulfhydryl groups were linked by disulfide bonds (–S–S–) to the linker. Sulfhydryl-reactive chemical groups include pyridyl disulfides that react with sulfhydryl groups at physiologic pH to form disulfide bonds. During the reaction, a disulfide exchange occurs between the molecules –SH group and the reagent's 2-pyridyldithiol group; as a result, pyridine-2-thione is released. The coupling between Cys peptides and linker was carried out in 5 ml PBS (10 mM, pH 7.4) weighing accurately 1 mol of linker and 1.05 mol of peptide. The reaction was stirred at 0 °C for 4 hours. The progress of the reaction was monitored by TLC, showing total conversion of the starting material. The solution was lyophilized to yield Peptide-Targeted Linker as a white powder.

## Synthesis of pre-polymer P* and block co-polymer 2P

The preliminary step was the production of pre-polymer P* which took place in the microwave reactor by reacting glutaric acid and 1.8-octanediol at a feeding ratio of 1:1.2 (molar) at 100 W for 1 hour. The reaction was performed under the same conditions as described in Chapter II. In this way a pre-polymer P* was obtained with an excess of 1.8-octanediol which can react with the linker. This last reaction took place in the microwave reactor with the same conditions above and with a ratio 1:1 (w/w) between preformed peptide-targeted linker and pre-polymer P*.

## Synthesis of fluorescently labeled 3P block co-polymer

To an oven dried one-necked flask at RT equipped with a stir bar, 20 mol of α-Thio-ω-carboxy poly (ethylene glycol) ($M_W$ 3073 Da) in 2 ml mQ water (pH 7) were added. To this mixture, 1 mol of the orange/red fluorescent dye (Alexa Fluor® 568) ($M_W$ 880.92 Da)

dissolved in few ml of water (pH 7) was added. The solution was allowed to stir for two hours. After completion of the reaction, TLC analysis was performed, using 70% DCM and 30% MeOH to verify the presence of non-reacted α-Thio-ω-carboxy poly (ethylene glycol). Next step was the production of pre-polymer P* which took place in the microwave reactor by reacting glutaric acid and 1.8-octanediol at a feeding ratio of 1:1.2 (molar) at 100 W for 1 hour. The reaction was performed under the same conditions as described in Chapter II. In this way a pre-polymer P* was obtained with an excess of 1.8-octanediol which can react with the fluorescently labeled α-Thio-ω-carboxy poly (ethylene glycol). This last reaction took place in the microwave reactor with the same conditions above and with a ratio 1:2 (w/w) between preformed fluorescently labeled α-Thio-ω-carboxy poly (ethylene glycol) and pre-polymer P*.

### 3.2.3 Characterization of Block Co-Polymer (2P)

The composition of the 2P block co-polymers was determined by proton nuclear magnetic resonance $^{1}$H-NMR in $CDCl_3$ at 300 MHz (Varian 400 MR). The weight-averaged molecular weight (Mw) and molecular weight distribution (P.I. = polydispersity index) of the obtained polymers were determined by gel permeation chromatography (GPC) using a LaChrome Elite chromatograph (Hitachi) equipped with a refractive index (RI) detector. A Shodex KF-603 column was used as stationary phase, and HPLC grade THF was used as the mobile phase at a flow rate of 0.5 ml/min. The samples were dissolved in THF and filtered previous to injection (injection volume = 20 µl). The molecular weights of the copolymers were determined relative to the standards curve, prepared using a series of Shodex SM-105 polystyrene standards. MALDI-TOF mass spectra were determined using a Microflex – Bruker Daltonics (Bruker Corporation, Germany). Polymer samples were spotted for analysis using a dried-droplet method. For each sample, the polymers were first dissolved in a TA solution of water, acetonitrile and TFA (50%, 50% and 0.1%, respectively). A fresh saturated solution of matrix material was prepared by mixing the matrix powder of ACCA (α-Cyano-4-hydroxycinnamic acid) with TA solution. Then 100 µl of the supernatant matrix

solution was mixed with the 10 µl of sample. A 1 µl droplet of the resulting mixture was placed on the mass spectrometer's sample stage, and then the droplet was dried at room temperature.

### 3.2.4 Preparation of 15F and REG peptide-functionalized PTX-NPs

The nanoprecipitation technique was applied to prepare peptide-functionalized PTX-NPs with modification of the method reported in Chapter II. Briefly, block co-polymers P, 2P and if required 3P, at different ratio (w/w) and PTX were dissolved in 1 ml of acetone to form the diffusing phase. This phase was then added to 20 ml of milliQ water, by means of a syringe, controlled by a syringe pump (KD Scientific), positioned with the needle directly in the medium, under magnetic stirring at room temperature. The resulting nanoparticles suspension was allowed to stir uncovered to allow the evaporation of acetone. Drug free nanoparticles were prepared according to the same procedure. The suspension was purified by centrifugation (Hettich Centrifuge, EBA 21, 4000 g, 45 min at RT) with ultracentrifugal devices (Amicon Ultra-15, Ultracel membrane with 100,000 MWCO, Millipore, USA). The supernatant was discarded and the pellet freeze-dried for 48 hours.

### 3.2.5 Characterization of 15F and REG-functionalized-PTX-NP

#### Size, morphology and zeta potential

The NPs size distributions and polydispersity were measured by dynamic light scattering (Malvern Zeta Sizer Nano Series) at 25ºC and at scattering angle of 90º using samples appropriately diluted with mQ water. For each sample the intensity-weighted mean value was recorded as the average of three measurements. The results were expressed as mean ± standard deviation (mean ± S.D) for two replicate samples. Further measurements were performed by nanoparticles tracking analysis (NTA, Nanosight LM 10, Laser Module LM 14C), with a 532 nm laser beam passed through a prism-edged optical flat and validating

all data with video files of the NPs moving under Brownian motion to determinate NPs size distribution and to confirm the monodispersity of the NPs solution. NPs were also characterized with respect to zeta (ζ) potential, the analysis was performed in triplicate on Malvern ZetaSizer (Nano Series) with a Smoluchowsky constant F ($K_a$) of 1.5 to achieve zeta potential values from electrophoretic mobility. For each sample the mean zeta potential was recorded as the average of three measurements. The results were expressed as mean ± S.D for two replicate sample. The size and morphology of the NPs were observed by Transmission Electron Microscopy (TEM) (Jeol Jem 2011). A drop of the NPs suspension (10 µl) was placed on carbon electron microscopy grids (Holey Carbon Film) and air-dried before analyze at an acceleration voltage of 200 kV without negative staining.

## Drug encapsulation efficiency

Freeze-dried NPs loaded with PTX were dissolved in acetonitrile and the amount of entrapped drug was detected by UPLC (Waters ACQUITY UPLC H-Class). A reverse phase BEH C18 column (1.7 µm 2.1 x 50mm) was used as stationary phase. The mobile phase consisted of a mixture of acetonitrile and water (60:40 v/v) at a flow rate of 0.6 ml/min. Paclitaxel was quantified by UV detection (λ=227 nm, Waters TUV detector). A calibration curve of standard paclitaxel solution was used to obtain the paclitaxel concentration, which was linear over the range of 60.5 – 0.47 µg/ml with a correlation coefficient of $R^2$=0.9998. Drug incorporation efficiency was expressed as drug content (% w/w) and drug entrapment (%); represented by Equation 3.1 and Equation 3.2, respectively. For each sample the mean value was recorded as the average of three measurements. The results were expressed as mean ± S.D for two replicate.

$$\text{Drug Content}\left(\%\frac{\text{w}}{\text{w}}\right) = \frac{\text{Mass of drug in NPs } \times 100}{\text{Mass of NPs recovered}}$$

Equation 3.1

$$\text{Drug Entrapment}(\%) = \frac{\text{Mass of drug in NPs } \times 100}{\text{Mass of drug used in formulation}}$$

Equation 3.2

## Thermal characterization

The physical state (crystalline *versus* amorphous) and miscibility of Paclitaxel in the NPs were characterized by differential scanning calorimetry (DSC Mettler Toledo DSC821e) on glass transition temperature ($T_g$) or melting point ($T_m$). Pure paclitaxel was analyzed as the control. Experimentally, 4-5 mg of each sample were sealed in a standard aluminum pan and purged with dry nitrogen at a flow rate of 50 ml/min while the sample was heated from 50ºC to 300ºC (temperature ramp of 10ºC/min).

## In-vitro PTX release

*In vitro* drug release from PTX loaded NPs was performed using a modified dialysis-bag diffusion technique, as reported by Kim et al. and Averineni et al. [30,31]. Specifically, a known amount of freeze-dried peptide-functionalized-PTX-NPs, corresponding to 0.3 mg of PTX, was suspended in a dialysis bag (regenerated cellulose tubular membrane, Cellu SEP® T2, nominal MWCO 6000‑8000, membrane filtration products, Inc, TX) containing 15 ml of release PBS solution (0.1 M at pH 7.4 and 0.3% v/v of Tween-80). The bag containing NPs suspension was placed in a 50 ml Eppendorf® Tube (Fisher Scientific Company, Houston, TX) containing 30 ml of release medium (PBS solution and 0.3% v/v of Tween-80). The whole system was then placed in an orbital shaking incubator (LM-450D, Yihder Co., Ltd) at 37°C and at shaking speed of 200 rpm. At pre-decided time points, 1 ml aliquots of release medium were withdrawn and replaced with an equal volume of fresh medium to maintain the sink conditions. Aliquots were filtered through a 0.2 µm syringe filter directly into UPLC vials and immediately capped. The amount of PTX released in each time interval was determined by UPLC with a reverse phase BEH C18 column (1.7 µm 2.1×50 mm) as stationary phase and a mixture of Acetonitrile/Ammonium Acetate Buffer (20 mM, pH 4.5) = 60/40 at a flow rate of 0.6 ml/min as the mobile phase. PTX was quantified by UV detection (λ=227 nm, Waters TUV detector); the reported values are

averages ± S.D. of three replicates. The percent drug release was calculated as percentage of the total encapsulated drug.

## Peptide-conjugation efficiency by Fluorometric assay

To quantify 15F and REG peptide on the NPs surface, lyophilized NPs solutions at c.a. 15 mg/ml were analyzed by using a fluorimeter (Horiba Scientific, Fluoromax-4). Intensity and wavelength distribution of the emission spectrum after excitation at $\lambda_{exc}$ = 400 nm (15F) and 500 nm (REG peptide) were studied. For each sample the intensity mean value was recorded as the average of three measurements. 15F and REG conjugation efficiency (CE %) was calculated using Equation 3.3, in order to determine the percentage of peptide conjugated to the NPs surface.

$$\text{Conjugation Efficiency}(\%) = \frac{\text{Amount of peptide conjugated on the NPs surface}}{\text{Total amount of peptide added}}$$

Equation 3.3

## Peptide-conjugation efficiency by Amino Acids analysis

Quantification of REG peptide decoration onto NPs surface was carried out by UPLC amino acids analysis. The Waters UPLC Amino Acid Analysis (AAA) Kit is based on a derivatizing reagent for amino acid analysis. 6-aminoquinolyl-N-hydroxysuccinimidyl carbamate is an N-hydroxysuccinimide-activated heterocyclic carbamate, a class of amine-derivatizing compounds. 6-aminoquinolyl-N-hydroxysuccinimidyl carbamate converts both primary and secondary amino acids to stable derivatives. Prior to the analysis, REG-functionalized-PTX-NP were hydrolyzed in 6M HCl (20 hours, 110ºC) at peptide concentration 1 mg/ml, followed by evaporation of HCl under $N_2$ and reconstituted in 0.1M HCl with borate buffer and then with derivatizing agent. Derivatization was carried out at 55ºC for 10 minutes. Analytical UPLC was performed using an ACCQ-TAG column ULTRA C18 (1.7 µm 2.1 x 100mm) in UPLC Waters ACQUITY UPLC H-Class. The parameters of analysis, eluents and gradient are shown in Table 3.1. Amino acids identification and quantification were

determined relative to the calibration standard obtained by internal method. Briefly, to prepare a 2.5 mM internal standard stock solution of norvaline, 2.94 mg of norvaline were added to 10 mL 0.1 N HCl. Mix 70 µl of Ultra Borate buffer with 10 µl of calibration standard and 20 µl of reconstituted derivatizing agent, and vortex for several seconds before heating the vial for 10 minutes at 55 °C.

Table 3.1 Gradient table for hydrolyzed sample. Eluent: (A) 0.1% Formic Acid/water, (B) Water/acetonitrile (90:10 v/v), (C) Water, (D) Acetonitrile. Detection wavelength 260 nm, flow rate 700 µl/min

| STEP | TIME (min) | % A | %B | % C | % D |
|---|---|---|---|---|---|
| **1** | 0.00 | 10.0 | 0.0 | 90.0 | 0.0 |
| **2** | 0.29 | 9.9 | 0.0 | 90.1 | 0.0 |
| **3** | 5.49 | 9.0 | 80.0 | 11.0 | 0.0 |
| **4** | 7.10 | 8.0 | 15.6 | 57.9 | 18.5 |
| **5** | 7.3 | 8 | 15.6 | 57.9 | 18.5 |
| **6** | 7.69 | 7.8 | 0.0 | 70.9 | 21.3 |
| **7** | 7.99 | 4.0 | 0.0 | 36.3 | 59.7 |
| **8** | 8.59 | 4.0 | 0.0 | 36.3 | 59.7 |
| **9** | 8.68 | 10.0 | 0.0 | 90.0 | 0.0 |
| **10** | 10.20 | 10.0 | 0.0 | 90.0 | 0.0 |

### 3.2.6 Cell experiment

## Cell culture

Bovine Brain Endothelial Cells (BBMVECs) and attachment factor solution were purchased from Cell Applications. U-87 MG (glioblastoma-astrocytoma) cells were provided by ATCC (Spain). Both were cultured in DMEM (Sigma, D5671) and FBS (Lonza, DE14-801F) containing L-Glutamine (PAA, M11-004), Penicillin/Streptomycin (PAA, P11-010) and Fibronectin (Sigma). Rat Astrocytes (RA) and astrocyte culture medium (AM) were provided by Innoprot. Rabbit monoclonal to RP1 (Anti-LRP1 antibody) and Alexa Fluor® 488 Goat Anti-Rabbit antibody were purchased from AbCam and Invitrogen, respectively.

## Hemocompatibility test

Hemocompatibility of 15F and REG-functionalized-NPs loaded and not loaded with PTX was evaluated by diluting NPs in PBS at concentrations of 100 µg/ml. Hemocompatibility test was carried out after blood exposure (according to ISO 10993-4). Interaction of NPs with blood was analyzed during 15 minutes at 37ºC using normal human plasma collected under citrate. Firstly, microscopic pictures of the whole blood after NPs exposure were analyzed. Next, the hemolysis test was performed according to ASTM (Standard practice for assessment of haemolytic properties of materials, American Society for Testing and Materials Designation: ASTM: F 756-00) adopting Drabkin's method. According to ASTM, <2% is considered as non haemolytic; 2-5% slightly haemolytic and >5% haemolytic. Further experiments included blood cell counting (Cell-Dyn Emerald 18, Abbott) and quantification of complement activation by determining the C3a concentration (ELISA kit). Finally, analysis of the activation of the coagulation either by the intrinsic (TCA test) or the extrinsic (Quick) pathways was performed. Analysis of the coagulation through the intrinsic and extrinsic pathway was performed under standard conditions of operation in clinical biology, i.e. with the addition of kaolin and thromblastin, respectively as activator of this biological cascade. This methodology allows to verify if the factors associated with this cascade are adsorbed or denaturated by the NPs. A reduction of the % corresponds to an inactivation of this coagulation pathway.

## LRP-1 expression in targeted cells

LRP-1 expression was evaluated in U-87 MG and BBMVECs of the BBB by immunofluorescence techniques. U-87 MG and BBMVECs were seeded at a density of 2000 cells/cm$^2$ in a 24-well plates and incubated for 24 hours. Then the media was aspirate off, cells washed with PBS, fixed with 10% formalin for 20 minutes at RT and washed again for three times with PBS and permeabilized with 0.1% Triton X-100 in PBS for 10 minutes. Cells were then incubated with specific primary antibody (rabbit anti-LRP1, 1:200; Abcam, Cambridge, UK) in PBS/0.1% Triton X-100/1% bovine serum albumin (BSA)

overnight at 4º C. After washing cells six times with PBS/0.1% Triton X-100 incubation with specific secondary antibody (Alexa Fluor 488 goat anti-rabbit, 1:300; Invitrogen, Carlsbad, CA) for 1 hour at RT was carried out. After last cell washing with PBS solution, cell nuclei were counterstained with Vectashield commercial mounting medium containing DAPI. LRP1-1 expression in immunostained cells was observed with a ZEISS Axiovert 200M microscope. Images were taken with a Zeiss Axiocan MRm. In a qualitative experiment, the abilities of cellular internalization and the interaction of peptide-functionalized-NPs with LRP-1 were visualized under a fluorescent microscope, using fluorescently labeled peptides as the fluorescent probe.

## In vitro cellular uptake of peptide functionalized-PTX-NPs

PTX loaded and peptide-functionalized NPs uptake by BBB endothelial cells and glioma cells was analyzed. BBMECs and U-87 MG cells were seeded at 20000 cells/$cm^2$ density in 24-well plate and incubated for 24 hours at 37ºC and 5% of $CO_2$. After checking the confluence and the morphology, cell culture media was removed, cells were washed three times with PBS and treated with NPs solution at a concentration of 250 µg/ml (DMEM without FBS) for 30 minutes at 4ºC and 37ºC. After the incubation, cells were washed three times with PBS, fixed with 10% formalin solution for 20 minutes, cell nuclei counterstained with DAPI and examined under a fluorescence microscope (ZEISS Axiovert 200M). Images were taken with a ZEISS Axiocam MRm. In a separate experiment, to study LRP-1 expression concurrently with cellular uptake, U-87 MG cells were incubated for 30 minutes in the presence of peptide-functionalized-NPs at 37ºC for 4 hours. The cultures were then fixed, immunostained for LRP-1 as described above, and then subjected to fluorescent microscopy analysis.

## NPs toxicity study on glioma, neuroblastoma, endothelial cells and glia

### ❖ MTS on glioma cell line (U-87 MG)

In order to evaluate the cytotoxicity of the REG-PTX-NPs on glioma cell line (U-87 MG), the cells were grown in DMEM supplemented with 10% FBS, 1% L-Glutamine and 1% Penicillin/Streptomycin and plated in 96-well plates at a cellular density of 30.000 cells/ml. After 24 h, medium was aspirated and substituted with 100 µl at 20 nM PTX concentration of PTX-NPs and REG-PTX-NPs suspensions. Empty NPs were also examined with the concentration corresponding to that of 10 nM of PTX. Cells with PTX at 20 nM were used as positive control; cells without NPs were used as the negative control. After 1, 4, 6 and 8 days, cell viability was assessed via MTS assay following the manufacturer instructions. Briefly, cells are washed with PBS and incubated with a solution of the MTS reagent and complete media at 37ºC. The absorption (A), which represented cell viability was measured via a microplate reader (Spectramax M2$^{e}$) at the wavelength of 490 nm. Cell viability was calculated by Equation 3.4 and the errors bars were obtained from triplicate samples

$$\text{Cell viability } (\%) = \frac{\text{A}_{sample} - A_{blank}}{\text{A}_{control} - A_{blank}} \times 100$$

Equation 3.4

### ❖ MTT on BBMVECs, human neuroblastoma cell line (IMR-32) and rat glial cells

The cells were plated in 96-well plates and after that the medium was aspirated, NPs, 15F-NPs and REG-NPs solutions were added. Cells without NPs were used as negative control; cells without NPs and treated with sds were used as the positive control. After 24 hours cell viability was assessed via MTT following the manufacturer instructions. Briefly, cells are washed with PBS and incubated with a solution of the MTT reagent and complete media at 37ºC for two hours. The absorption (A), which represented cell viability was

measured via a microplate reader (Spectramax M2e) at the wavelength of 540 nm. Cell viability was calculated as before described by the Equation 3.4 .

.

### ❖ Generation of reactive oxygen species (ROS) test on BBMVECs, human neuroblastoma cell line (IMR-32) and rat glial cells

Generation of reactive oxygen species (ROS) is inevitable for healthy cells and occurs at a controlled rate. Under conditions of oxidative stress (e.g. toxicity), ROS production is dramatically increased, resulting in subsequent alteration of membrane lipids, proteins, and nucleic acids. Different cell lines seeded on 24 well/plates were exposed to the NPs solutions (NPS, 15F-NPs and REG-NPs) at a concentration of 0.25 and 0.5 mg/ml. After incubating cells at 37° C for 24 h, cells were washed with PBS and incubated with a PBS solution of the Dichloro-dihydro-fluorescein diacetate (DCFH-DA) reagent (5 µM) at 37ºC for half hour. When DCFH (commonly known as dichlorofluorescin) enters the cells, cleavage of the diacetate groups following enzymatic or base-catalyzed occurs and a rapid oxidation to the highly fluorescent product dichlorofluorescein (DHF) takes place. The fluorescence was then analysed by flow cytometry. Cells without NPs were used as negative control; cells without NPs and treated with doxorubicin were used as positive control. The results were expressed as mean ± standard deviation (mean ± S.D) for three replicate samples (n=6).

### ❖ Annexin A5 affinity assay on BBMVECs, human neuroblastoma cell line (IMR-32) and rat glial cells

Apoptosis is a carefully regulated process of cell death that occurs as a normal part of development. In normal live cells, phosphatidylserine (PS) is located on the cytoplasmic surface of the cell membrane. However, in apoptotic cells, PS is translocated from the inner to the outer leaflet of the plasma membrane, thus exposing PS to the external

cellular environment. The human anticoagulant, annexin V, has a high affinity for PS. Annexin V labelled with a fluorophore (Alexa Fluor® 488) can identify apoptotic cells providing an assay for apoptosis. Different cell lines seeded on 24 well/plates were exposed to the NPs solutions (NPS, 15F-NPs and REG-NPs) at concentration of 0.25 and 0.5 mg/ml. After incubating cells at 37° C for 24 h, cells were washed with PBS and incubated with a water solution of annexin V (10 mM HEPES, 140 mM NaCl, 2,5 mM Cacl2, pH 7.4) at 5 µL annexin V for 100 µL cellular suspension and at RT for half hour. Finally, cells were washed with PBS and 1 µL of propidium iodide (PI) in annexin solution was added before flow cytometry. Cells without NPs were used as negative control; cells without NPs and treated with doxorubicin were used as positive control. The results were expressed as mean ± standard deviation (mean ± S.D) for three replicate samples (n=6).

## Transendothelial transport experiments by NTA and UPLC

To provide an *in vitro* model of BBB for studying brain capillary functions, a system of co-culture that closely mimics the *in vivo* BBB was developed. The endothelial cells were seeded onto polycarbonate filters (Transwell insert), that were placed in the wells containing astrocytes (no-contact). Primary culture of fresh astrocytes were plated in AM-a culture medium and when confluence reached 80-90%, astrocytes were seeded in a 6-wells plate (125.000 cells/well, 2ml). When the cellular confluence reached 60-70%, bovine Brain endothelial cells were seeded in Transwell insert (1 µm pore for a six well plate, 150000-200000 cells per insert) after coating surface. The co-culture was established after 48-72 hours aspirating astrocytes medium and transferring the Transwell insert into the wells so as to obtain a luminal and abluminal compartment. In order to assess the barrier integrity, BBB models were characterized in terms of trans-endothelial electrical resistance (TEER measurement after 72 h from the co-culture establishment, each measure per triplicate) and permeability (Pe) of the water-soluble molecular tracer Lucifer Yellow (LY). Transport from the luminal to abluminal compartment was performed as follows. PTX loaded REG-targeted and non-targeted NPs were suspended in Ringer's solution at concentration of 250 µg/ml. 1.5 ml of NPs solution were incubated in the

luminal compartment of the BBB for 60 minutes at 37ºC and with 5% of $CO_2$. 2.5 ml of Ringer's solution was add in the abluminal compartment. Samples were collected from both compartments, at the beginning and at the end of the experiments and NPs concentrations were measured by NTA and by UPLC with the experimental conditions described in drug encapsulation efficiency section. An insert without cells was used as blank.

## Transendothelial transport experiments by fluorimetry

In a separate transendothelial transport experiment, performed at Centro Tecnologico GAIKER-IK4, Zamudio, Spain, two *in vitro* BBB models employing endothelial and bend3 cells, respectively, were developed. A system of co-culture was established and 3P-fluorescently-labeled NPs, 15F-NPs and REG-NPs suspended in RHB + 0.5% BSA medium at 0.25 and 0.5 mg/ml concentrations, were incubated in the luminal compartment of the BBB model for 60 minutes. Moreover, in order to verify that NPs do not affect the barrier integrity, the permeability of the water-soluble molecular tracer Lucifer Yellow (LY) was studied. The permeability of NPs and LY through endothelial cells monolayer was determined

## 3.3 Results and Discussion

### 3.3.1 Synthesis and Characterization of Block Co-polymer (2P)

Block co-polymer 2P was synthetized by polycondensation of the linker (2,2'-dithiodipyridine and α-Thio-ω-carboxy poly-ethylene glycol) coupled to peptide by disulfide bonds, and pre-polymer P* (1.8-octanediol and glutaric acid, 1.2:1 molar) in a microwave reactor, under vacuum, at 120°C and 100 W and with a ratio 1:1 (w/w) between preformed peptide-targeted linker and pre-polymer P* (Scheme 3.2).

The composition of linker, P* and 2P co-polymers is confirmed by $^{1}$H-NMR. The linker polymer structure is confirmed by the corresponding $^{1}$H-NMR spectra (Figure 3.1). The four typical signals of the pyridyl group are shown at the aromatic region between 6.5 ppm and 8.0 ppm (peaks a to d). The other proton signals refer to the different methylene groups present in the polymer structure. N-methylene protons of the amide group appear at 3.81 ppm as a multiplet (peak e) deshield due to the electronegativity of the near nitrogen. The signal corresponding to the PEG 1500 is shown as an intense singlet at 3.64 ppm as expected (peak f), with an integration number of 369H referred to the protons of the pyridyl group. Methylene groups directly attached to the PEG group are evidenced at 3.46 ppm (peak g) and 3.37 ppm (peak h) both as multiplets, at the amide group and carboxylic group sides, respectively. Protons on the β-carbon of the carboxylic acid appear as different signals as they are not magnetically equivalent, at 3.07 ppm and 2.96 ppm (peak i). Signals at 2.63 ppm and 2.37 ppm correspond to the protons on the α-carbon of the amide (peak j) and carboxylic acid (peak k), respectively. Finally, the most upfield protons appear at 1.86 ppm as a multiplet (peak l). *$^{1}$H NMR (400 MHz, Methanol-d$_4$) δ 8.42 (td, J = 4.7, 2.4 Hz, 1H, a), 7.88 – 7.78 (m, 1H, b), 7.77 – 7.66 (m, 1H, c), 7.28 – 7.21 (m, 1H, d), 3.81 (m, 2H, e), 3,64 (s, 369H, f) 3.46 (m, 2H, g), 3.37 (td, J = 5.5, 2.5 Hz, 2H, h), 3.07 (t, J = 7.1 Hz, 1H, i), 2.96 (t, J = 7.2 Hz, 1H, i), 2.63 (td, J = 7.2, 6.4 Hz, 2H, j), 2.37 (t, J = 7.4 Hz, 2H, k), 1.86 (m, 2H, l).*

The P* structure is confirmed by the corresponding $^{1}$H-NMR spectra (Figure 3.2). Signals corresponding to the protons of the methylene groups attached to heteroatom are

observed at 4.08 ppm and 3.54 ppm, connected to the ester group (peak a) and to the hydroxyl group (peak b), respectively. Protons on the α-carbon of carboxylic acid and ester groups appear as a complex multiplet at 2.38 ppm (peak c), while the protons of the carbon atom on β-carbonyl appear as a multiplet at 1.90 ppm (peak d). The methylenic groups of the hydroxyl chain non-directly connected to heteroatom appear at 1.64 ppm (peak e) and 1.53 ppm (peak f), which corresponds to the most external groups, and at 1.36 ppm (peak g) as an intense signal, which corresponds to the central methylenic groups. *$^1$H NMR (400 MHz, Methanol-$d_4$) δ 4.08 (t, a), 3.54 (t, b), 2.38 (m, c), 1.90 (m, d), 1.64 (m, e), 1.53 (m, f), 1.36 (m, g).*

As the corresponding $^1$H-NMR reveals (Figure 3.3), the aromatic signals of the pyridyl group are not observed in the spectra of the 2P polymer. The signals corresponding to P* polymer are present in the spectra, and the peak corresponding to the protons of the methylene adjacent to the terminal alcohol has disappeared, as expected, due to bond formation with linker. Moreover, presence of PEG in the polymer is confirmed by the appearance of a peak at 3.50 ppm. *$^1$H NMR (400 MHz, DMSO-$d_6$) δ 3.99 (t), 3.50 (s), 2.31 (t), 2.23 (t), 1.73 (m), 1.54 (m), 1.39 (m), 1.26 (s).*

The weight-averaged molecular weight and molecular weight distribution of the obtained P* and REG-2P co-polymer were determined by means of GPC. The molecular weights were found to be 1069 and 10299 for the P* and REG-2P copolymers, respectively. The PDI was narrow, which was around 1.8 for the P* co-polymer and 1.4 for the REG-2P co-polymer. To verify the correct assignment of the peak fractions, the average molecular weight determination of the fractions was performed by MALDI-TOF mass spectroscopy. All mass spectra showed one major peak in agreement with the GPC profiles. The obtained experimental molecular weights were approximately 1000, 3000, 7300, 10200 for P* (Figure 3.4), linker (Figure 3.5), 15F-2P (Figure 3.6) and REG-2P (Figure 3.7), respectively.

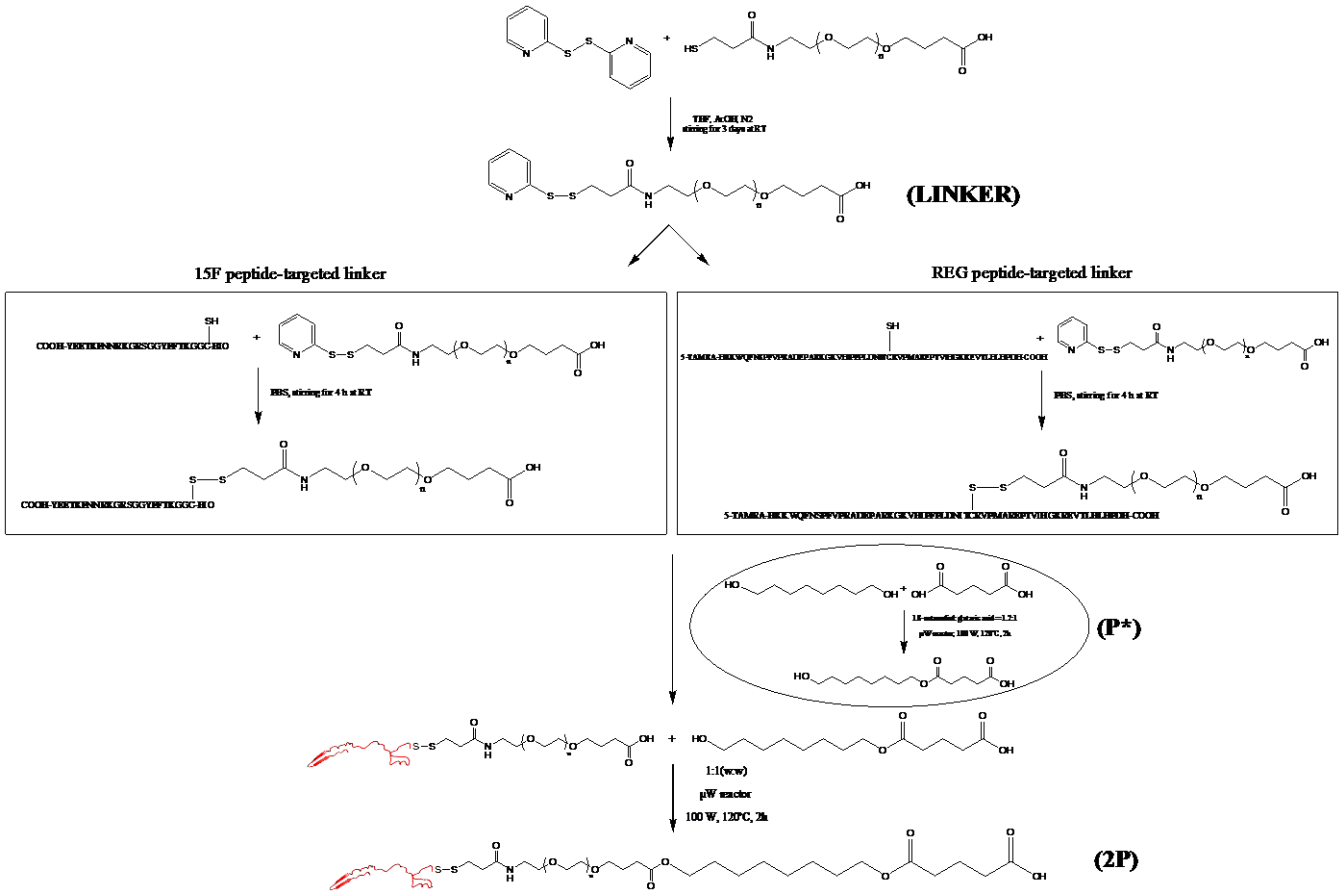


Scheme 3.2 Synthesis by polycondensation of block co-polymer 2P

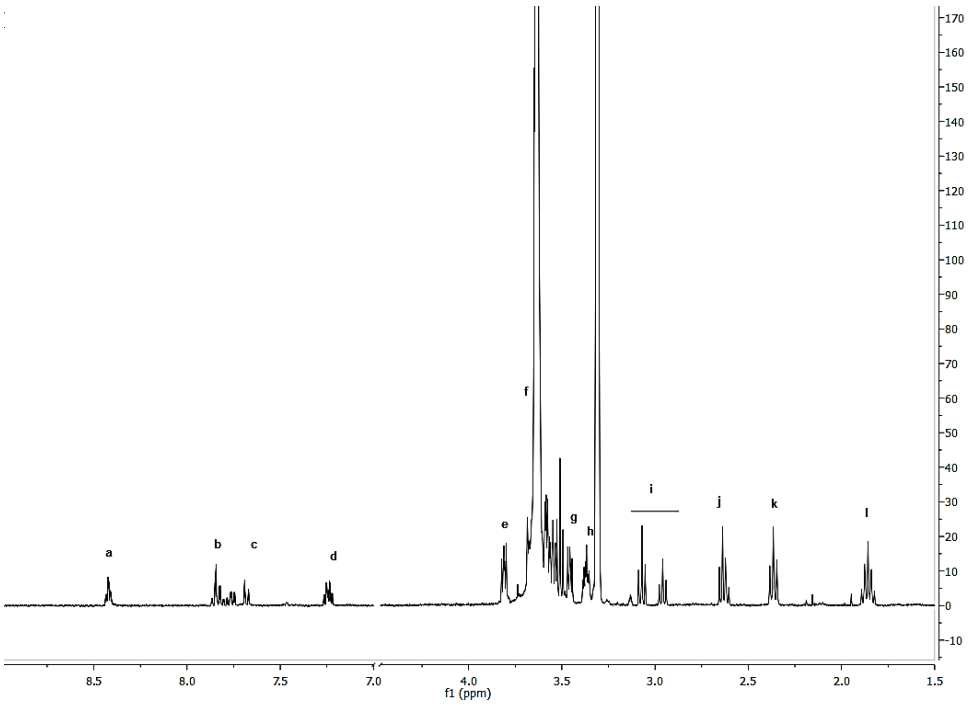


Figure 3.1 $^{1}$H-NMR spectra of Linker

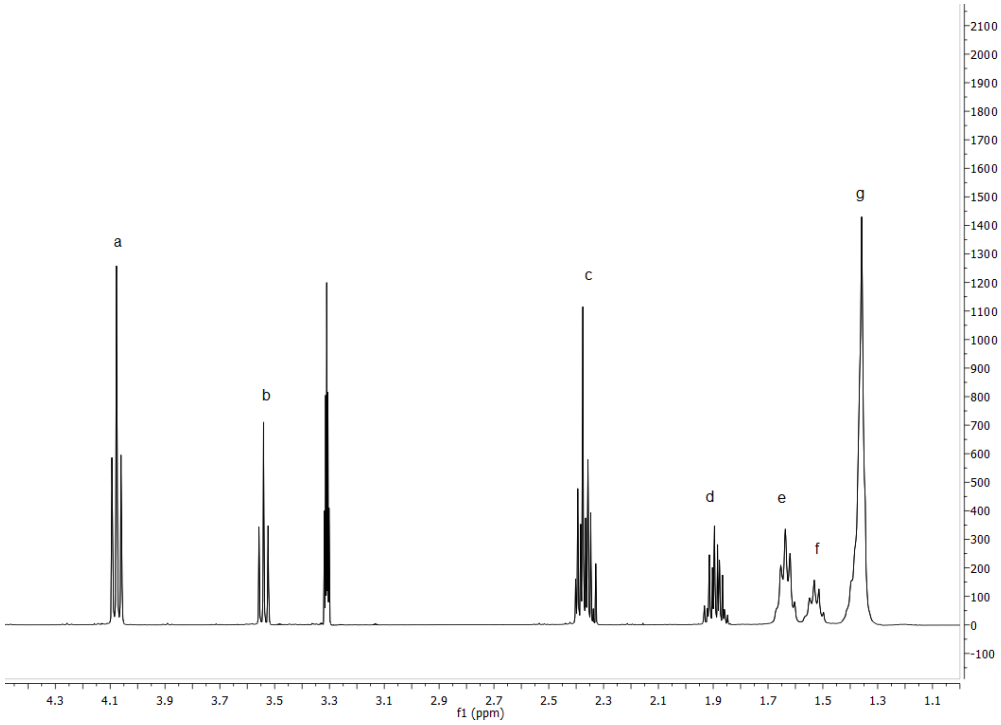


Figure 3.2 $^{1}$H-NMR spectra of P* block co-polymer

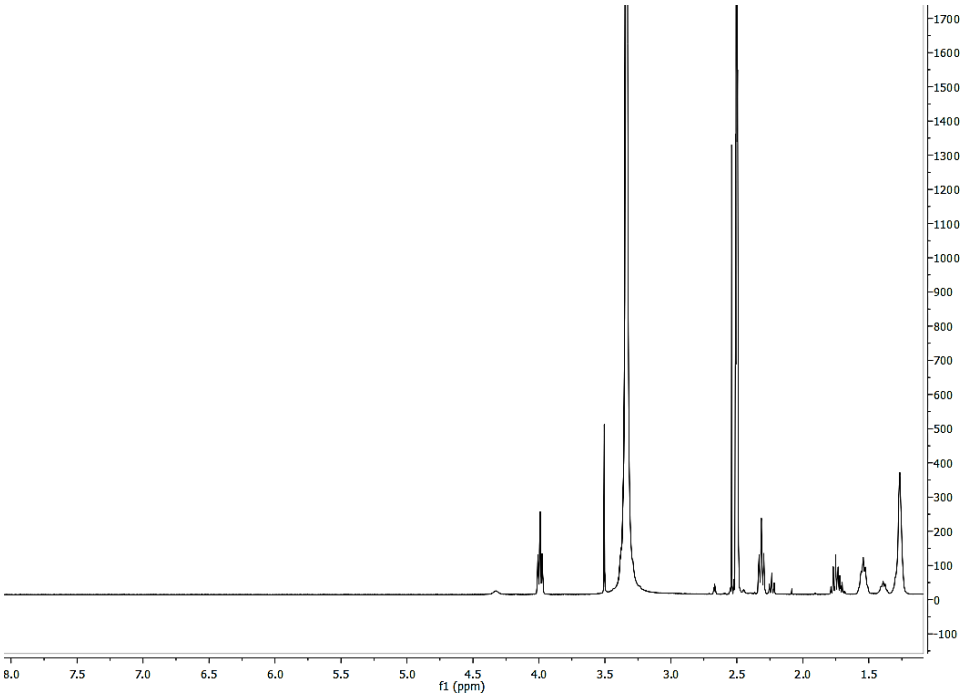


Figure 3.3 1H-NMR spectra of 2P block co-polymer

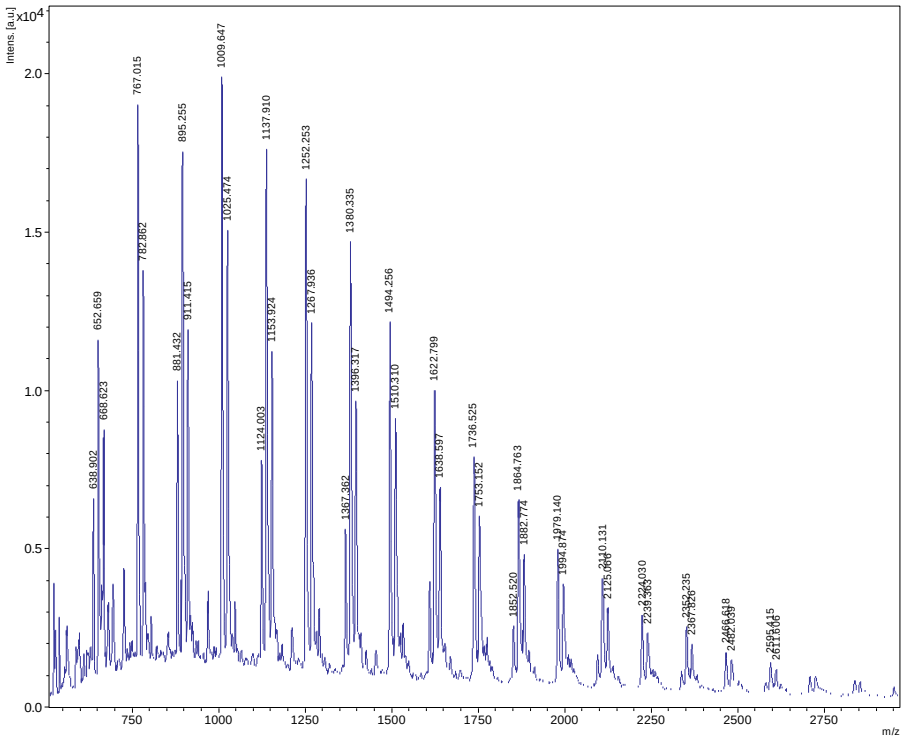


Figure 3.4 MALDI-TOF mass spectroscopy of P* block co-polymer

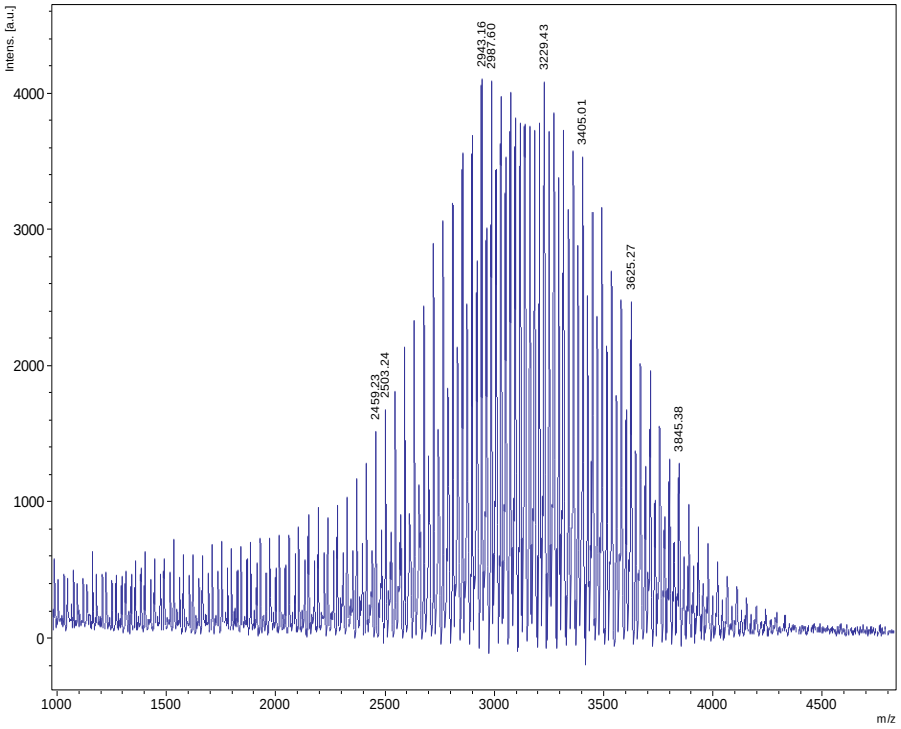


Figure 3.5 MALDI-TOF mass spectroscopy of linker

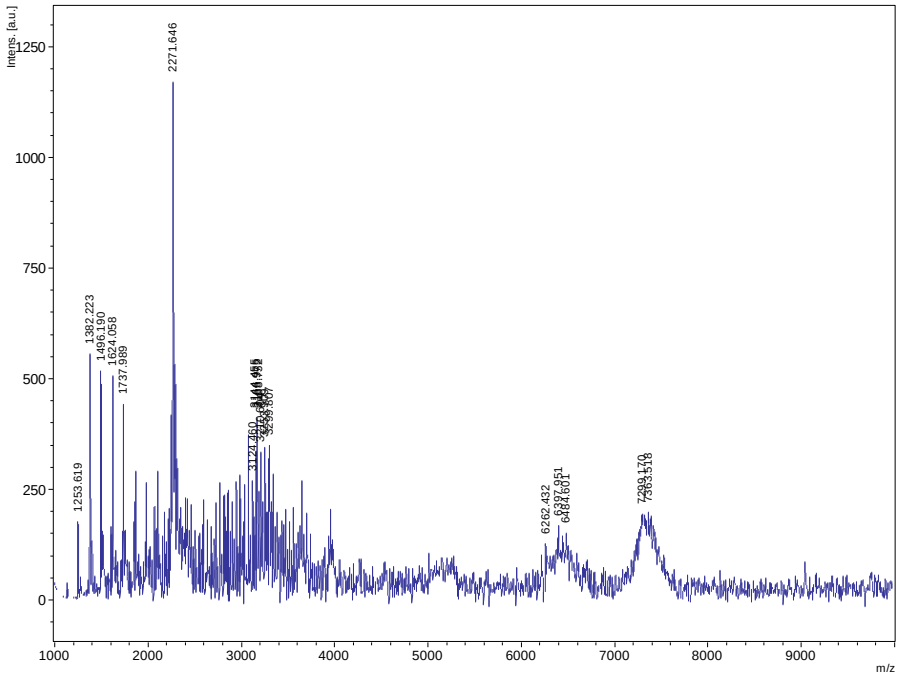


Figure 3.6 MALDI-TOF mass spectroscopy of 15F-2P block co-polymer

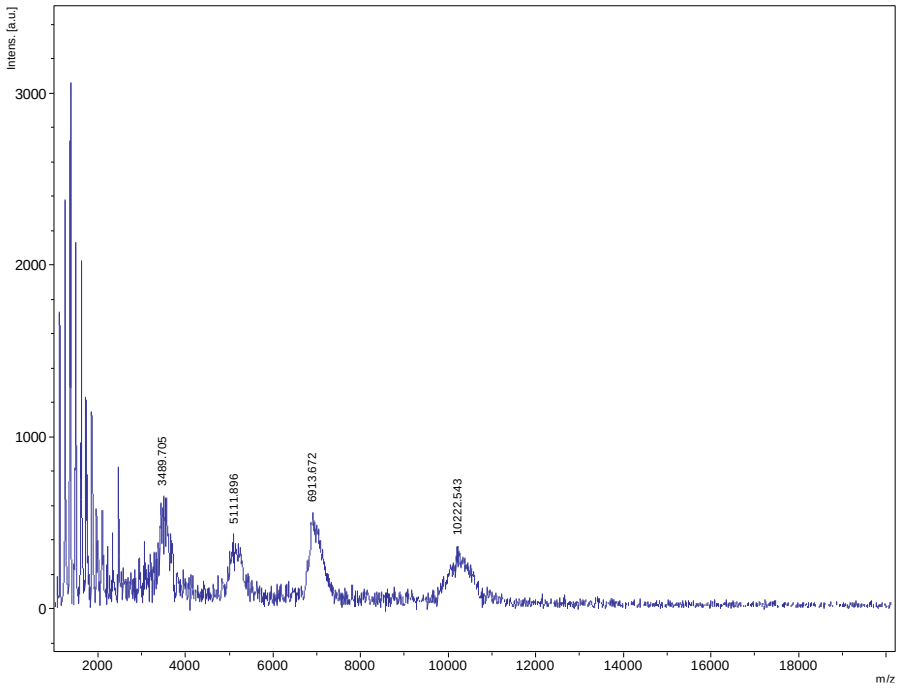


Figure 3.7 MALDI-TOF mass spectroscopy of 15F-REG block co-polymer

### 3.3.2 Characterization of 15F and REG-functionalized-PTX-NPs

#### Morphology, particle size, size distribution and zeta-potential

The modified nanoprecipitation approach proposed for the preparation of peptide-functionalized PTX-NPs is shown in the schematic illustration of Scheme 3.3. In this process, the organic phase containing preformed block co-polymers P and 2P was co-precipitated with PTX into the aqueous phase to form NPs. The particle size, polydispersity and morphology are shown in Figure 3.8. The average diameter of NPs determined by DLS and NTA was 180 nm with a PDI of 0.1 (Figure 3.8 A, B, D). The zeta potential for both peptide functionalized-PTX-NPs was about -32±1.5 mV. TEM images (Figure 3.8 C) revealed that the NPs were dispersed as individual NP with a well-defined spherical shape surrounded by PEG-corona and homogenous distribution around 200 nm in diameter, without any adhesion or aggregation.

## Drug efficiency and Differential Scanning Calorimetry (DSC)

As described by the previous Chapter with PTX-NPs (without 2P block co-polymer), an increase in PTX theoretical loading led to a corresponding increase in D.C. (% w/w) with E.E. (%) remaining approximately constant. The D.C. of peptide-functionalized-PTX-NPs was confirmed about 4 % and 7 % when the PTX theoretical loading was 3 and 5%, respectively. Higher D.C. than other polyester-based NPs [32] is most likely due to the arrangement of the hydrophobic P and 2P co-polymers regions when forming NPs. Indeed, PTX acting as binding agent facilitates nanoprecipitation probably by increasing lipophilic interaction among hydrophobic co-polymers blocks. Supposedly, polyester regions of the P and 2P co-polymers are in close contact with PTX while PEG groups are directed to NPs surface to interact with water. DSC showed the existence of the PTX, formulated in the peptide-functionalized-PTX-NPs at 3 and 5% PTX theoretical loading, in an amorphous state or solid solution in the polymeric matrix.

## *In vitro* PTX release

The release profile of PTX from 3 % PTX loaded peptide-functionalized-NPs in PBS 0.1 M with 0.3 % v/v Tween-80, at 37ºC is presented in Figure 3.9. The release pattern displayed an approximately first-order release, without initial burst and with a drug release reaching completion in approximately 12-13 days. The release was very slow and constant with approximately 19 % of PTX released in 24 hours. The initial burst absence and the nearly linear behavior demonstrate the absence of adsorbed drug on NPs surface. *In vitro* PTX release from polyester-based NPs usually present biphasic profile or very fast complete drug release. PHA (Poly Hydroxyalkanotes) and poly ε-CPL for example, released over 50% of PTX in the first hours [22,32]. On the other hand PDLLA/PLGA PEG NPs exhibited a lower burst effect, but nevertheless the total cargo is released in 2 and 4 days, respectively [32,33], which, generally, is too fast to meet therapeutic needs. As discussed in the previous Chapter with PTX-NPs, when higher drug loading (e.g. 10, 15%) same trend but a slower release was achieved. The higher PTX content (w/w) in the polymeric matrix bestow on NPs greater hydrophobic character, leading to slower release that is proportional to NPs

co-polymer matrix degradation and depending on the total cargo, allows PTX to be released in a modulated and controlled way. This may be explained assuming that PTX acts as a binding agent, thus higher PTX weight content in the matrix material makes the NPs possess greater hydrophobic character, leading to limited water entry into the NPs core.

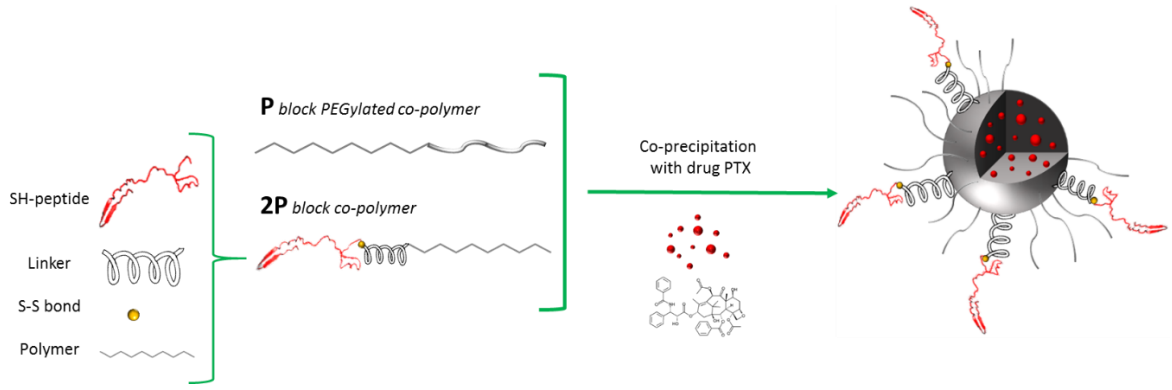


Scheme 3.3 Fabrication of peptide-functionalized-NPs encapsulating PTX via co-precipitation

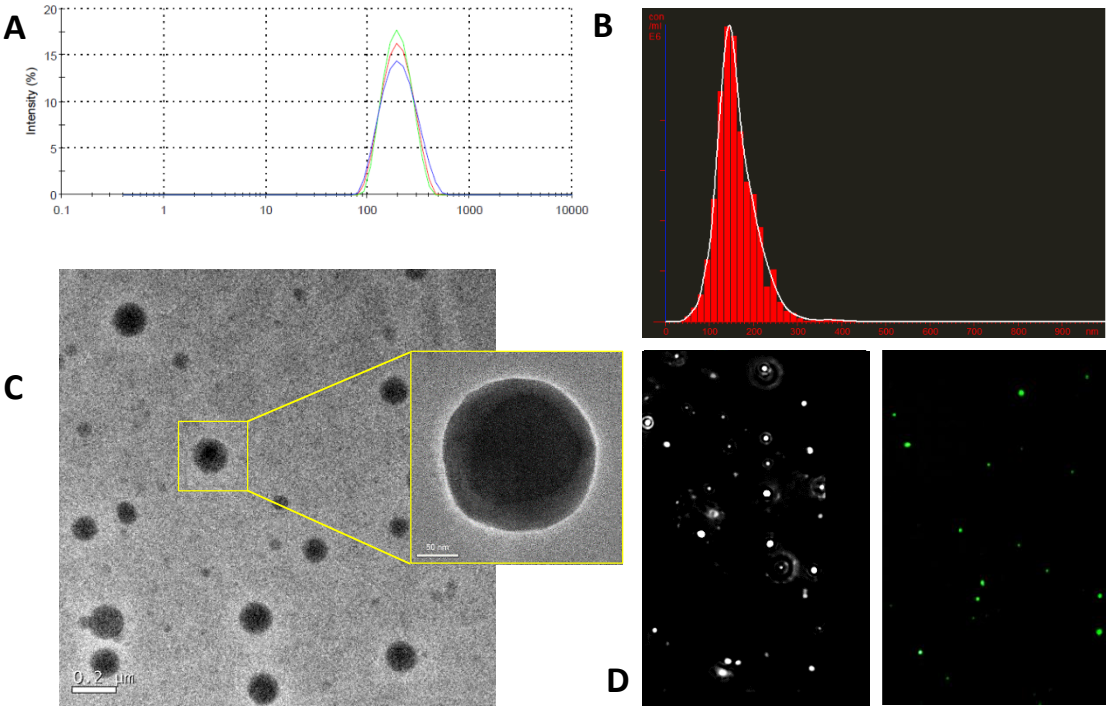


Figure 3.8 Characterization of peptide-functionalized-PTX-NPs. NPs size distribution determined by (A) DLS and (B) NTA; (C) TEM images of peptide-functionalized-PTX-NPs with different magnifications; (D) NTA sample video frame of NPs moving under Brownian motion in (left) scattering and (right) fluorescent mode

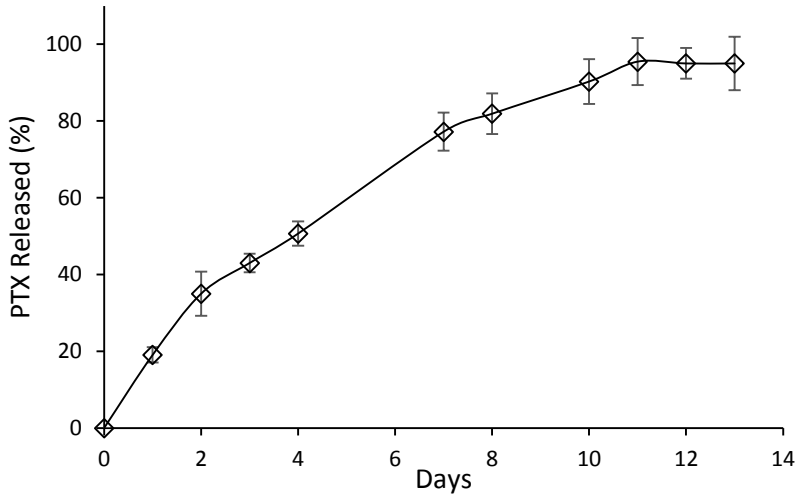


Figure 3.9 In vitro release kinetics of PTX from peptide-functionalized-PTX-NPs at 3 % w/w theoretical drug content (PBS 0.1 M with 0.3 % v/v Tween-80, pH 7.4, 37ºC) Mean ± SD (n=3)

## Peptide-conjugation efficiency

AGBBB015F (15F), introduced in 2007 by Demeule and co-workers [34], is a peptide that belongs to a family of peptides named Angiopeps , which were derived from the Kunitz domain of aprotinin. Angiopeps are known to be able to pass through the BBB with a mechanism involving the LDLR (low density lipoprotein receptor).

Regulon (REG) peptide is able to cross the BBB but its mechanism of action has not been reported yet and no relationship between Regulon and the LDLR has been published. It is made up of 59 AAs and the proposed structure, predicted with an ab-initio method [35–37], can be divided into two parts: (i) a long unstructured flexible chain, (ii) a rigid β-hairpin structure, localized near the C-terminal region. The β-hairpin is constituted of 2 beta-strands and a U-turn, localized in the TVIHG, EVTLH and KR regions, respectively. It is supposed that REG interacts with the LA domain of LDLR family using its hairpin region but this interaction is insufficient to justify the binding of the whole REG peptide. This hypothesis is based on the interacting surface area, which is rather small with respect to the total REG surface. Considering REG as a double domain binder, the flexible loop of REG should participate in the binding through the residues R13, R19 and K20, K22. Indeed, it

has a larger interacting surface and moreover, it has a residue composition and configuration that can resemble the flexible Kunitz domain of 15F peptide. In both domains the presence of arginine and lysine amino acids ensures the hydrogen bond interactions with the LRP1 receptor

Sulfhydryl groups are useful for peptide conjugation. First, sulfhydryls are not as numerous as primary amines; thus, crosslinking via sulfhydryl groups is more selective and precise. Second, sulfhydryl groups in proteins are often involved in disulfide bonds, so crosslinking at these sites typically does not significantly modify the underlying peptide structure. The coupling procedure between peptides and linker is suitable for incorporating relatively large peptide possessing Cys residue at the central region of the peptide, as described by G. Mezö et al [38]. The presence of Reg-peptide on the NPs surface was qualitatively validated by NTA under fluorescence mode Figure 3.8 D) and was confirmed by fluorometric assay, with a conjugation efficiency of 16.9 ± 2.1 and 15 ± 1.8 % for 15F and REG peptides respectively, and by amino acids quantification in REG-functionalized-NPs. Pro, Val and Phe were quantified at 33 ± 4.5, 16 ± 2 and 25 ± 5 % (w/w) of theoretical amino acid feeding, respectively.

### 3.3.3 Cell experiments

## Hemocompatibility test

Analyzing microscopic pictures of the whole blood after NPs exposure at 100ul/ml concentration, no change in morphology was observed on red blood cells (RBCs), white cell (WBCs) and platelets (Figure 3.10). 15F-NPs and 15F-PTX-NPs were not haemolytic. This was confirmed by cell counting analysis, which showed no significant changes in the number of RBCs, WBCs and platelets at these conditions. Furthermore, the lack of a significant activation of the complement system in the presence of the NPs suspension indicated no immunogenicity (Figure 3.11). Finally, no relevant activation of coagulation by the intrinsic or the extrinsic pathway was detected (Table 3.2)

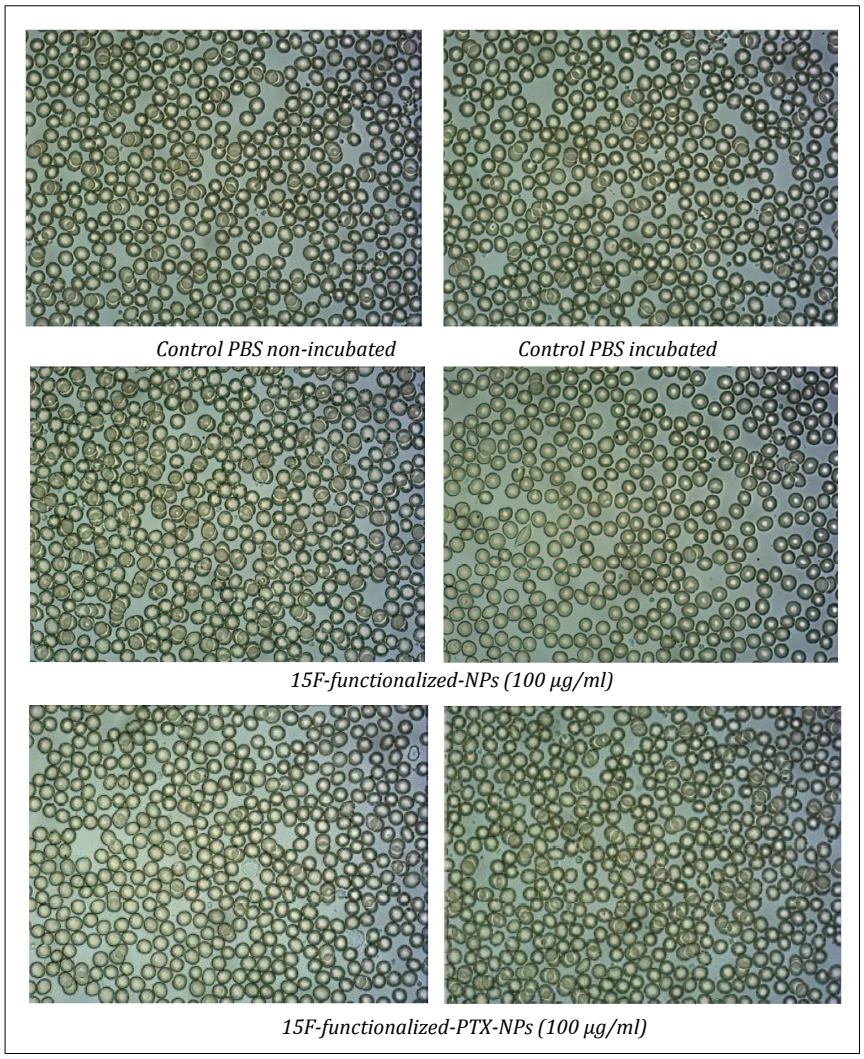


Figure 3.10 Microscopic pictures of the whole blood after 15F-PTX-NPs exposure

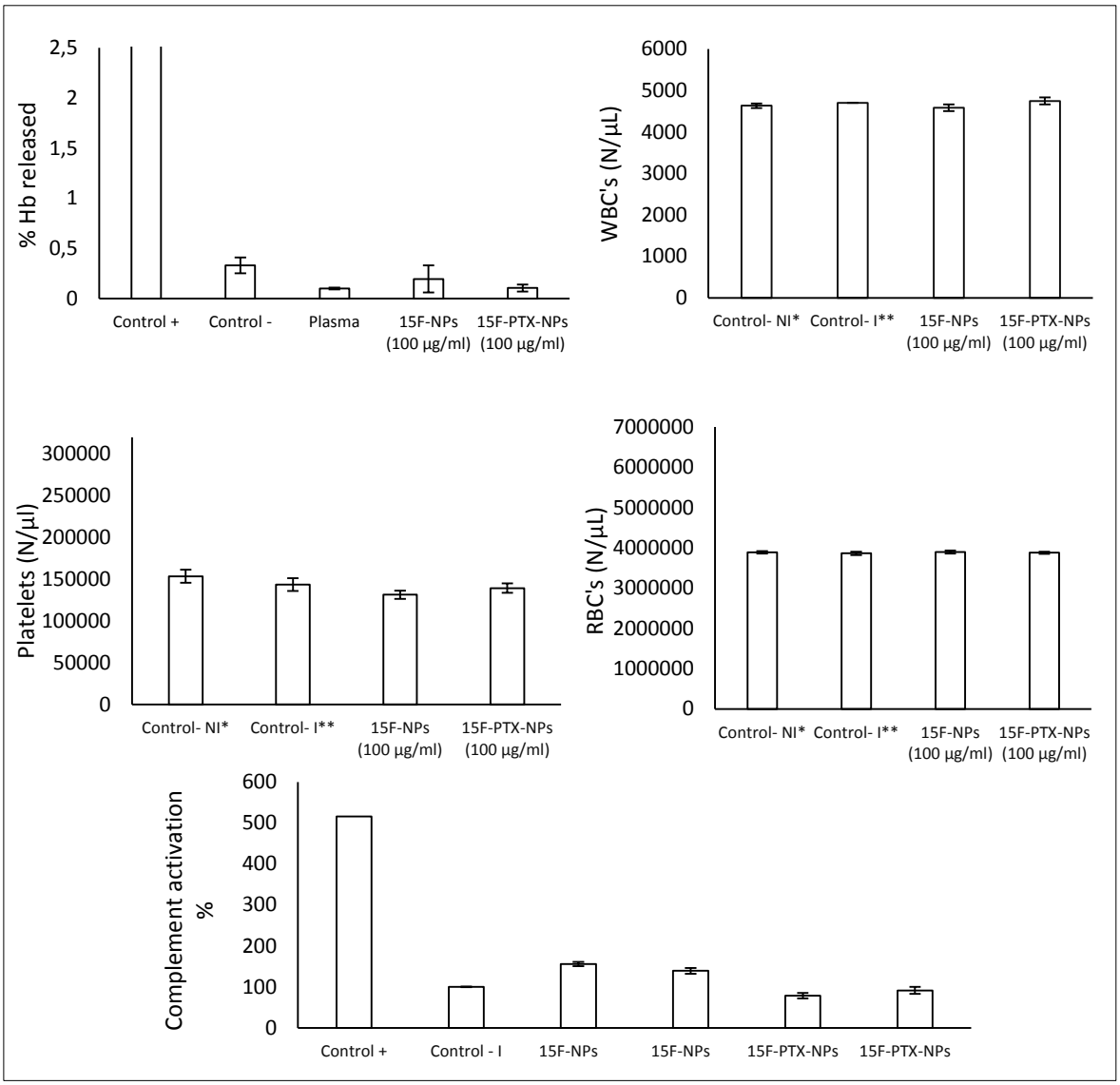


Figure 3.11 Hemolysis test, blood cell counting and complement activation study

Table 3.2 Hemostasis control

| Formulation | TCA or aPTT (%) | Quick or PT (%) |
|---|---|---|
| 15F-NPs (100 µg/ml) | >100 | 89,44 |
| 15F-PTX-NPs (100 µg/ml) | >100 | 91,87 |
| Positive control + Kaolin | 63,11 | 112,6 |
| Blood control incubated | 100 | 91,86 |
| Blood control non incubated | 100 | 90,24 |

## Receptor expression in targeted cells

Different transporters and receptors present at the BBB have been described as playing roles in maintaining the integrity of the BBB and brain homeostasis. Among them, the low-density lipoprotein receptor-related protein (LRP), whose presence had been proved extensively on brain capillary endothelial cells [39–41], possess the ability to mediate transport of ligands across endothelial cells of the BBB [13–15]. The low-density lipoprotein receptor-related protein-1 (LRP-1) is a membrane receptor displaying both scavenging and signaling functions. The wide variety of extracellular ligands and of cytoplasmic scaffolding and signaling proteins interacting with LRP-1 gives it a major role not only in physiological processes, such as embryogenesis and development, but also in critical pathological situations, including cancer and neurological disorders [42]. Qualitative analysis of LRP-1 expression was carried out by immunofluorescence on BBMVECs and U-87 MG cells with a specific antibody against LRP-1. The results showed high LRP-1 expression in BBMVECs and U-87 MG cells (Figure 3.12).

## Cellular uptake of peptide functionalized-NPs

In order to assess the ability of REG-functionalized-NPs to penetrate cells in an energy-dependent manner, fluorescently-labeled peptides-functionalized-NPs were incubated with BBMVECs and U-87 MG cells for 30 minutes at 4ºC and 37ºC and analyzed by fluorescent microscopy. As shown in Figure 3.13, while intracellular uptake of REG-functionalized-NP was observed at 37ºC in both BBMVECs and U-87 MG cultures, no cytoplasmic signal was detected when the incubation took place at 4ºC, suggesting that the intracellular transport of the NPs was energy-dependent. In order to confirm that this active transport was specifically mediated by the LRP-1 receptor, we studied the cellular uptake of REG-functionalized-NPs together with LRP-1 expression in U87 MG cells. After a 30 minutes incubation, a clear co-localization of LRP-1 receptor (in green) and REG-peptide-functionalized-NPs (in red) was detected inside the cytoplasm of U-87 MG cells (Figure 3.14). This result suggested again that the REG-peptide-functionalized-NPs internalization was being mediated by the LRP-1 receptor.

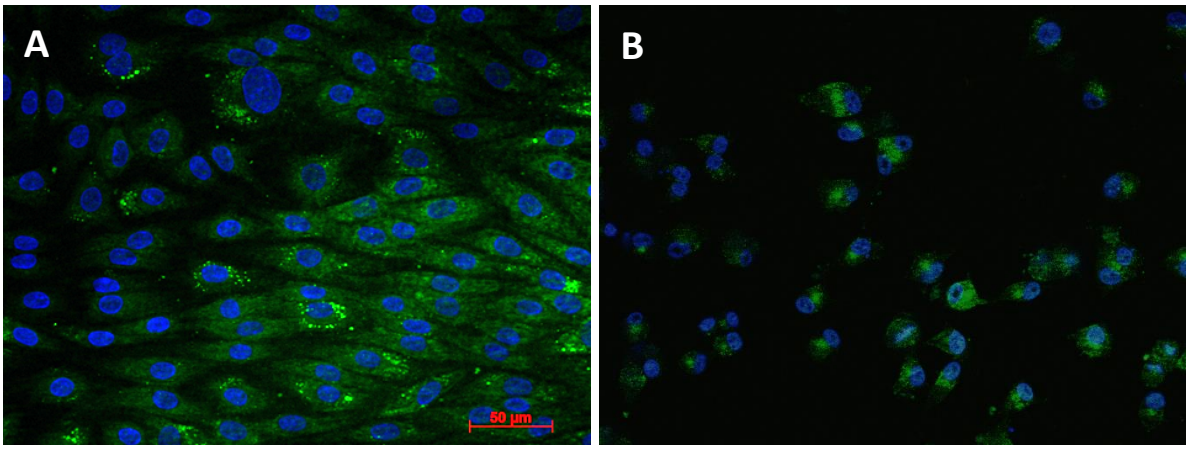


Figure 3.12 LRP-1 expression in (A) BBMVECs and (B) U-87 MG detected by a specific secondary antibody (Alexa Fluor 488 goat anti rabbit). Cell nuclei were counterstained with DAPI

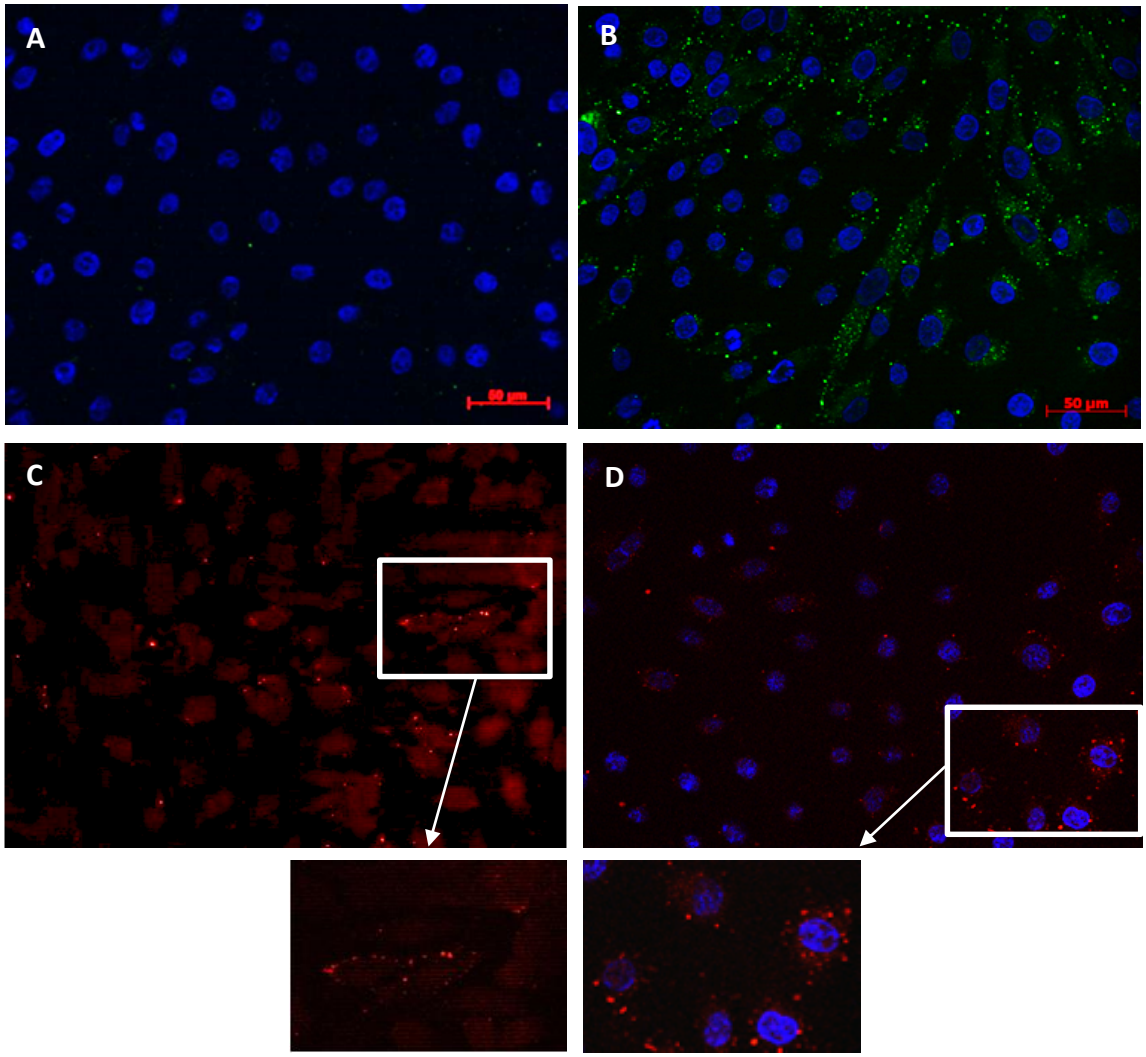


Figure 3.13 Cellular uptake of peptide functionalized NPs.BBMVECs incubated for 30 min in the presence of REG-functionalized-NPs at (A) 4 ºC and (B) 37ºC. U-87 MG incubated for 30 min in the presence of REG-functionalized-NPs at (C) 4ºC and (D) 37ºC. Cell nuclei counterstained with DAPI

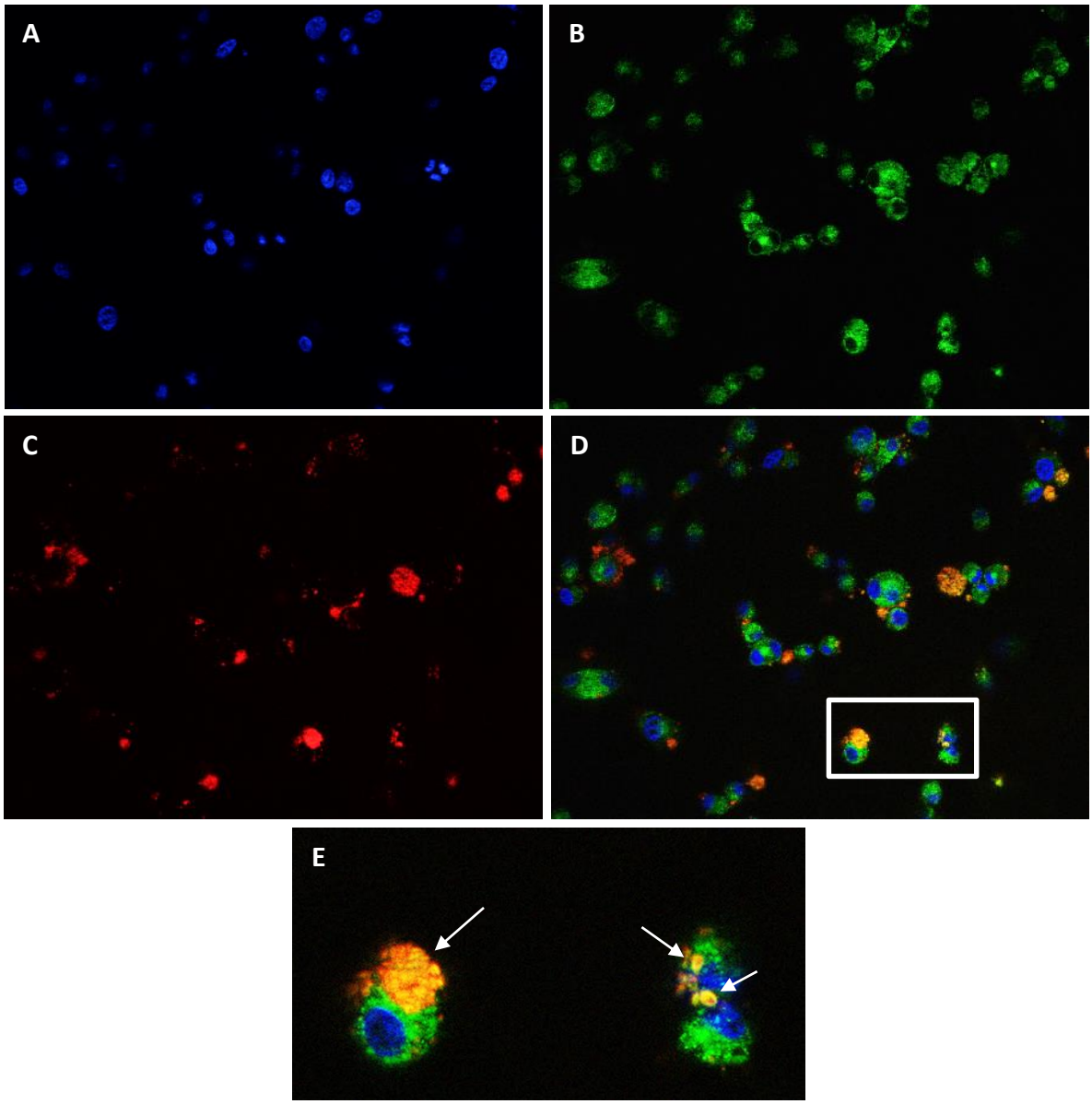


Figure 3.14 Intracellular uptake of REG-functionalized-NPs, 30 minutes transcytosis across the U-87 MG cells was performed for REG-NPs. (A) Cell nuclei counterstained with DAPI. (B) LRP1 in U-87 MG cells was labeled in green using a primary antibody (rabbit anti-LRP1) and secundary antibody (Alexa Fluor 488 goat anti-rabbit). (C) Incorporated REG-peptide-functionalized-NPs (in red) detected in vesicular structure of the U-87 MG cells. (D) Co-localization of REG-NPs (red) and LRP1 (green) is represented in orange in the merged image. (E) Image in the white square was enlarged and co-localization of REG-NPs with LRP1 (in orange) is indicated by arrow.

## NPs toxicity study on different cell lines

### ❖ MTS on glioma cell line (U-87 MG)

The *in vitro* anti-proliferative effect of REG-PTX-NPs, PTX-NPs, REG-NPs (without PTX) and free PTX on U-87 MG cells was evaluated using MTS assay. The synthetized block co-polymers (P, 2P) biocompatibility was confirmed since the drug-free REG-NPs showed no decrease in cellular viability and the REG peptide linked on the particle surface did not cause obvious cytotoxicity to U-87 MG cells. Cells were incubated with REG-(3%)-PTX-NPs and (3%)-PTX-NPs at 20 nM PTX concentrations. This concentration was selected because it corresponds to $IC_{50}$ value for U87-MG cells. As can be seen in Figure 3.15, a marked reduction in survival rate (down to 45%) was observed when U-87 MG cells were incubated for 8 days with REG-(3%)-PTX-NPs at 20 nM. After the same incubation time, PTX showed similar toxicity levels, indicating that the developed REG-PTX-NPs system did not decrease the PTX antitumoral activity and that the cytotoxicity against U-87 MG cells was in time-dependent manner. Otherwise, for (3%) PTX-NPs a slighter effect was observed, with 60 % survival rate showing that the antiproliferative effect of the PTX-NPs was markedly elevated by functionalizing with REG peptide. This result suggested that the enhanced toxicity in U-87 MG cells might be due to the active cellular uptake mediated by LRP1 interaction which increased the intracellular concentration of PTX.

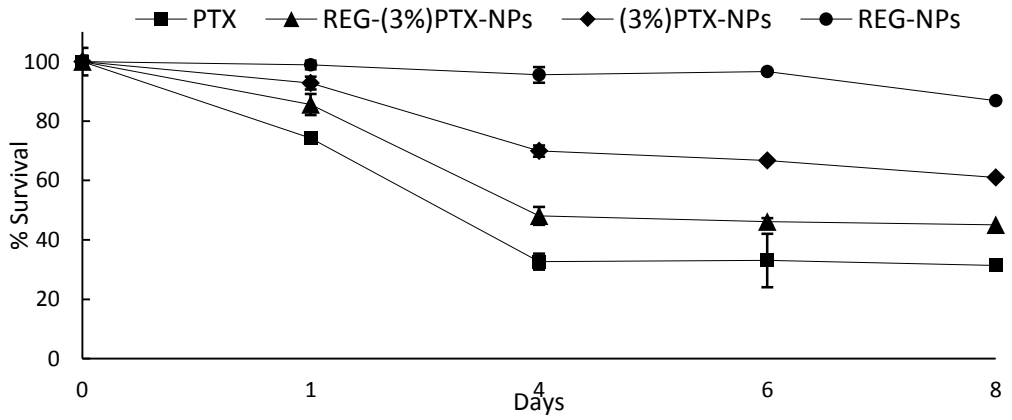


Figure 3.15 Cell viability on U-87 MG incubated with PTX, REG-(3%)PTX-NPs, (3%)PTX-NPs and REG-NPs (drug free) at 20 nM PTX concentration after 8 days cell culture (n=3)

## ❖ MTT on BBMVECs, human neuroblastoma cell line and rat glial cells

The *in vitro* toxicity of NPs, 15F-NPs and REG-NPs on BBMVECs, human neuroblastoma cell line and rat glial cells was evaluated by using MTS assay. In Table 3.3 are shown the values of $IC_{20}$, $IC_{50}$ and $IC_{80}$ which represents the concentrations for each formulation of NPs needed to inhibit 20, 50 and 80 % the cellular viability, respectively. Since pronounced lower concentrations inhibition of all NPs formulations in respect to SDS, it can be assessed that NPs at concentration tested did not cause obvious cytotoxicity to all cell lines tested.

Table 3.3 NPs, 15F-NPs and REG-NPs Inhibitory concentration (20, 50 and 80 %) on Astrocytes, BBMVECs and IMR-32 cells

| **Astrocytes** | **NPs** | **Reg-NPs** | **15F-NPs** | **SDS** |
|---|---|---|---|---|
| **IC20** | 900,1482 µg/mL | 500,392 µg/mL | 1345,63 µg/mL | 103,97078 µg/mL |
| **IC50** | 5621,65 µg/mL | 2091,47 µg/mL | 2924,93 µg/mL | 133,058 µg/mL |
| **IC80** | 1,10E+08 µg/mL | 8741,62 µg/mL | 6357,76 µg/mL | 170,311333 µg/mL |

| **BBMVECs** | **NPs** | **Reg-NPs** | **15F-NPs** | **SDS** |
|---|---|---|---|---|
| **IC20** | 486,013 µg/mL | 409,897 µg/mL | 215,817 µg/mL | 228,530488 µg/mL |
| **IC50** | 2211,2 µg/mL | 1710439 µg/mL | 1988,97 µg/mL | 282,165667 µg/mL |
| **IC80** | 13682,5 µg/mL | 7,10E+09 µg/mL | 18330,3 µg/mL | 348,548333 µg/mL |

| **IMR-32** | **NPs** | **Reg-NPs** | **15F-NPs** | **SDS** |
|---|---|---|---|---|
| **IC20** | 706,689 µg/mL | 495,317 µg/mL | 671,587 µg/mL | 49,3800434 µg/mL |
| **IC50** | 1244,77 µg/mL | 1036,50 µg/mL | 1137,77 µg/mL | 84,9392667 µg/mL |
| **IC80** | 2213,71 µg/mL | 1770,65 µg/mL | 1927,57 µg/mL | 165,0313 µg/mL |

## ❖ ROS test on BBMVECs, human neuroblastoma cell line and rat glial cells

The Generation of reactive oxygen species (ROS) *in vitro* was evaluated employing the fluorescent probe DCFH-DA that once into the cells, following enzymatic or base-catalyzed cleavage of the diacetate groups, it is readily oxidized to the highly fluorescent product dichlorofluorescein (DCF) and analyzed by flow cytometry. As shown in Figure 3.16 no significant differences in generation of ROS, compared with negative control (glial cells: 12,11 ± 2,93%; BBMVECs: 16,94 ± 1,24 %; IMR32: 18,86 ± 5,57 %), were detected for the three NPs formulations at tested concentration. Otherwise a pronounced and statistically significant ($p<0.005$) percentage increase of cells positive to the production of superoxide radical was found for positive control of doxorubicin.

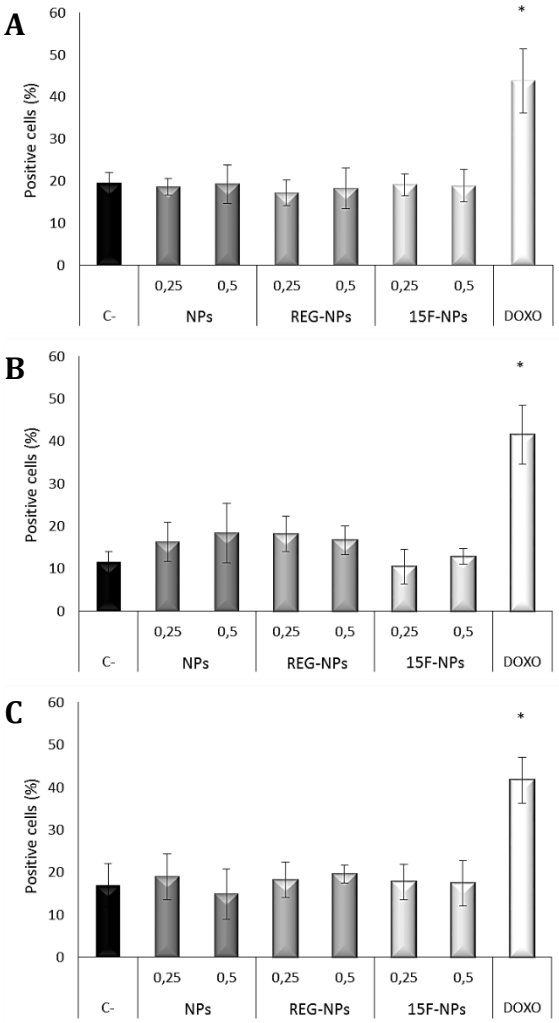


Figure 3.16 ROS generation in (A) IMR32, (B) astrocytes and (C) BBMVECs when exposed to 0,25 and 0,5 mg/ml NPs, 15F-NPs and REG-NPs concentrations, or to doxorubicin (n=18)

## ❖ Annexin A5 affinity assay on BBMVECs, human neuroblastoma cell line and rat glial cells

Cell Apoptosis in the different cell lines was evaluated by annexin V y propidium iodide. The results of flow cytometry are shown in Table 3.4 with the percentages of cells positive to annexin v and PI after treatments with different NPs forumlations at 0.25 and 0.5 mg/ml concentrations or positive control, doxorubicin, at concentration of 0.3 μg/ml. As can be seen, none of NPs formulations, compared with control, produced a significant increase in percentage of cells positive to annexin v or PI. Otherwise, a pronounced and statistically significant ($p<0.005$) percentage increase of cells positive to anexina V and IP was observed for doxorubicin.

Table 3.4 Cell Apoptosis in the different cell lines when exposed to 0,25 and 0,5 mg/ml NPs, 15F-NPs and REG-NPs concentrations, or to doxorubicin, evaluated by annexin V and propidium iodide

| **Astrocytes** | **Control** | | **0,25 mg/ml** | | **0,5 mg/ml** | | **doxo** | |
|---|---|---|---|---|---|---|---|---|
| | **Anexina V** | **IP** | **Anexina V** | **IP** | **Anexina V** | **IP** | **Annexin V** | **PI** |
| **NPs** | 14,94 ± 0,88 | 12,77 ± 3,58 | 12,85 ± 7,10 | 14,57 ± 2,53 | 12,54 ± 3,84 | 17,82 ± 3,34 | | |
| **REG-NPs** | 4,55 ± 0,76 | 10,05 ± 4,56 | 4,95 ± 2,12 | 17,00 ± 6,26 | 4,46 ± 0,70 | 15,93 ± 4,98 | 29.99 ± 4.99* | 42.45 ± 4,24* |
| **15F-NPs** | 6,59 ± 1,78 | 12,77 ± 3,58 | 7,30 ± 2,91 | 15,33 ± 3,09 | 3,69 ± 0,53 | 12,36 ± 3,61 | | |

| **BBMVECs** | **Control** | | **0,25 mg/ml** | | **0,5 mg/ml** | | **doxo** | |
|---|---|---|---|---|---|---|---|---|
| | **Anexina V** | **IP** | **Anexina V** | **IP** | **Anexina V** | **IP** | **Annexin V** | **PI** |
| **NPs** | 8,11 ± 3,51 | 10,16 ± 1,46 | 10,12 ± 2,55 | 11,38 ± 3,57 | 12,30 ± 1,80 | 10,11 ± 2,29 | | |
| **REG-NPs** | 5,92 ± 3,35 | 12,37 ± 6,48 | 10,06 ± 1,86 | 9,19 ± 1,93 | 8,87 ± 3,70 | 15,50 ± 2,54 | 28,62 ± 2,43* | 31,22 ± 4,27* |
| **15F-NPs** | 7,45 ± 1,53 | 11,68 ± 1,96 | 10,47 ± 3,44 | 8,12 ± 1,90 | 10,22 ± 2,20 | 7,29 ± 1,10 | | |

| **IMR-32** | **Control** | | **0,25 mg/ml** | | **0,5 mg/ml** | | **doxo** | |
|---|---|---|---|---|---|---|---|---|
| | **Anexina V** | **IP** | **Anexina V** | **IP** | **Anexina V** | **IP** | **Annexin V** | **PI** |
| **NPs** | 8,84 ±1,61 | 12,90 ± 2,47 | 5,86 ± 1,65 | 8,01 ± 2,53 | 8,74 ±3,15 | 10,68 ± 4,70 | | |
| **REG-NPs** | 11,94 ± 1,39 | 13,82 ± 1,45 | 12,78 ± 4,05 | 14,35 ± 2,90 | 10,03 ± 4,51 | 15,97 ± 2,63 | 19,90 ± 2,28* | 58,50 ± 4,03* |
| **15F-NPs** | 12,24 ± 0,97 | 11,67 ± 1,78 | 13,88 ± 3,87 | 11,90 ± 1,81 | 14,77 ± 3,27 | 11,88 ± 2,89 | | |

## In vitro blood-brain barrier transportation of PTX-peptide-functionalized NPs

The BBB is localized at the interface between blood and cerebral tissue [43], formed by the brain capillary endothelial cells (BCECs), basal lamina, glial cells, perithelial cells and so on. Among that, BCECs is the most important component to maintain the function of BBB because BCECs differed from other endothelial cells by (i) the absence of fenestration correlating with the presence of intracellular tight junctions, (ii) the low level of non-specific transcytosis and intracellular diffusion of hydrophilic compounds and (iii) the polarized expression of membrane receptors and transporters which are responsible for the active transport [44,45].

### ❖ Transendothelial transport experiments by NTA and UPLC

BBMVECs were chosen as an easy BBB model to study the brain delivery property of peptide-functionalized-PTX-NPs *in vitro*. To improve the barrier properties of BBMVECs cultures a co-culture of endothelial cells with primary astrocytes isolated from neonatal rats was developed. This approach has been shown significantly increasing transendothelial electrical resistance (TEER) value [46]. In order to assess the barrier integrity, BBB models were characterized in terms of trans-endothelial electrical resistance (TEER) and permeability (Pe) of the water-soluble molecular tracer Lucifer Yellow (LY). The obtained TEER values were higher than 200 $\Omega cm^2$, the measurements were performed after 72 hours from the co-culture establishment in 20 Transwells from each model. In order to further assess the quality of the established *in vitro* BBB models, BBMVECs permeability coefficient (Pe) to LY was determined for each culturing condition. As expected, the presence of glial cells in the model resulted in low LY Pe values (< 0.8 cm·min-1). The transport of peptide-functionalized-NPs from the luminal to the abluminal compartment was analyzed. REG-PTX-NPs and PTX-NPs were incubated in the luminal compartment of the BBB model for 60 minutes at 37ºC and with 5% of CO2. An insert without cells, incubating PTX-NPs in the luminal compartment was used as blank. Collected samples from the upper and the lower compartment, were analyzed by NTA and UPLC. As shown in Figure 3.17, REG-PTX-NPs in the luminal and abluminal compartments

reached the equilibrium of concentration. The same result was observed for PTX-NPs in both compartments of the insert without cells (blank). In contrast, PTX-NPs passage was restricted by the barrier indicating that the presence of REG-based decoration on the NPs surface increased the passage across the co-culture *in vitro* BBB model.

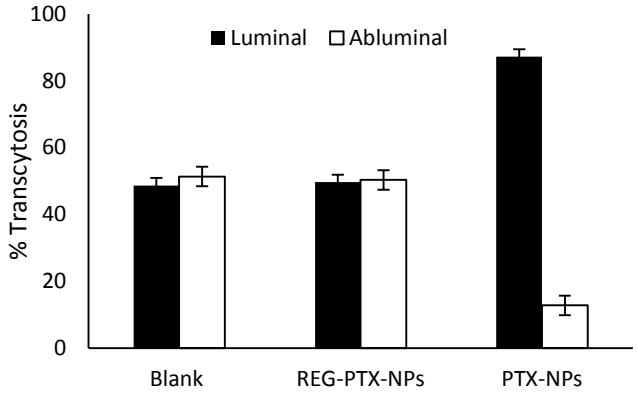


Figure 3.17 REG-PTX-NPs transport across co-culture in vitro BBB model quantified by NTA and UPLC (n=2)

### ❖ Transendothelial transport experiments by fluorometric detection

To study NPs toxicity and transendothelial transport efficiency on BBB *in vitro* models, fluorescently and peptide functionalized NPs at 0.25 and 0.5 mg/ml concentrations were employed. The integrity of both barrier models (bend3 and endothelial cells) was characterized by analyzing the permeability of the LY coincubated 1 hour with NPs solutions. As shown in Figure 3.18, all NPs formulations at both concentrations tested did not alter endothelial- and bend3-based barrier integrity since the permeability coefficient of LY was equivalent to that of the control cells.

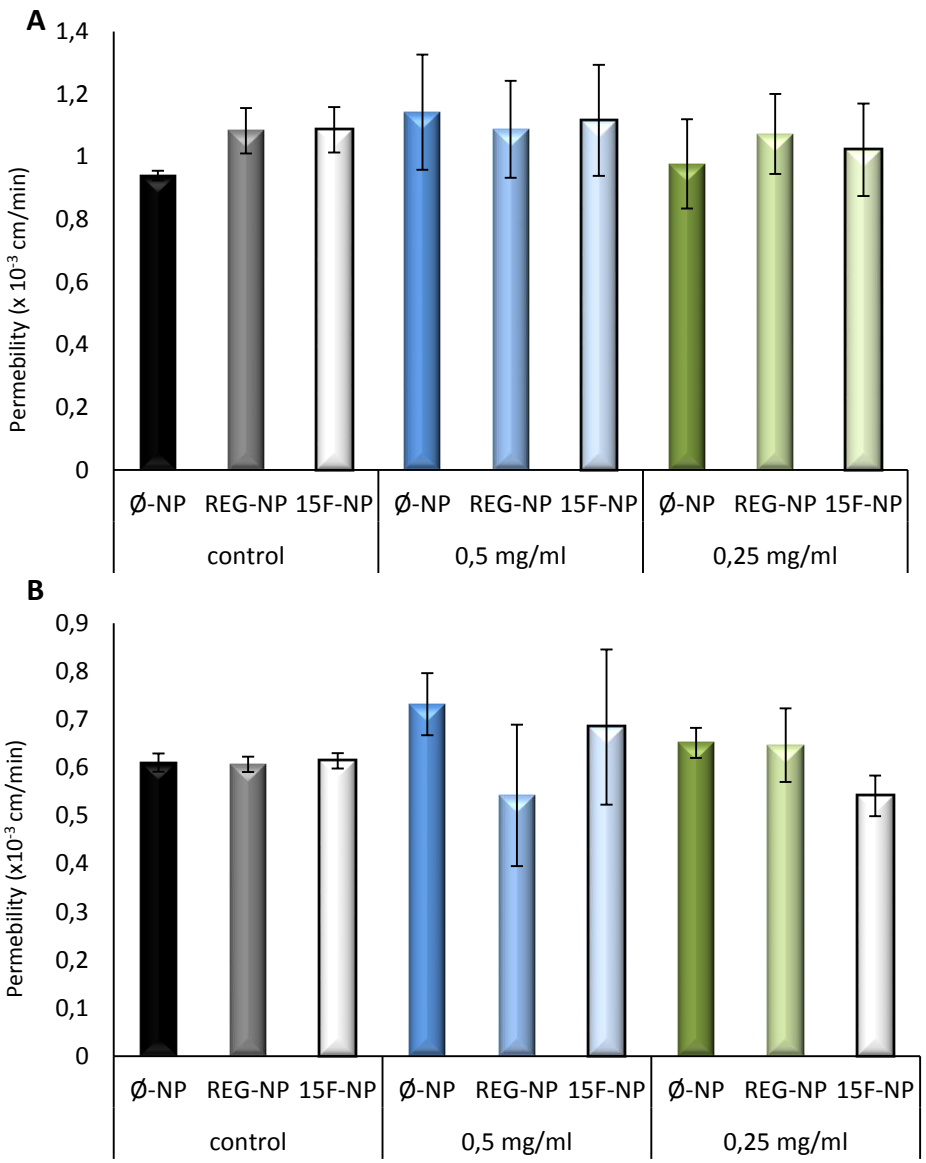


Figure 3.18 Integrity of the BBB model with (A) bend3 and (B) endothelial cells after 1 hour incubation with NPs, REG-NPs and 15F-NPs formulation at 0,5 and 0,25 mg/ml concentrations (n=9)

By a fluorometric quantitative study analyzing fluorescence emitted by AlexaFluor 568 labeled NPs, the transport of peptide-functionalized-NPs from the luminal to the abluminal compartment was analyzed. As shown in Figure 3.19 referred to bend3 BBB model, REG-NPs showed a not significant increase in permeability (0,5 mg/ml: 0,12 ± 0,01 x10-3 cm/min; 0,25 mg/ml: 0,13 ± 0,03 x10-3 cm/min) in comparison with NPs (0,5 mg/ml: 0,11 ± 0,01 x10-3 cm/min; 0,25 mg/ml: 0,10 ± 0.02 x10-3 cm/min). Otherwise, for 15F-NPs

an intensely increased permeability (p<005) due to the efficient peptide-functionalization was obtained (0,5 mg/ml: 0,22 ± 0,02 x10-3 cm/min; 0,25 mg/ml: 0,22 ± 0,01 x10-3 cm/min). With the endothelial BBB model it was observed again, an insignificant increase in REG-NPs permeability against a considerable higher transendothelial transport capability increase (p<0,005) of 15F-NPs.

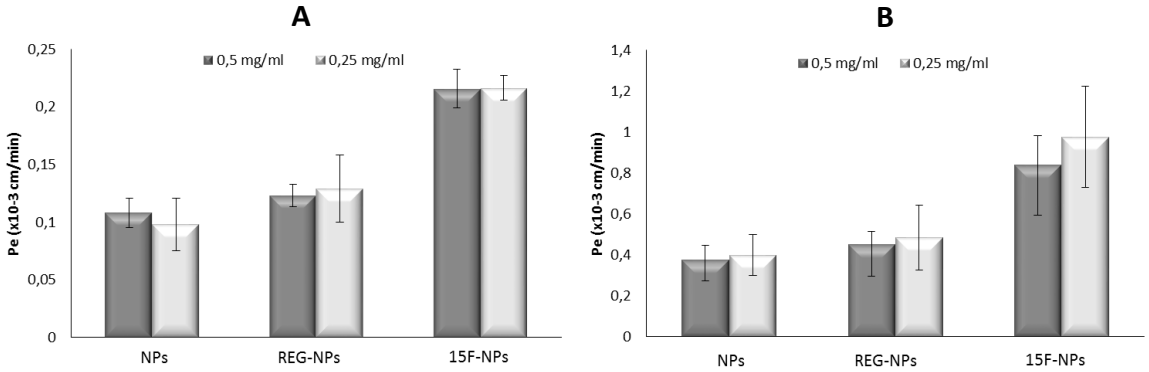


Figure 3.19 Permeability coefficient of NPs, REG-NPs and 15F-NPs across (A) bend3 and (B) endothelial culture in vitro BBB model quantified by fluorimetry (n=9)

## 3.4 Concluding Remarks

We have employed peptides (15F, REG) known to be efficiently transported across the BBB as a targeting moiety to develop a dual-targeting drug delivery system. A novel biodegradable block co-polymer (2P) has been successfully synthetized to obtain in only one step via modified nanoprecipitacion emulsifier-free, a very monodisperse peptide-PTX-NPs population, spherical in shape, with particle size of ~180 nm, polydispersity of ~0.1 and with a surrounding PEG corona on the surface. High drug loading, probably due to strong lipophilic interactions of PTX with hydrophobic inner region of NPs, has been obtained and *in vitro* PTX release from NPs has exhibited an approximately first-order profile, with a controlled release depending on the total cargo, for a prolonged period of time. *In vitro* studies have confirmed a pronounced cellular uptake of peptide functionalized-PTX-NPs by U-87 MG and BBMVECs cells. Dual-targeting effect has been demonstrated not only by a significant increased transendothelial transport ratio of PTX in an *in vitro* BBB model but also by enhanced *in vitro* anti-tumoral activity against U-87 MG. Considering these promising results, next chapter (Chapter IV) is centered in the *in vivo* characterization of the developed nanocarriers. Relevant *in vivo* properties of the NPs are explored to assess their biological profile in view of their application as a target anticancer delivery system.

## 3.5 Rerefences


1. K. Greish, Enhanced permeability and retention of macromolecular drugs in solid tumors: A royal gate for targeted anticancer nanomedicines, J. Drug Target. 15**,** 457–464 **(2007)**

2. R. K. Jain, Delivery of molecular and cellular medicine to solid tumors, 46**,** 149–168 **(2001)**

3. I. Brigger, C. Dubernet and P. Couvreur, Nanoparticles in cancer therapy and diagnosis., Adv. Drug Deliv. Rev. 54**,** 631–51 **(2002)**

4. L. R. Gref R, Minamitake Y, Peracchia MT, Trubetskoy V, Torchilin V, Biodegradable long-circulating polymeric nanospheres, Science (80-. ). 263**,** 1600–3 **(1994)**

5. S. M. Moghimi, a C. Hunter and J. C. Murray, Long-circulating and target-specific nanoparticles: theory to practice., Pharmacol. Rev. 53**,** 283–318 **(2001)**

6. R. Langer, Drug delivery and targeting, Nature 392**,** 5–10 **(1998)**

7. W. M. Pardridge, Why is the global CNS pharmaceutical market so underpenetrated?, Drug Discov. Today 7**,** 5–7 **(2002)**

8. G. W. Bemis and M. a. Murcko, Designing Libraries with CNS Activity, J. Med. Chem. 42**,** 4942–4951 **(1999)**

9. A. K. Ghose, V. N. Viswanadhan and J. J. Wendoloski, A Knowledge-Based Approach in Designing Combinatorial or Medicinal Chemistry Libraries for Drug Discovery . 1 . A Qualitative and Quantitative Characterization of Known Drug Databases, 55–68 **(1999)**

10. W. M. Pardridge, Blood-brain barrier drug targeting: the future of brain drug development., Mol. Interv. 3**,** 90–105, 51 **(2003)**

11. W. M. Pardridge, Short Review CNS Drug Design Based on Principles of Blood — Brain Barrier Transport, **(1998)**

12. W. M. Pardridge, Blood-brain barrier biology and methodology., J. Neurovirol. 5**,** 556–69 **(1999)**

13. R. D. Bell, A. P. Sagare, A. E. Friedman, G. S. Bedi, D. M. Holtzman, R. Deane and B. V Zlokovic, Transport pathways for clearance of human Alzheimer's amyloid beta-peptide and apolipoproteins E and J in the mouse central nervous system., J. Cereb. Blood Flow Metab. 27**,** 909–18 **(2007)**

14. M. Shibata, S. Yamada, S. R. Kumar, M. Calero, J. Bading, B. Frangione, D. M. Holtzman, C. A. Miller, D. K. Strickland, J. Ghiso and B. V Zlokovic, Clearance of Alzheimer ' s amyloid- β 1-40 peptide from brain by LDL receptor – related protein-1 at the blood-brain barrier, 106**,** 1489–1499 **(2000)**

15. S. Ito, S. Ohtsuki and T. Terasaki, Functional characterization of the brain-to-blood efflux clearance of human amyloid-beta peptide (1-40) across the rat blood-brain barrier., Neurosci. Res. 56**,** 246–52 **(2006)**

16. L. Maletínská, E. A. Blakely, K. A. Bjornstad, L. L. R. Protein, L. Maletı, D. F. Deen, L. J. Knoff and T. M. Forte, Human Glioblastoma Cell Lines : Levels of Low-Density Lipoprotein Receptor and Low-Density Lipoprotein Receptor-related Protein Human Glioblastoma Cell Lines : Levels of Low-Density Lipoprotein Receptor and, 2300–2303 **(2000)**

17. M. Yamamoto, K. Ikeda and K. Ohshima, Increased Expression of Low Density Lipoprotein Receptor-related Protein / α 2-Macroglobulin Receptor in Human Malignant Astrocytomas Increased Expression of Low Density Lipoprotein Receptor-related Macroglobulin Receptor in Human Malignant Astrocytomas, 2799–2805 **(1997)**

18. a Régina, M. Demeule, C. Ché, I. Lavallée, J. Poirier, R. Gabathuler, R. Béliveau and J.-P. Castaigne, Antitumour activity of ANG1005, a conjugate between paclitaxel and the new brain delivery vector Angiopep-2., Br. J. Pharmacol. 155**,** 185–97 **(2008)**

19. L. Brannon-Peppas and J. O. Blanchette, Nanoparticle and targeted systems for cancer therapy., Adv. Drug Deliv. Rev. 56**,** 1649–59 **(2004)**

20. A. M. Harmon, M. H. Lash, S. M. Sparks and K. E. Uhrich, Preferential cellular uptake of amphiphilic macromolecule-lipid complexes with enhanced stability and biocompatibility., J. Control. Release 153**,** 233–9 **(2011)**

21. F. Danhier, N. Lecouturier, B. Vroman, C. Jérôme, J. Marchand-Brynaert, O. Feron and V. Préat, Paclitaxel-loaded PEGylated PLGA-based nanoparticles: in vitro and in vivo evaluation., J. Control. Release 133**,** 11–7 **(2009)**

22. H. Xin, L. Chen, J. Gu, X. Ren, Z. Wei, J. Luo, Y. Chen, X. Jiang, X. Sha and X. Fang, Enhanced anti-glioblastoma efficacy by PTX-loaded PEGylated poly(ε-caprolactone) nanoparticles: In vitro and in vivo evaluation., Int. J. Pharm. 402**,** 238–47 **(2010)**

23. Y. Yu, J. Zou, L. Yu, W. Ji, Y. Li, W. Law and C. Cheng, Functional Polylactide- g -Paclitaxel À Poly ( ethylene glycol ) by Azide À Alkyne Click Chemistry, 4793–4800 **(2011)**

24. Y. Tao, R. Liu, M. Chen, C. Yang and X. Liu, Cross-linked micelles of graftlike block copolymer bearing biodegradable ε-caprolactone branches: a novel delivery carrier for paclitaxel, J. Mater. Chem. 22**,** 373 **(2012)**

25. X. Jiang, H. Xin, X. Sha, J. Gu, Y. Jiang, K. Law, Y. Chen, L. Chen, X. Wang and X. Fang, PEGylated poly(trimethylene carbonate) nanoparticles loaded with paclitaxel for the treatment of advanced glioma: in vitro and in vivo evaluation., Int. J. Pharm. 420**,** 385–94 **(2011)**

26. J. S. Moghimi, S.M., Stealth liposomes and long circulating nanoparticles: critical issues in pharmacokinetics, opsonization and protein-binding properties, Prog. Lipid Res. 42**,** 463–478 **(2003)**

27. B. Zhang, X. Sun, H. Mei, Y. Wang, Z. Liao, J. Chen, Q. Zhang, Y. Hu, Z. Pang and X. Jiang, LDLR-mediated peptide-22-conjugated nanoparticles for dual-targeting therapy of brain glioma., Biomaterials 34**,** 9171–82 **(2013)**

28. P. P. Di Mauro and S. Borrós, Development of High Drug Loaded and Customizing Novel Nanoparticles for Modulated and Controlled Release of Paclitaxel., Pharm. Res. **(2014)**

29. Y. Zhang, J. Hou, C. Qian, L. Song and S. Guo, Taxol-Loaded Nanoparticles with Methoxy Poly ( ethylene glycol ) - b -Poly ( e -caprolactone ) as a Novel Additive in the Outer Aqueous Phase, **(2011)**

30. S. Y. Kim, I. G. Shin, Y. M. Lee, C. S. Cho and Y. K. Sung, Methoxy poly(ethylene glycol) and epsilon-caprolactone amphiphilic block copolymeric micelle containing indomethacin. II. Micelle formation and drug release behaviours., J. Control. Release 51**,** 13–22 **(1998)**

31. R. K. Averineni, G. V Shavi, A. K. Gurram, P. B. Deshpande, K. Arumugam, N. Maliyakkal, S. R. Meka and U. Nayanabhirama, PLGA 50:50 nanoparticles of paclitaxel: Development, in vitro anti-tumor activity in BT-549 cells and in vivo evaluation, Bull. Mater. Sci. 35**,** 319–326 **(2012)**

32. G. Gaucher, R. H. Marchessault and J.-C. Leroux, Polyester-based micelles and nanoparticles for the parenteral delivery of taxanes., J. Control. Release 143**,** 2–12 **(2010)**

33. Q. Hu, G. Gu, Z. Liu, M. Jiang, T. Kang, D. Miao, Y. Tu, Z. Pang, Q. Song, L. Yao, H. Xia, H. Chen, X. Jiang, X. Gao and J. Chen, F3 peptide-functionalized PEG-PLA nanoparticles co-administrated with tLyp-1 peptide for anti-glioma drug delivery., Biomaterials 34**,** 1135–45 **(2013)**

34. M. Demeule, J.-C. Currie, Y. Bertrand, C. Ché, T. Nguyen, A. Régina, R. Gabathuler, J.-P. Castaigne and R. Béliveau, Involvement of the low-density lipoprotein receptor-related protein in the transcytosis of the brain delivery vector angiopep-2., J. Neurochem. 106**,** 1534–44 **(2008)**

35. J. Maupetit, P. Derreumaux and P. Tufféry, A fast method for large-scale de novo peptide and miniprotein structure prediction., J. Comput. Chem. 31**,** 726–38 **(2010)**

36. J. Maupetit, P. T. And and P. Derreumaux, A coarse-grained protein force field for folding and structure prediction, Proteins Struct. Funct. Bioinforma. 69**,** 394–408 **(2007)**

37. R. G. Kaur H, Garg A, PEPstr: a de novo method for tertiary structure prediction of small bioactive peptides, Protein Pept Lett. 14**,** 626–31 **(2007)**

38. G. Mezö, N. Mihala, D. Andreu and F. Hudecz, Conjugation of epitope peptides with SH group to branched chain polymeric polypeptides via Cys(Npys)., Bioconjug. Chem. 11**,** 484–91 **(2000)**

39. C. Fillebeen, L. Descamps, M.-P. Dehouck, L. Fenart, M. Benaissa, G. Spik, R. Cecchelli and a. Pierce, Receptor-mediated Transcytosis of Lactoferrin through the Blood-Brain Barrier, J. Biol. Chem. 274**,** 7011–7017 **(1999)**

40. M. Demeule, J. Poirier, J. Jodoin, Y. Bertrand, R. R. Desrosiers, C. Dagenais, T. Nguyen, J. Lanthier, R. Gabathuler, M. Kennard, W. a Jefferies, D. Karkan, S. Tsai, L. Fenart, R. Cecchelli and R. Béliveau, High transcytosis of melanotransferrin (P97) across the blood-brain barrier., J. Neurochem. 83**,** 924–33 **(2002)**

41. W. Pan, A. J. Kastin, T. C. Zankel, P. van Kerkhof, T. Terasaki and G. Bu, Efficient transfer of receptor-associated protein (RAP) across the blood-brain barrier., J. Cell Sci. 117**,** 5071–8 **(2004)**

42. H. Emonard, L. Théret, a H. Bennasroune and S. Dedieu, Regulation of LRP-1 expression: make the point., Pathol. Biol. (Paris). 62**,** 84–90 **(2014)**

43. J. M. Walker, The Blood-Brain and Other Neural Barriers, **(**2011**)**

44. N. Weiss, F. Miller, S. Cazaubon and P.-O. Couraud, The blood-brain barrier in brain homeostasis and neurological diseases., Biochim. Biophys. Acta 1788**,** 842–57 **(2009)**

45. M. a Petty and E. H. Lo, Junctional complexes of the blood-brain barrier: permeability changes in neuroinflammation., Prog. Neurobiol. 68**,** 311–23 **(2002)**

46. S. Lundquist, M. Renftel, J. Brillault, L. Fenart, R. Cecchelli and M.-P. Dehouck, Prediction of drug transport through the blood-brain barrier in vivo: a comparison between two in vitro cell models., Pharm. Res. 19**,** 976–81 **(2002)**

# CHAPTER IV.

## *In Vivo* evaluation of NPs pharmacokinetic properties

## 4.1 Introduction

Chapter II and Chapter III have developed a peptide targeted drug delivery system able to modulate and control the release of PTX across an *in vitro* BBB model and specifically, on human glioma cells. Since promising *in vitro* ability to shuttle and deliver PTX over the BBB, the NPs system has been translated to *in vivo* conditions to evaluate biological activities, focusing on pharmacokinetics properties (mainly biodistribution), and in particular on brain uptake. Effectively, evaluating the *in vivo* fate of a candidate nanocarriers in animals is a necessary step to estimate its potential as a targeted drug delivery agent.

Nanocarriers designed for the selective delivery of drugs to specific tissues or organs after systemic administration require a long circulation times in the bloodstream, in order to reach the targeted organ or tissue before clearance or degradation occurs [1–4]. This is not likely to happen if the carrier is taken up by RES organs (liver, spleen and bone marrow) immediately after intravenous administration or if rapid renal excretion occurs. Similar considerations are needed for nanostructure meant to be a circulating reservoir for sustained release of therapeutic cargoes. Hence, investigation of the pharmacokinetic properties of NPs for controlled release is of paramount importance.

Different approaches can be used to investigate the pharmacokinetic properties of NPs. Visualization methods such as optical or electron microscopies are often employed. Microscopy requires fluorescent dyes, loaded into NPs or covalent coupled to particle building blocks[5,6], to visualize the fluorescence emission in the whole body of a living small animal (e.g. NPs uptake in organs)[7,8]. Next to fluorescence microscopy, electron microscopy is commonly used. With this technique, single particles can be visualized (e.g. in specific regions of the brain). Although *in vivo* imaging is a rapidly progressing field, detection is at present not sensitive enough to visualize the particles within the microenvironment of the brain for example, or to provide quantitative information on the usually low concentrations that have accumulated.

The first part of this chapter focuses on two radiolabelling strategies for NPs and peptide for PET-CT imaging and gamma counting, respectively employing radionuclides positron and gamma emitters. As discussed in Chapter III, one important advantage of using NPs as a platform for drug delivery is the possibility to incorporate or conjugate multiple agents or functional groups. Among them, agents for non-invasive imaging by means of nuclear imagine technique represent an ideal tool for investigate *in vivo* fate of the NPs, including stability in biological environments (stealthiness), pharmacokinetics and specific organ uptake[9].

To quantitatively study the *in vivo* uptake of candidate nanocarriers at the target site with high sensitivity, the particle itself or an entrapped compound can be radiolabeled. Most commonly, radioisotopes like $^{3}H$, $^{18}F$, $^{14}C$ or $^{125}I$ are used. Radiolabelling can be performed with or without slight modifications of the original NP surface. For ligands to bind effectively, each radionuclide can be conjugated directly on the NP surface, with or without a spacer, or can be attached to the NPs during chemical synthesis. The spacer groups between the NP surface and the radionuclide or the biomolecule can be a simple hydrocarbon chain, a peptide sequence or a polyethylene glycol linker [10].

*In vivo* imaging techniques such as Positron Emission Tomography (PET), Single Photon Emission Computerized Tomography (SPECT), Magnetic Resonance Imaging (MRI) or Fluorescence Tomography show high sensitivity and tissue penetration and are widely used to investigate the *in vivo* characteristics of NPs. These techniques can be applied both to small and large animal species as well as humans and allow the determination of quantitative pharmacokinetics by imaging the uptake of the NPs[9].

It has to be considered how NPs are interacting with tissues and cells, and especially which time frame allows a suitable visualization of certain effects and functions. The physical half-life ($T_{½}$) of the radionuclide plays a crucial role for measurements in the desired time

frame, and it has to be considered which radionuclide or half-life, respectively, is suitable for the investigated question and pharmacokinetic profile (Scheme 4.1).

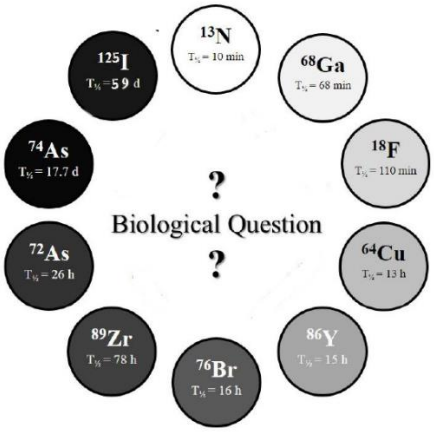


Scheme 4.1 The Clock-Of-Nuclides showing the positron emitters used for radiolabelling of NPs or peptides[11]

The $^{18}$F positron emitter is a very attractive radionuclide for radiolabelling of NPs due to its relatively long half-lived ($T_{1/2}$ = 109.7 min) and can be produced as [$^{18}$F]$F^-$ in the GBq scale in all biomedical cyclotrons. $^{18}$F emits a positron from the nucleus traveling only a short distance through the tissue before interact with a free electron. The outcome of this interaction (Annihilation) produce two antiparallel photons with energy 511 keV, independent of their kinetic energy (Scheme 4.2).

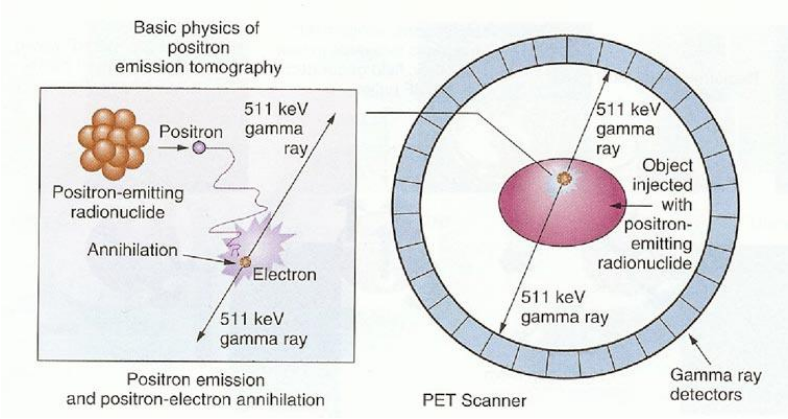


Scheme 4.2 Decay of $^{18}$F and basic physics of Positron Emission Tomography (PET) Imaging

Unfortunately, direct labelling with [$^{18}$F]F$^-$ requires harsh conditions (for example, high temperature and water-free organic solvent), and long reaction times;[12] alternatively, indirect labelling methods can be used. In this chapter, a radiolabeled prosthetic group is prepared in a first step, purified, and subsequently coupled to the molecule of interest, usually under mild conditions.

Alternatively, radioactive iodine is another useful tool for labelling of various large and small molecules. Many radioiodination methods, including electrophilic radio-iodination with various oxidants, and isotopic exchange with or without catalyst, have been well established for small organic molecules[13]. Radioiodination techniques include a variety of electropositive iodine sources, such as molecular iodine, iodine monochloride, NaI or KI with chloramine-T or iodogen, electrolytic methods, and enzymatic methods. Many different substances can be labeled by radioiodination. In most of studies with labeled molecules, it is necessary to measure very low concentrations of the substance under investigation, which in turn requires the preparation of high specific radioactivity labeled species. Two radioisotopes of iodine are widely available, $^{125}$I and $^{131}$I. $^{125}$I has a half-life of nearly 59 days and decays by electron capture to an excited state of $^{125}$Te, which decays immediately by gamma ray emission with a maximum energy of 35.5 keV (Scheme 4.3). $^{131}$I has a half-life of 8.02 days and decays 100% by electron emission, also resulting in the emission of gamma rays with a maximum energy of 364.5 keV. As γ-emitters, both are useful for *in vitro* and *ex vivo* applications; the application of $^{125}$I *in vivo* is restricted due to the low energy of the gamma rays, which may lead to a significant attenuation, especially in large animals or humans.

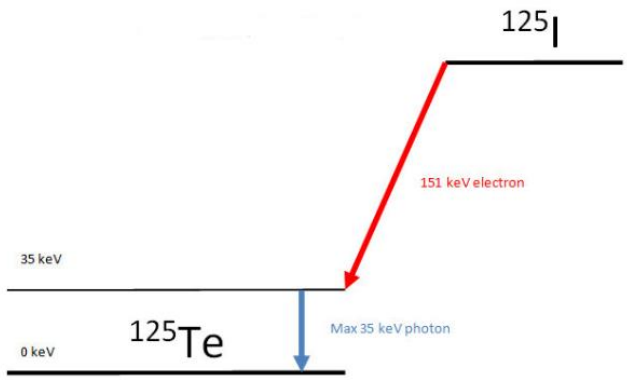


Scheme 4.3 Decay of $^{125}I$

Labelling methods for potential drug delivery systems are an indispensable need to provide the radiolabeled analogue and this chapter describes novel strategies and various approaches for the radiolabelling of the developed drug delivery systems using positron and gamma emitters.

Pharmacokinetics provides a mathematical basis to assess the time course of NPs and their effects in the body. It enables the following processes to be quantified: (i) absorption (ii) distribution (iii) metabolism, (iv) excretion. These pharmacokinetic processes determine the NPs concentration in the body and a fundamental understanding of these parameters is required to design an appropriate drug delivery system. Ideally, the concentration of NPs should be measured at the site of action of the drug, that is, at the receptor. However, concentrations are normally measured in whole blood from which serum or plasma is generated. A variety of techniques is available for representing the pharmacokinetics of a compound or NP. The most usual is to view the body as consisting of compartments between which candidate nanocarriers moves and from which elimination occurs. The transfer of compound between these compartments is represented by rate constants.

In this chapter a pharmacokinetic study is carried out to study the influx of the radiolabeled and peptides functionalized NPs across the BBB after single iv bolus injection. Multiple-time regression analysis is adapted to assess the fraction of the administered dose that is distributed within the BBB complex or is excreted from the body, based on a two-compartment mathematical model proposed by Patlak, Blasberg, and Fenstermacher[14,15]. The unidirectional influx constant (Ki) of NPs formulations is calculated and compared with known crossing compounds. Along with pharmacokinetic parameters, biodistribution studies are also used as a quantitative method to study *in vivo* NPs brain uptake.

For γ emitting-based biodistribution studies, the nanoparticles are usually administered intravenously[16]. After administration, the animals are sacrificed at a specific time point, or preferably at several time points. The brain is taken out, along with some of the major organs where the particles are likely to end up, including liver and kidney. If a γ-emitting label is used, organs can be directly counted in a γ counter. The amount of compound found in the brain and other organs can be represented as mass/organ or mass/gram. In this way, the increase in brain uptake compared to the control sample is obtained. Along with the experimental samples, the injection sample, as it was administered to the animals, can be assayed for NPs using the same analytical method, so that the amount of NPs taken up into the brain can be expressed as a percentage of the injected dose (%ID).

As a result, this chapter seeks to explore new radiolabelling strategies by synthetizing and purifying optimized NPs, labeled with radionuclide gamma or positron emitters, to investigate their pharmacokinetics *in vivo* behaviour and biodistribution by PET and gamma counter. A special attention is given to the NPs uptake into the brain by using a theoretical model of blood-brain exchange in order to evaluate the potential of the peptide functionalized NPs as brain targeting drug delivery system.

## 4.2 Experimental Section

The experimental part of this work has been carried out in the Molecular and Functional Imaging Facility of CIC biomaGUNE.

### 4.2.1 Materials

1.8-Octanediol (98%), 2,2'-Dithiodipyridine (≥97%) and polyethyleneglycol (PEG, Mw 1.5 KDa) were purchased from Sigma (Sigma–Aldrich, USA). Glutaric acid (99%) was obtained from Alfa Aesar (USA). AGBBB015F (CGGKTFFYGGSRGKRNNFKTEEY) and Regulon (HKKWQFNSPFVPRADEPARKGKV HIPFPLDNITRVPMAREPTVIHGKREVTLHLHPDH) peptides fluorescently labeled with carboxyfluorescein and 5-Tamra, respectively, were synthesized by Innovagen AB (Sweden). PEG Thiol acids, α-Thio-ω-carboxy poly (ethylene glycol) (MW 458 and 3.000 Da) were supplied by Iris Biotech GmbH (Germany). PTX (≥ 97%) was provided by Yunnan Hande Bio-Tech CO, LTD, P.R. China. Iodination beads and Bolton-Hunter reagents were purchased from Thermo Scientific Pierce. All other chemicals were of analytical grade and were purchased from Sigma (Sigma–Aldrich, Germany).

### 4.2.2 Synthesis and characterization of [$^{18}$F]-labeled/peptide-functionalized NPs

#### Synthesis of $^{18}$F-labeled active agent $^{18}$F-[FBBA]

The prosthetic group 4-[$^{18}$F]fluorobenzyl-2-bromoacetamide ([$^{18}$F]FBBA, [$^{18}$F]**4,** Scheme 4.4) was synthesized following a previously reported methodology with minor modifications. 4-[$^{18}$F]fluorobenzonitrile ([$^{18}$F]**2**) was prepared by reaction of 4-Cyano-*N*,*N*,*N*-trimethylanilinium trifluoromethanesulfonate (**1**) with [$^{18}$F]$F^-$ generated by proton irradiation of [$^{18}$O]$H_2O$; [$^{18}$F]$F^-$ was first trapped in an anion exchange resin and subsequently eluted with $K_2CO_3$/$H_2O$ and Kryptofix2.2.2/MeCN. After azeotropic evaporation of the solvent, the dried potassium [$^{18}$F]fluoride-Kryptofix2.2.2 complex was

dissolved in dry DMSO and the resulting solution was reacted with **1** (130ºC, 10 min). The reaction mixture containing [$^{18}$F]**2** was cooled, the reaction crude was diluted with purified water (9 mL) and the mixture was flushed through a C-18 cartridge (Sep-Pak®, Waters). The retained labelled species was eluted with 1.5 mL of THF, dried over $Na_2SO_4$ and molecular sieve and reacted with $LiAlH_4$ in THF (120ºC, 2 min) to yield [$^{18}$F]**3**, which was further reacted with bromoacetyl bromide (solution in $CH_2Cl_2$). After addition of 2 mL of MeCN/water 1/1, the mixture was purified by high performance liquid chromatography (HPLC) using a VP125/10 Nucleosil 100-7C18 semipreparative column (Macherey-Nagel) as stationary phase and MeCN/water 1/1 as the mobile phase (retention time = 13 min) to yield [$^{18}$F]**4** in overall yield of 12% (decay corrected). The presence of the desired product was confirmed by HPLC and co-elution with reference standard, using an Agilent 1200 Series HPLC system with a multiple wavelength UV detector (λ = 254 nm) and a radiometric detector (Raytest). A RP-C18 column (Eclipse XDB C18, 4.6x150 mm, 5 µm particle size) was used as stationary phase. The elution solutions were A (water) and B (MeCN). The column was eluted with a gradient: t=0 min, 95% A, 5% B; t=0.5 min, 95% A, 5% B; t=7.5 min, 1% A, 99% B; t=10min, 1% A, 99% B, and the flow was 1 mL/min (retention time = 9.5 min, injected volume = 20 µL). The collected fraction was used without further treatment for subsequent labelling steps.

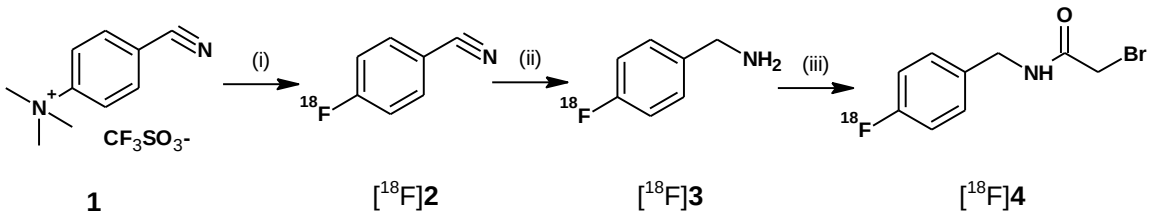


Scheme 4.4 Reaction for the preparation of [$^{18}$F]FBBA ([$^{18}$F]**4**); (i) azeotropically dried [$^{18}$F]$F^-$, $K_2CO_3$, $K_{2.2.2.}$, MeCN, 130°C, 10 min; (ii) 0.1M $LiAlH_4$, 2 min, 120 °C; (iii) bromoacetyl bromide in $CH_2Cl_2$, 2 min, RT

## Synthesis of $^{18}$F-[FBBA]-PEG-thiol-acids

Preparation of $^{18}$F-labelled PEG-thiol-acids was carried out by condensation of [$^{18}$F]-FBBA with the corresponding α-Thio-ω-carboxy poly (ethylene glycol). These experiments were

conducted to have a proof of principle of the feasibility of the condensation reaction. Experimentally, a 1 mg/ml solution of PEG-thiol-acid in 1:1 (v/v) phosphate buffer saline and acetonitrile (total volume = 250 µl), was mixed with a solution of [$^{18}$F]-FBBA in water/acetonitrile (250 µl). Two different PEG-thiol-acids with molecular weights of 458.6 and 3300 Da were used, and experimental conditions were optimized (T = 70-90°C, t = 10-30 min) in both cases. The radiochemical conversion was determined by radio-HPLC, using the same experimental conditions as above. For both polymers, the reaction proved to run smoothly at 90°C, yielding approximately 90% of radiochemical conversion after 10 minutes. Lower temperature required longer reaction times and lower radiochemical conversion values were achieved. Longer reaction times did not improve conversion. After optimization of experimental conditions, large scale syntheses for *in vivo* experiments were carried out using the optimal reaction time (T= 90°C, t = 10 min); the radiolabelled species were purified by HPLC under analytical conditions described above using a 500 µL injection loop. The fractions containing the pure labelled polymers were collected, allowed to complete decay and the identity of the labelled species was confirmed by UPLC/ESI-MS. Analyses were performed using an AQUITY UPLC separation module coupled to a LCT TOF Premier XE mass spectrometer (Waters, Manchester, UK). An Acquity BEH C18 column (1.7 µm, 5 mm, 2.1 mm) was used as stationary phase. The elution buffers were A (water and 0.1% formic acid) and B (Methanol and 0.1% formic acid). The column was eluted with a gradient: t=0 min, 95% A, 5% B; t=0.5 min, 95% A, 5% B; t=7.5 min, 1% A, 99% B; t=10min, 1% A, 99% B. Total run was 10 min, injection volume was 5 µL and the flow rate 300 µL/min. The detection was carried out in negative ion mode, monitoring the most abundant isotope peaks from the mass spectra.

## Synthesis of $^{18}$F-[FBBA]-P Block co-polymer ([$^{18}$F]P)

The radiosynthesis of $^{18}$F-[FBBA]-P Block co-polymer ([$^{18}$F]P) was approached for the subsequent preparation of $^{18}$F-labeled NPs. Experimentally, a 1 mg/ml solution of P in 1:1 (v/v) phosphate buffer saline and acetonitrile (total volume = 250 µL), was mixed with an equal volume of a solution of [$^{18}$F] FBBA in water/acetonitrile. The reaction was incubated at a pre-determined temperature and the radiochemical conversion was monitored at different times from chromatographic profiles (conditions described above). Different incubation times (30, 60, 90 and 120 min) and temperatures (90° and 120°C) were tested in order to achieve optimal conditions.

Large scale syntheses for *in vivo* experiments were carried out using the optimal reaction time (30 min) and temperature (90°C); the radiolabelled species were purified by HPLC under conditions described above, using a 500 µl injection loop.

## Synthesis and [$^{18}$F]-labelling of 3P block co-polymer ([$^{18}$F]3P)

The second strategy for the preparation of radiolabelling NPs required the preparation of a novel block co-polymer (3P) labeled with $^{18}$F. First, the microwave-assisted production of a pre-polymer was approached by reacting glutaric acid and 1.8-octanediol at a feeding molar ratio of 1:1.2 at 100 W for 1 hour. The reaction was performed under vacuum with continuous stirring and air-cooling to maintain the temperature at 120º C. The resulting pre-polymer, which contained an excess of 1.8-octanediol, was reacted with the PEG-thiol-acid (3.3 KDa) to obtain 3P block co-polymer. This second reaction was conducted in a microwave reactor under experimental conditions described above, using a ratio 1:1 (w/w) between pre-polymer and PEG-thiol-acid. Finally, radiolabelling of the 3P was achieved by condensation with $^{18}$F-[FBBA] under the same experimental conditions used for the preparation of $^{18}$F-labelled PEG-thiol-acids.

## Synthesis and characterization of [$^{18}$F]-labeled/peptide-functionalized-NPs

The synthesis of $^{18}$F-labelled/peptide functionalized NPs was approached by modifying the nano co-precipitation method described in Chapter III. Three different strategies were followed, depending on the labelled species used. The first strategy (Scheme 4.5 A) consisted of dissolve block co-polymers $^{18}$F-P and 2P at ratio 9:1 (w/w) in 1 ml of acetone to form the diffusing phase. This phase was then added to 20 ml of milliQ water, by means of a syringe, controlled by a syringe pump (KD Scientific) under magnetic stirring at room temperature; the needle was positioned directly in the medium and a flow rate of 50 µl/min was used. The resulting suspension was allowed to stir uncovered, in order to allow the evaporation of acetone. The suspension was purified by centrifugation (Hettich Centrifuge, EBA 21, 4000 g, 45 min at RT) with ultracentrifugal devices (Amicon Ultra-15, Ultracel membrane with 100,000 MWCO, Millipore, USA). The second strategy consisted of dissolving block co-polymers P, 2P and [$^{18}$F]3P in the organic phase (acetone) at ratio 8:1:1 (w/w) (Scheme 4.5 B), and following exactly the same experimental procedure.

Finally, and taking advantage of the hydrophobicity character of the labelled prosthetic group, a third strategy consisting of encapsulating $^{18}$F-[FBBA] into the peptide-functionalized NPs was approached (Scheme 4.5 C). With that aim, the labelled species ([$^{18}$F]FBBA) was dissolved in the organic phase (acetone, 1 ml) together with the starting polymers, and the solution was added dropwise to the aqueous phase under continuous stirring.

In all cases, the physiochemical properties (size and zeta potential) of the resulting $^{18}$F-labeled/peptide-functionalized NPs were determined after complete decay as described in Chapter III. To assess radiolabelling efficiency (R.E., %), the amount of radioactivity in the pellet and supernatant after centrifugation were determined, and R.E. was calculated using Equation 4.1

$$R.E.(\%) = \frac{A_{pellet}}{A_{pellet} + A_{supernat}} x100$$

Equation 4.1

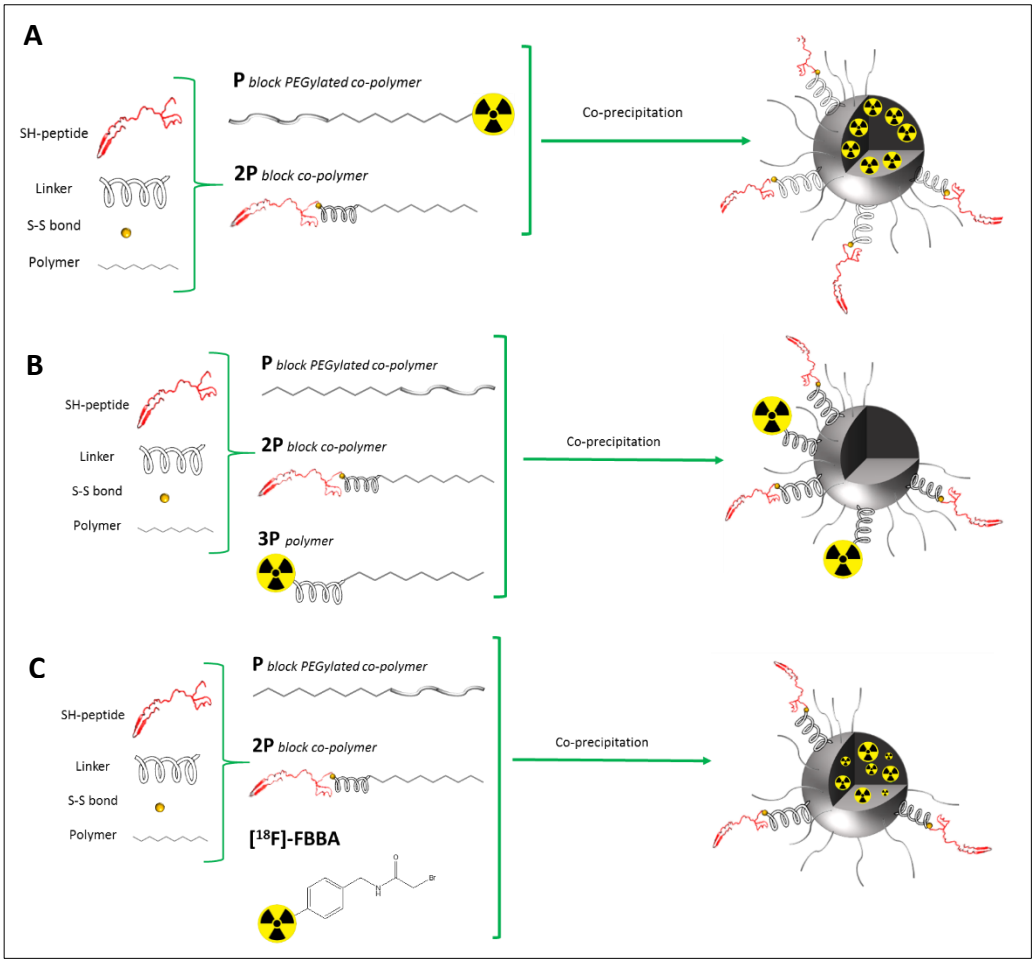


Scheme 4.5 Three strategies for the fabrication of $^{18}$F-labeled and peptide-functionalized-NPs via co-precipitation. Labeled parte are (A) block co-polymer P, (B) block co-polymer 3P and (C) [$^{18}$F]FBBA

To assess the radiochemical stability, NPs were prepared and purified as described above and subsequently resuspended in 200 µL of physiologic NaCl 0.9% solution (Braun Medical S.A.). The suspension was then divided into 4 different aliquots containing 50 µL of the NPs each. The aliquots were kept at 37°C for 1, 3, 24 and 48 hours, respectively. The samples were then filtered and radioactivity was measured in a 2470 WIZARD2 Automate

Gamma Counter (PerkinElmer). The dissociation of $^{18}F$ (expressed in percentage) at each time point was calculated as the ratio between the amount of radioactivity in the filtrate and the starting amount of radioactivity.

### 4.2.3 Synthesis and characterization of [$^{125}I$]-labeled/peptide-functionalized NPs

#### Iodination of 15F, REG peptides and characterization

Labelling with Iodine-125 involves incorporation of Iodine-125 into tyrosine residues within the peptide. 15F peptide was radiolabeled with standard procedure using iodo-beads. Briefly, beads (2 per iodination) were washed twice with 1 ml of PBS on a Whatman filter and resuspended in 60 µl of PBS (0.1 M pH 6.5). Na [$^{125}I$]I (approximately 1 MBq) was added to the beads suspension for 5 minutes at room temperature. Iodination of the peptide was initiated by the addition of 100 µl of 15F diluted in PBS at 150 ng/ml. At different incubation times (5, 10 15, 20 minutes, RT) the reaction was stopped by removing iodo-beads and the radiolabelling efficiency was determined by HPLC, using an Agilent 1200 Series HPLC system with a multiple wavelength UV detector (λ = 215 nm) and a radiometric detector (Gabi, Raytest). A RP-C18 column (Teknokroma, 18 µm, 15 x 0.46 mm) was used as stationary phase, and the mobile phase consisted of a gradient of A (0.1% TFA/water) and B (0.1% TFA/Acetonitrile); 0 min, 100% A; 30 min, 100% B; flow rate = 1 ml/min; retention time = 12.5 min). Large scale syntheses (37 MBq) for *in vivo* experiments were carried out using the optimal reaction time (15 min) and the radiolabelled 15F was purified by HPLC under identical conditions.

For REG-peptide, which lacks accessible tyrosine residues, free amines were derivatised with iodinated Bolton-Hunter reagent. Briefly, 2 µl of Bolton-Hunter reagent solution (0.5 mg/ml DMSO) were added to labelling buffer (50 mM sodium phosphate buffer, pH 7.5, ~1 MBq Na $^{125}I$). Chloramine-T (1µg/µl in 50 mM sodium phosphate buffer, pH 7.5) was immediately added and the mixture was incubated for 15 seconds. $^{125}I$-Labeled Bolton-

Hunter reagent was extracted by adding 5 µl of DMF and 100 µl of benzene; the aqueous phase was removed and the organic phase was dried by evaporation under a gentle stream of air. REG-peptide solution (150 ng/µl in 60 µl ice-cold 50 mM sodium borate buffer) was added to the dried, labeled reagent and after incubation for 2 hours on ice, the reaction mixture was analyzed by HPLC, using the same chromatographic system and experimental conditions specified above (λ=546, retention time = 12.5 min). Large scale syntheses (37 MBq) for *in vivo* experiments were carried out using identical experimental conditions and the radiolabelled REG-peptide was purified by HPLC under the same conditions. The stability of both labeled peptides was determined by HPLC at t=24 hours.

The radiolabelling of peptide-functionalized-2P block co-polymers was approached following the same protocols described above; iodination of the peptides was initiated by adding 200 µl of 2P block co-polymer at 5 mg/ml concentration in PBS and in sodium borate buffer for 15F-2P and REG-2P, respectively.

### Synthesis and characterization [$^{125}$I]-labeled and peptide-functionalized-NPs

Following the nano co-precipitation method developed in Chapter III and employing radiolabeled 2P block co-polymers, $^{125}$I-15F- and $^{125}$I -REG-functionalized NPs were obtained for *in vivo* experiments. Obtained $^{125}$I-labeled-NPs were physiochemical characterized, in terms of size and zeta potential, after complete decay, as described in Chapter III. Activity of the NPs pellet, after centrifugation, was measured before animal injection.

## 4.2.4 *In vivo* and ex vivo experiments

Healthy, 9-10 weeks aged Sprague-Dawley rats (Harlan, Udine, Italy) were used to examine the biodistribution pattern of radiolabelled and peptide-functionalized-NPs after intravenous injection. The animals were maintained and handled in accordance with the Guidelines for Accommodation and Care of Animals (European Convention for the Protection of Vertebrate Animals Used for Experimental and Other Scientific Purposes) and internal guidelines, and experimental procedures were approved by the Ethical

Committee and local authorities. Rats were acclimated to the housing facility at 25°C and 55% of humidity under light/dark conditions for at least 5 days prior to experiments.

## *In vivo* biodistribution in rats (PET-CT Imaging)

Animals were anesthetized with 4.5% isoflurane in pure oxygen as carrier gas. $^{18}$F-peptide-functionalized-NPs were suspended in a certain volume of saline solution (NaCl 0.9%) to obtain the required concentration of radioactivity (37-74 MBq/ml) and intravenously administered via one of the lateral tail veins. Formulations of $^{18}$F-3P and $^{18}$F-FBBA were also administered and used as controls.

PET-CT imaging was performed on an eXplore Vista-CT camera (GE Healthcare). Acquisition of the scans was started immediately after dose administration. Three beds were defined to acquire whole body images (frames: 2 x 2 min, 3 x 5 min, 2 x 10 min, total acquisition time = 117 min). After acquisition, a CT scan was performed for a later attenuation correction application in the image reconstruction. Random and scatter corrections were also applied to the reconstructed images (2DOSEM iterative algorithm, 4 iterations). PET-CT images were co-registered and analyzed using PMOD image processing tool. Volumes of interest (VOIs) were drawn in the kidneys, liver, stomach and brain, using the CT images for anatomical reference. Time–activity curves (decay corrected) were obtained for each organ as cps/cm$^3$. Curves were transformed into real activity (Bq/cm$^3$) curves by using a calibration factor. Injected dose and organ mass normalizations were finally applied to data.

## *Ex vivo* Pharmacokinetics and biodistribution in rats (Gamma-counter)

Healthy, 9-10 weeks aged Sprague-Dawley rats (Harlan, Udine, Italy) were used to examine the pharmacokinetics and biodistribution of peptide-functionalized-PTX-NPs. The animals were maintained and handled in accordance with the Guidelines for Accommodation and Care of Animals (European Convention for the Protection of Vertebrate Animals Used for Experimental and Other Scientific Purposes) and internal

guidelines, and experimental procedures were approved by the Ethical Committee. Rats were acclimated to the housing facility at 25ºC and 55% of humidity under light/dark conditions for 5 days before experiments. Animals were randomly divided into four groups (n=3 per group) and were anesthetized with 4.5% isoflurane in pure oxygen as carrier gas. $^{125}$I-15F, $^{125}$I-REG, $^{125}$I-15F-PTX-NPs and $^{125}$I-REG-PTX-NPs were suspended in a certain volume of saline solution (NaCl 0.9%) to obtain the required concentration of radioactivity (~1.85 MBq/mL). Peptides and NPs solutions were intravenously administered via one of the lateral tail veins. In each group, at pre-defined time points (2, 5 and 10 minutes post injection) mice were anesthetized and blood samples (c.a. 100 µl) were withdrawn by cardiac puncture. Immediately after, animals were anesthetized by exsanguination/perfusion using saline solution and main organs (liver, kidney, brain and cerebellum) were harvested, rinsed with PBS solution and stored in plastic vials at -20°C until being submitted to gamma counting. Blood samples were introduced into heparinized tubes, counted in the gamma counter (2470 Wizard2, PerkinElmer) and then submitted to centrifugation to separate the plasma (1000 g, 10 minutes) and stored at -20ºC until analysis by gamma counting. Measurements in the gamma counter were transformed into amount of radioactivity per gram of tissue by using a calibration curve, and values were normalized to injected amount of radioactivity to obtain the percentage of injected dose per gram of tissue (%ID/g) at each time point.

Multiple-time regression analysis was used to study the influx of radiolabeled peptides and NPs across the BBB. A two-compartment model of the BBB with unidirectional influx was used [14,15]. The unidirectional influx rate ($K_i$, expressed in units of microliters per-gram minute) and the apparent volume of distribution at time 0 ($V_i$ expressed in units of microliters per gram) were determined from the following equation:

$$Am/Cpt = K_i \left[ \int_0^t Cp(\tau) d\tau \right] / Cpt + V_i$$

Equation 4.2

where Am is the concentration of radioactivity in the brain, Cpt is the concentration of radioactivity in arterial plasma at time *t* and exposure time (Expt, expressed in minutes) is calculated as the integral of the concentration of radioactivity over time divided by the concentration of radioactivity at time t $[\int_0^t Cp(\tau)d\tau]/Cpt$. The slope of the linear region when plotting Am/Cpt vs Expt corresponds to $K_i$. The half-time disappearance and the distribution volume were calculated from the slope and the intercept, respectively, of the linear region obtained when plotting the log of the %ID/g in serum *vs* time. Drug clearance (CL), defined as the volume of plasma in the vascular compartment cleared of drug per unit time by process of metabolism and excretion, is related to half-life by the following equation:

$$CL = \frac{\ln 2 \ Vi}{t_{1/2}}$$

Equation 4.3

## 4.3 Results and Discussion

### 4.3.1 Synthesis and Characterization of [$^{18}$F]-labeled NPs

#### Characterization of $^{18}$F-FBBA and $^{18}$F-labeled polymers

The labelled active agent [$^{18}$F]-FBBA was synthesized following a well-established procedure [17]. The presence of the desired labelled species was confirmed by HPLC and co-elution with reference standard (Figure 4.1). Radiochemical yields similar to those previously reported in the literature (16%, decay corrected; total synthesis time approximately 90 min including purification) were achieved.

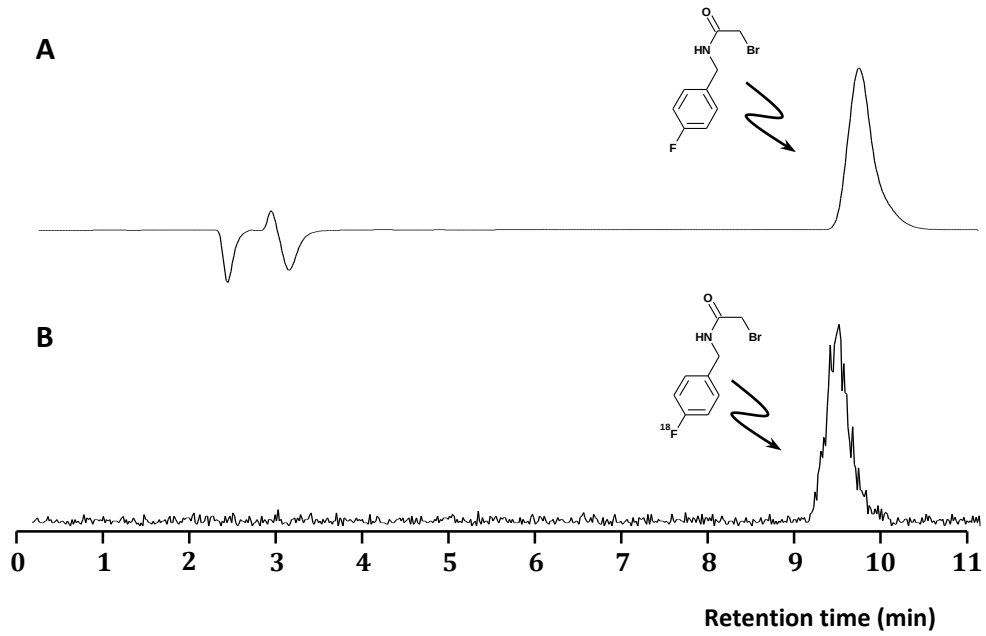


Figure 4.1 Labelled active agent characterization. HPLC chromatograms of (A) FBBA (reference standard solution, UV detector) and (B) [$^{18}$F]-FBBA (purified fraction, radiometric detector)

The coupling reaction of the PEG-thiol-acids with [$^{18}$F]-FBBA (Scheme 4.6) was optimized by using different temperatures and reaction times. In Figure 4.2, the radiochemical conversion values (obtained by direct integration of the radiometric chromatographic profiles) at different reaction times are shown (PEG-thiol-acid with MW = 458.6, T = 90°C). As it can be seen, similar radiochemical conversion values were obtained for t>10 min.

This kinetic profile was also observed for T=70°C, although lower conversion values (<85%) could be achieved and the plateau was slightly delayed (t>20 min). Very similar results were obtained for the higher MW PEG-thiol-acid. Figure 4.3 shows the chromatographic profiles (radiometric detector) of the reaction mixture at t=0 min and t=10 min. It can be seen that, for the lower MW polymer, the peak corresponding to the radiolabelled condensation product appears even at t=0. This is due to the time gap between reaction initiation and injection into HPLC (approximately 3 minutes). Thus, the reaction was taking place (slowly) at room temperature. After purification under optimal conditions, overall radiochemical yields of 51±7% (uncorrected) were achieved. UPLC-ESI/MS analysis of the collected fractions confirmed the presence of the condensation products (see for example Figure 4.4).

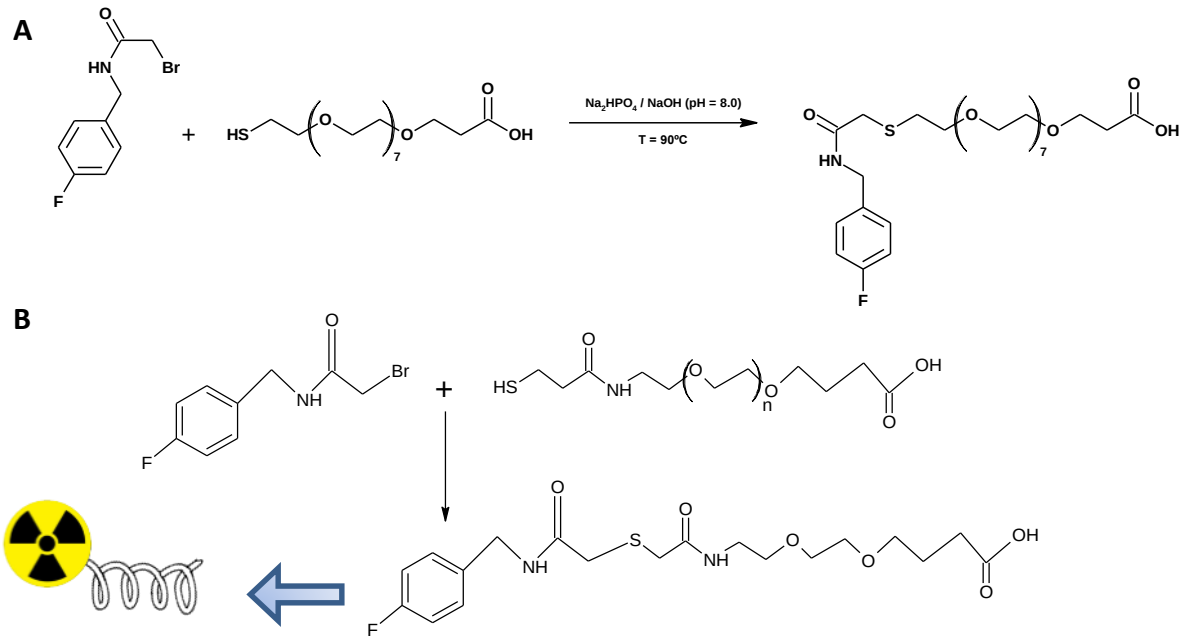


Scheme 4.6 Synthesis of [$^{18}$F]-FBBA-PEG-thiol-acids by the condensation of [$^{18}$F]FBBA with PEG-thiol-acid of (A) Mw 458.6 Da and (B) Mw 33 KDa

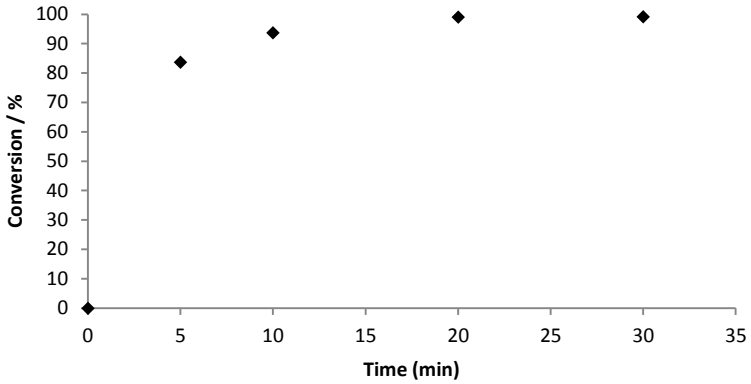


Figure 4.2 Radiochemical conversion of $^{18}$F-FBBA into $^{18}$F-FBBA-PEG as a function of time; T = 90 °C; MW = 458.6 Da

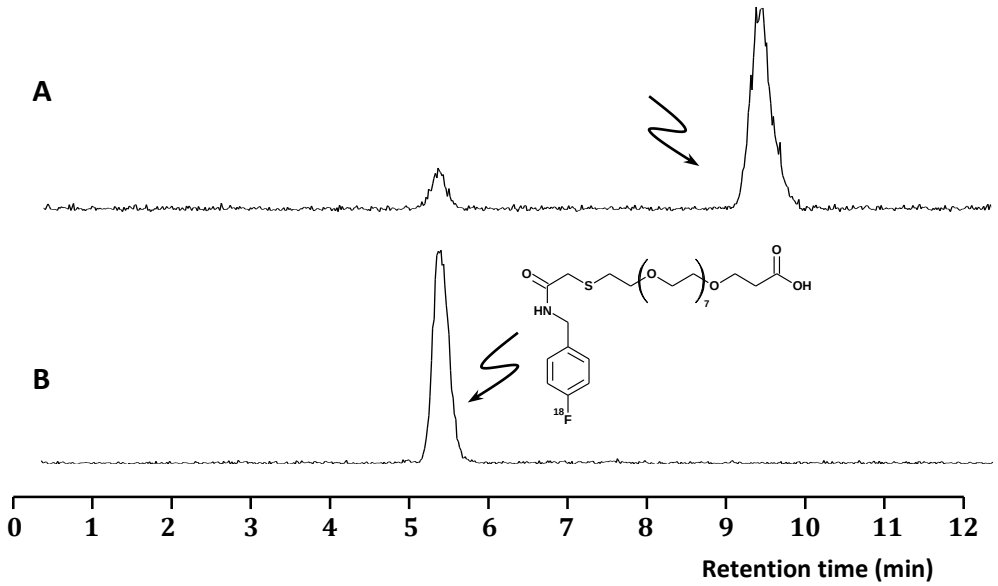


Figure 4.3 HPLC chromatograms obtained during reaction of PEG-thiol-acid low MW and [$^{18}$F]-FBBA. (A) Reaction time = 0 min; and (B) Reaction time = 10 min (T = 90˚C, radiometric detector)

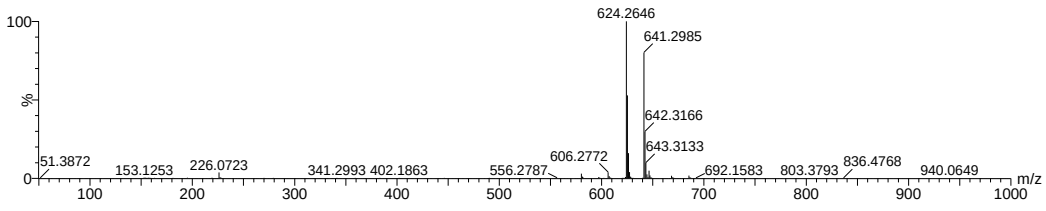


Figure 4.4 MS spectrum of [18F]-FBBA-PEG.

Incorporation of the labelled active agent $^{18}$F-[FBBA] into block-co polymers P and 3P was carried out following the chemical reaction schematized as shown in Scheme 4.7 and Scheme 4.8, respectively. Radiochemical conversion value of 52% and 65% were achieved for polymer P at 90 and 120°C, respectively (Figure 4.5). However, at 120°C the reaction occurred faster, reaching a plateauy after 30 minutes. The plateau was reached only after 120 min when the reaction was conducted at 90°C. For 3P block co-polymer, radiochemical conversion was approximately 60 % after 1 hour (Figure 4.6) when the reaction was carried out at 120°C.

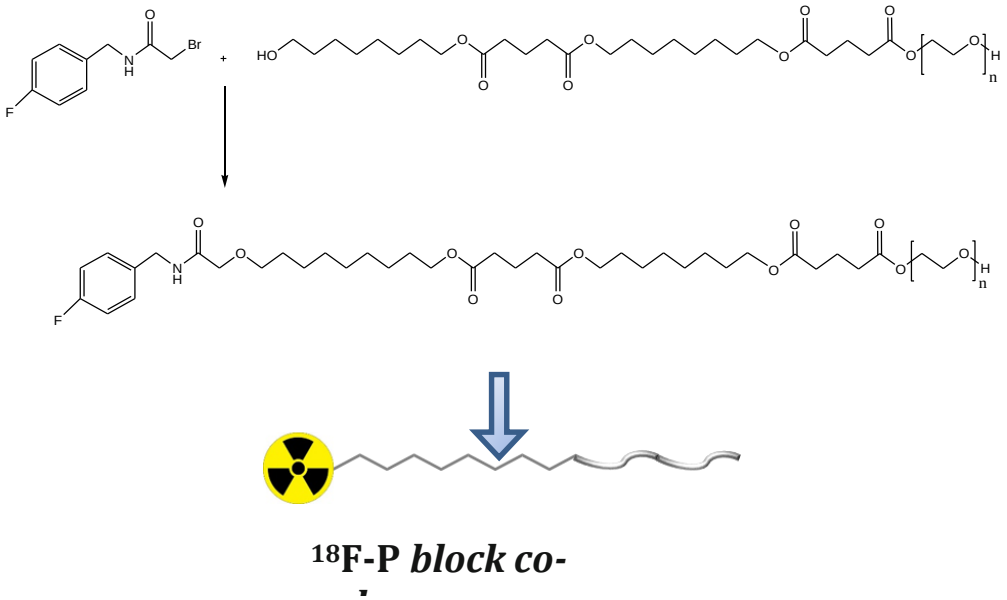


Scheme 4.7 Synthesis of [$^{18}$F]-FBBA-P block co-polymer

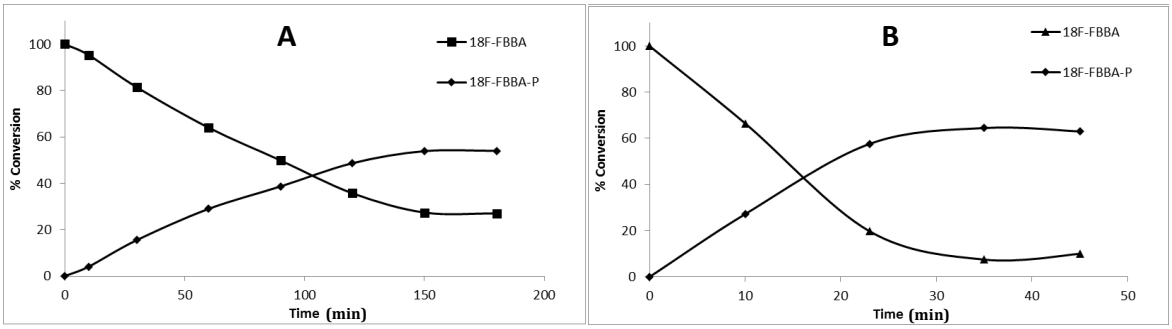


Figure 4.5 Radiochemical conversion of [$^{18}$F]-FBBA into [$^{18}$F]-FBBA-P as a function of time at (A) 90 ºC and (B) 120ºC

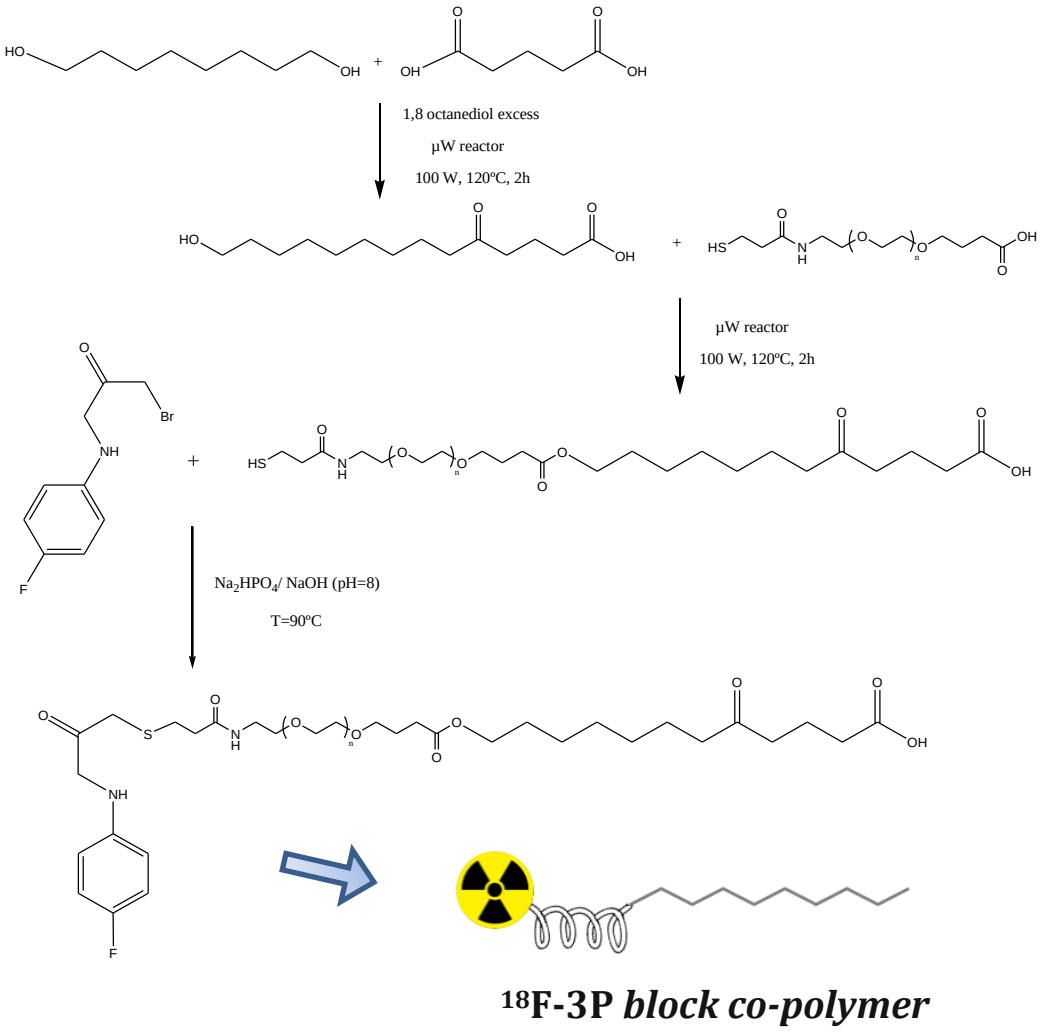


Scheme 4.8 Synthesis of [$^{18}$F]-FBBA-3P block co-polymer: obtained pre-polymer reacted with PEG-thiol-acid (Mw 33 KDa) and following condensated with [$^{18}$F]-FBBA

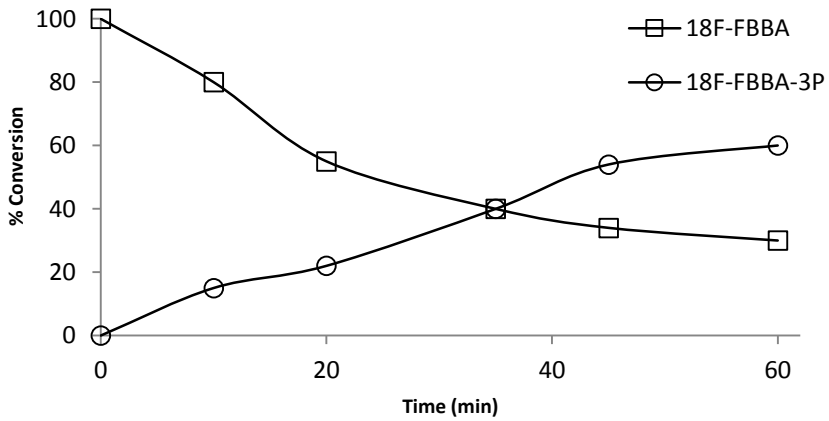


Figure 4.6 Conversion of [$^{18}$F]-FBBA into [$^{18}$F]-FBBA-3P as a function of time

## Synthesis and characterization of [$^{18}$F]-labeled NPs

By modifying the nano co-precipitation method described in chapter III, $^{18}$F-labeled and peptide-functionalized NPs were obtained following three different methods as specified in the experimental section of this chapter. These three strategies resulted in values of R.E. ranging from 5 to 14 %, related to the amount of starting radiolabelled polymer (strategies 1 and 2) or starting amount of [$^{18}$F]FBBA (strategy 3) (Table 4.1).

According to the measurements of particle size and zeta potential, the incorporation of the radiolabel did not result in statistically significant alteration of the physic-chemical properties of the resulting NPs; all the formulations exhibited average diameters and zeta-potential values within the required specifications (data not shown).

Radiochemical stability studies showed no detachment of the radioactivity for NPs prepared following strategies 1 and 2 (radiochemical purity > 95% after 48 hours). Slow detachment of [18F]FBBA was observed at long times for NPs synthesized following strategy 3.

Table 4.1 R.E. (%) for the NPs obtained by different strategies (radionuclide labelled to polymers P, 3P or encapsulated)

| **$^{18}$F-labelling strategy** | **Radiolabelling efficiency (%)** |
|---|---|
| $^{18}$F-P | 5 |
| $^{18}$F-3P | 14 |
| $^{18}$F-FBBA | 10 |

### 4.3.2 Synthesis and Characterization of [$^{125}$I]-labeled NPs

## Characterization of $^{125}$I-15F and $^{125}$I-REG

Many different substances can be labeled by radioiodination. In most of studies with labeled molecules, it is necessary to measure very low concentrations of the substance under investigation, which in turn requires the preparation of high specific radioactivity labeled species. Two radioisotopes of iodine are widely available, $^{125}$I and $^{131}$I. $^{125}$I has a half-life of nearly 59 days and decays by electron capture to an excited state of $^{125}$Te, which decays immediately by gamma ray emission with a maximum energy of 35.5 keV. $^{131}$I has a half-life of 8.02 days and decays 100% by electron emission, also resulting in the emission of gamma rays with a maximum energy of 364.5 keV (81.7%). As γ-emitters, both are useful for in vitro and ex vivo applications; the application of $^{125}$I in vivo is restricted due to the low energy of the gamma rays, which may lead to a significant attenuation, especially in large animals or humans. In the current study, $^{125}$I was the isotope of choice, due to its high specific radioactivity, reasonable price and adequacy for the purpose of the study. 15F-peptide was radiolabeled using a direct method in which labelling with $^{125}$I involved incorporation of $^{125}$I into tyrosine residues already present in the peptide (Scheme 4.9 A). This was done by treatment of the sample with Na$^{125}$I in the presence of an oxidizing reagent to generate a source of electrophilic iodine. Iodination takes place at the ortho-positions to the hydroxyl group on tyrosine and mono- or di-substitution can occur. To prevent the potential degradation of the peptide in the presence of strong oxidizing agents, an insoluble derivative of the sodium salt of N-chloro-benzenesulfonamide immobilized on nonporous, polystyrene beads (Iodo-Beads), was used as the oxidant. By using this reagent, the reaction was finalized by simply removing the beads from the reaction mixture. The radioiodination reaction kinetics was evaluated by determining the radiochemical incorporation at different times using HPLC equipped with a radiometric detector. As shown in Figure 4.7 A, the radioactivity ratio between free $^{125}$I and $^{125}$I-15F was analyzed after 5, 10, 15 and 20 minutes of reaction and the highest 15F radiolabelling efficiency was obtained after 15 minutes incubation ($^{125}$I free/$^{125}$I-

15F=34:66). To ensure $^{125}$I-15F compound stability, the same collected and purified fraction was analyzed after 24 hours and as shown in Figure 4.7 B, no free $^{125}$I was detected proving stable incorporation of iodine into tyrosine residues. Radiolabelling of 15F-functionalized-2P block co-polymer was also performed and the degree of radioisotope incorporation, analyzed by HPLC (Figure 4.7 C) was $^{125}$I / $^{125}$I-15F = 12/88.

REG-peptide lacks accessible tyrosine residues, and hence an indirect radiolabelling method was used; with this purpose, free amines were reacted with N-succinimidyl-3-[4-hydroxyphenyl] propionate (Bolton-Hunter) reagent, previously labelled with $^{125}$I. The presence of the N-hydroxysuccinimide (NHS) ester group reacts efficiently with primary amino groups of lysine at pH 7-9 to form stable amide bonds (Scheme 4.9 B). This condensation reaction was carried out in 15 minutes, leading to 77% labelling efficiency. The radiochemical stability of $^{125}$I-REG compound was analyzed after 24 hours by HPLC (Figure 4.8); no free $^{125}$I was detected. Radiolabelling of REG-functionalized-2P block co-polymer was also performed following a parallel strategy with radiochemical conversion values close to 80%.

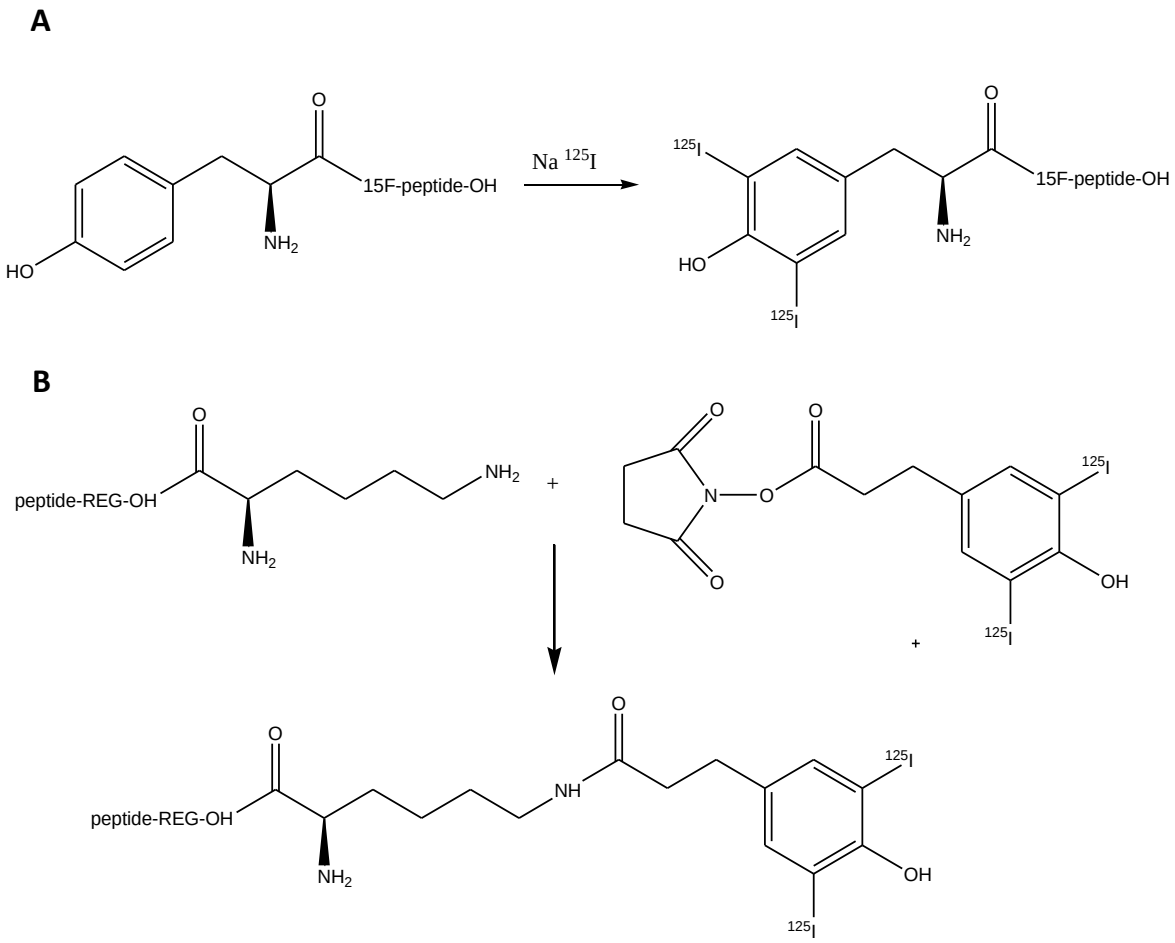


Scheme 4.9 Peptides radiolabelling with γ-emitting radioisotope $^{125}$I. (A) 15F-peptide radiolabeled by direct method incorporating $^{125}$I into tyrosine residues. (B) REG-peptide radiolabeled by indirect method involving conjugation of a preiodinated [$^{125}$I] Bolton-Hunter reagent to primary amines of lysine to form stable amide bonds

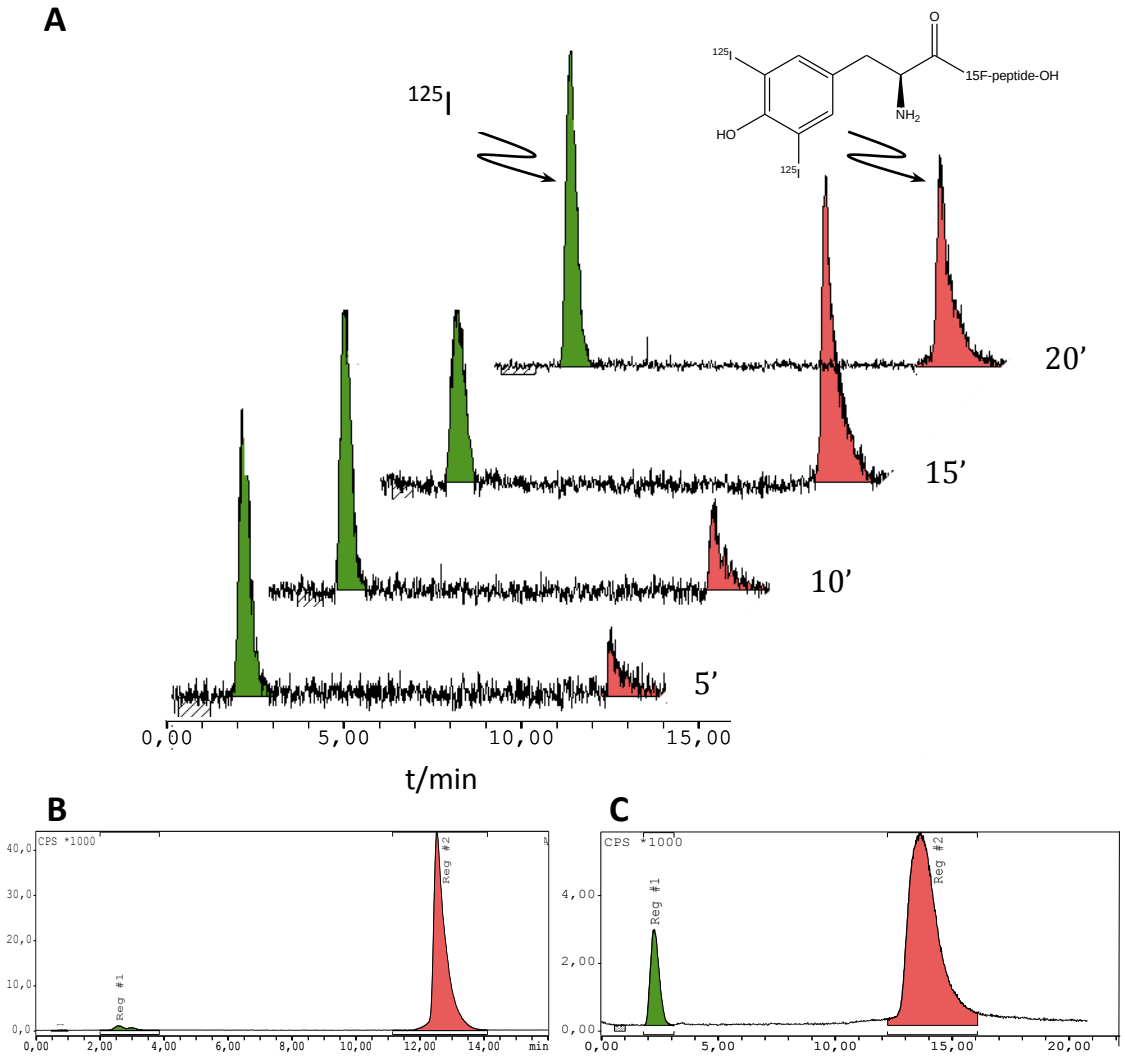


Figure 4.7 Radioactive HPLC characterization of $^{125}$I-15F radiolabeling. (A) Reaction time study, $^{125}$I / $^{125}$I-15F ratio analyzed at different incubation times: (a) 5' 78:22, (b) 10' 73:27, (c) 15' 34:66, (d) 20' 53:47. (B) $^{125}$I-15F stability test after 24 h; (C) $^{125}$I-15F-2P

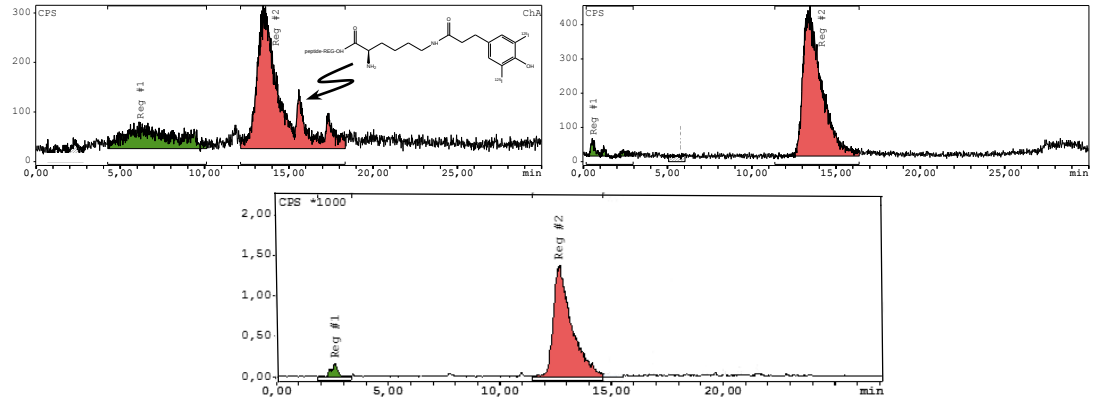


Figure 4.8 Radioactive HPLC characterization of $^{125}$I-REG radioactive detection HPLC. Top left: $^{125}$I / $^{125}$I-REG ratio analyzed at 15 minutes incubation time: 23 / 77; top right: $^{125}$I-REG stability test after 24h; bottom: $^{125}$I-REG-2P

### Characterization of $^{125}$I-15F-NPs and $^{125}$I-REG-NPs

Activity of $^{125}$I-15F and $^{125}$I-REG-NPs, obtained by following the nanoprecipitation protocol describe in Chapter III and employing radiolabeled-peptide 2Ps, was measured before animal injections and ranged in 150-150 μCi. According to the measurements of particle size and zeta potential, the incorporation of the radiolabel did not result in statistically significant alteration of the physic-chemical properties of the resulting NPs; all the formulations exhibited average diameters and zeta-potential values within the required specifications (data not shown).

## 4.3.3 *In vivo* and *ex vivo* experiments

### *In vivo* biodistribution in rats (PET-CT Imaging)

*In vivo* biodistribution studies using PET imaging were carried out using the labelled NPs following strategy 2 (this is, using [$^{18}$F]3P as labelled precursor). This decision was made based on radiochemical yields during particle preparation (see Table 4.1). The labelled precursors (namely [$^{18}$F]FBBA and [$^{18}$F]3P) were also investigated as controls. PET images (Figure 4.9) were acquired after NPs injections and quantified as shown in Figure 4.10. As expected, a pronounced lower uptake of the NPs in the liver than kidneys was ascertained. Renal excretion of the NPs became the favorite way when the surrounding PEG corona on the surface avoids rapid blood clearance through liver accumulation [18,19]. Moreover, a marked renal uptake for 3P block co-polymer (Figure 4.11 A) was found during first 20 minutes, which confirms that although PEG presence, low molecular weight block co-polymers tended to renal excretion more than high molecular weight polymers[11].

Approximately constant uptake in organs in the first 2 hours (Figure 4.10) demonstrated no phagocytosis of the circulating NPs by the RES components of the liver. In this way, NPs blood circulation half-life can be increased and a prolonged blood circulation can result in a higher uptake by targeted tissue.

The stealth character of the NPs was confirmed by the higher liver uptake for the $^{18}$F-FBBA used as control, compared to NPs and 3P (Figure 4.11 B). This can be attribute to the lack of hydrophilic chains (PEG) in $^{18}$F-FBBA compound along with its high hydrophobicity. After liver accumulation, the excretion occurs across hepatocytes through the biliary production pathway. Hepatocytes have been shown to have phagocytic ability, although they are not as effective as Kupffer cells in capturing nanoparticles. Furumoto et al. [20] have found that polystyrene nanoparticles are taken up by both Kupffer cells and hepatocytes after intravenous administration.

As was observed by many authors, nanoparticulate systems could produce hepatotoxicity because normally accumulate in liver[11]. This behavior can be attributed to the conjugate's negative superficial charge, which favors the interaction with the RES. When the NPs are administered, a variety of plasma proteins (e.g. opsonins) bind to their surfaces. The conjugates can then be recognized by the macrophage cell surface and internalized, leading to a significant loss of NPs from circulation. Although negative superficial charge of the developed peptide-functionalized-NPs, opsonization and consequently liver accumulation was clearly avoided thanks to stealthy behaviour awarded to nanoparticulate system.

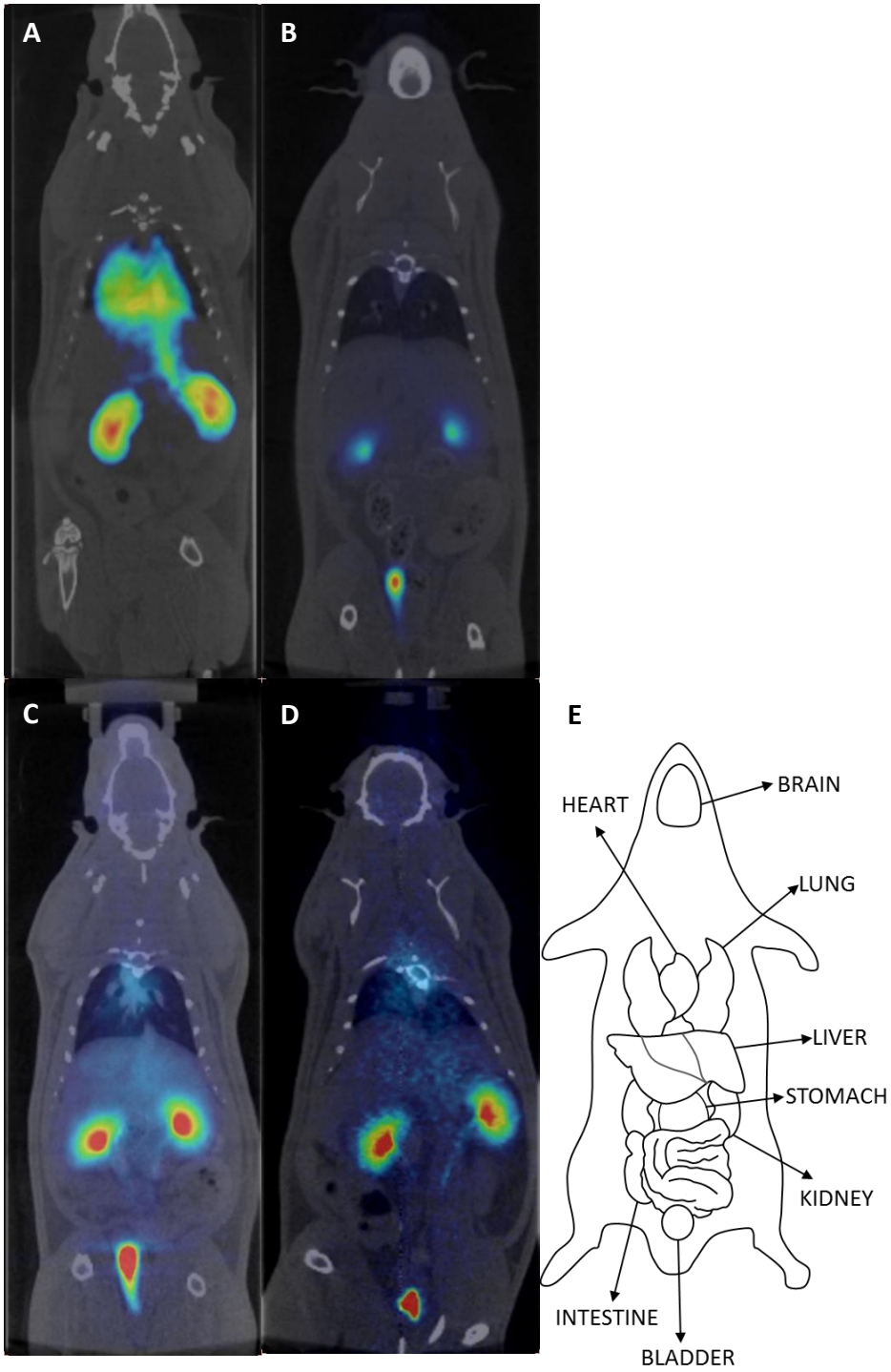


Figure 4.9 Representative PET-CT image (coronal view) for the first frame acquired after an intravenously injection of (A)$^{18}$F-FBBA, (B) $^{18}$F-PEGthiolAcid, (C) $^{18}$F-3P, (D) $^{18}$F-NPs(1), (E) $^{18}$F-NPs(2) and (F) schematic anatomical overview with localization of important organs.

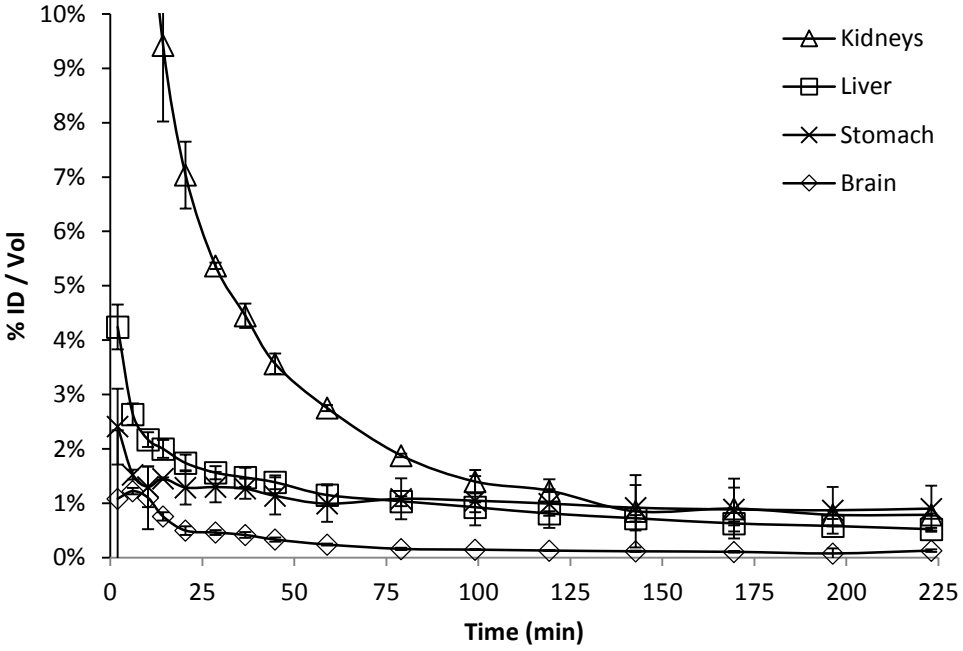


Figure 4.10 Time-activity curves of the defined organs after intravenous injection of $^{18}$F-Peptide-functionalized-NPs

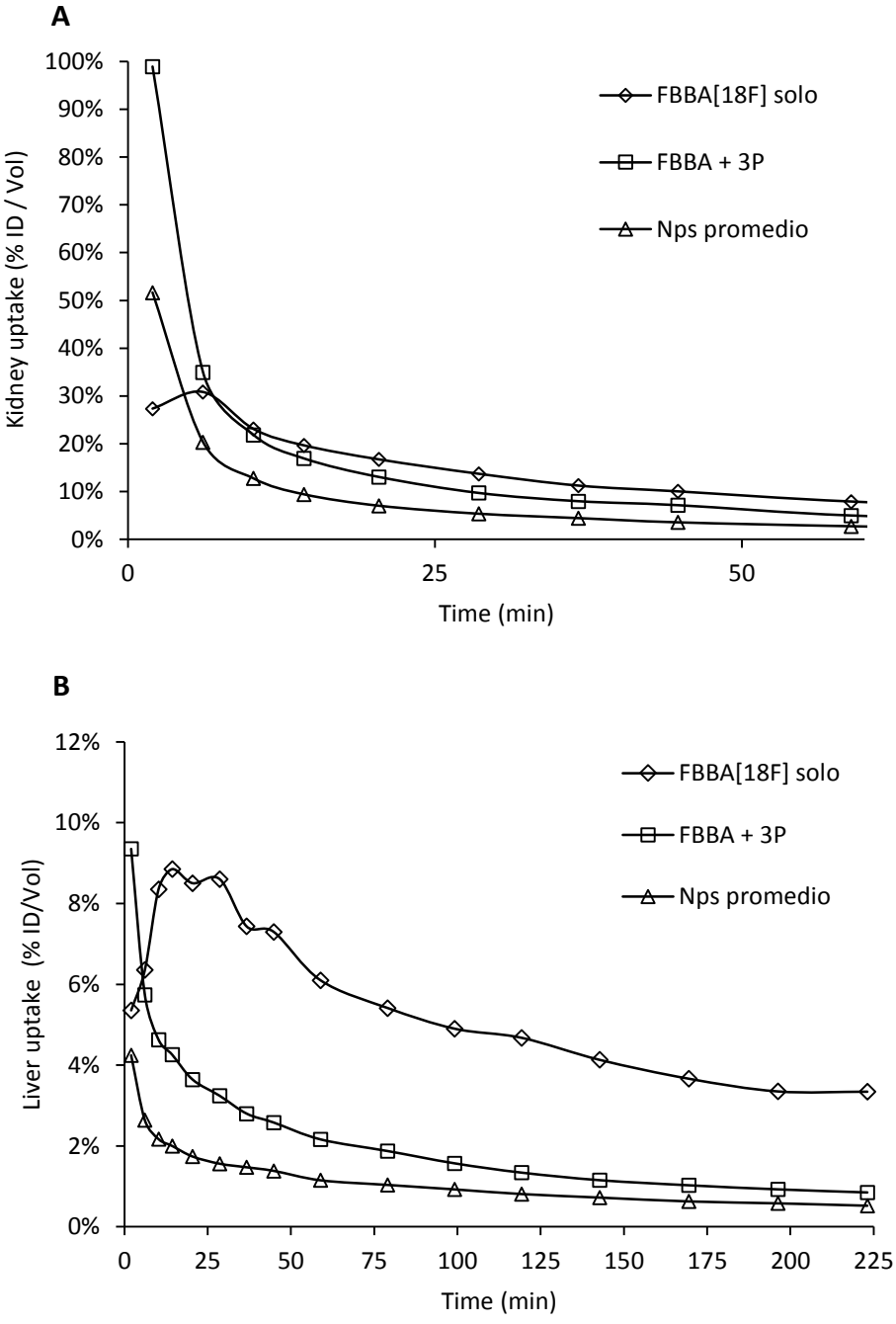


Figure 4.11 Time activity curves of $^{18}$F-Peptide-NPs, $^{18}$F-FBBA and $^{18}$F-3P in (A) kidney and (B) liver

## *Ex vivo* Pharmacokinetics and biodistribution in rats (Gamma-counter)

*In vivo* biodistribution studies were performed by measuring the amount of radioactivity in blood samples and harvested organs at 2, 5 and 10 minutes post-injection. Exsanguination with perfusion after collection of the blood samples was applied to remove the contribution from the radioactivity present in the blood during determination of the radioactivity in the organs. As can be observed in Figure 4.12 A, $^{125}$I-15F-NPs distribution detected in liver and blood showed similar value to that of $^{125}$I-15F at each time point. The concentration of radioactivity in the blood decreased slowly, and a similar trend was found in the liver. Highest % ID/g of $^{125}$I-15F-NPs counted in the kidney was probably due to the low Mw of block co-polymers that tended to renal excretion more than high Mw polymers [11]. The kidney is capable of rapidly removing molecules from the vascular compartment mostly as the injected forms and therefore, renal excretion represents a desirable pathway for NP removal with minimal catabolism. The higher levels of uptake in the kidney in comparison to the liver confirmed that the hepatobiliary system represents the primary route of excretion for NPs that do not undergo renal clearance [21]. This confirmed the results of the biodistribution studies and proved the stealthy behaviour of NPs owing to external hydrophilic coating, which allowed avoid recognition by reticuloendothelial system and so rapid blood clearance through liver accumulation. Moreover, the liver is a major excretion route for larger NPs (>250 nm) [22]. A significant uptake of $^{125}$I-15F in kidney was observed and according to previously reported findings by Vegt et al., radiolabeled peptides, including small fragments are excreted primarily via the kidneys because of accumulation mainly in the renal cortex [23]. As expected, lower kidney uptake of $^{125}$I-15F-NPs in comparison with peptide alone was observed due to the presence of PEG-corona; the insertion of 2- to 4-kDa PEG groups reduces indeed the renal uptake [18,19]. Ex vivo biodistribution in brain revealed an uptake of 0.06 and 0.04 % ID/g for $^{125}$I-15F and $^{125}$I-15F-NPs, respectively (Figure 4.12 B) with higher concentration in cerebellum with respect to the brain (Figure 4.12 C, D). To study the influx of radiolabeled peptides and NPs across the BBB, multiple-time regression analysis was used. The unidirectional influx rate (Ki) and clearance from blood (CL) for $^{125}$I-15F and $^{125}$I-15F-NPs

are shown in Table 4.2. The blood-to-brain entry data corresponding to 125I-labeled compounds are plotted in Figure 4.13 as expressed in eq XX. 15F and 15F-NPs showed linear, unidirectional uptake into brain with BBB transfer coefficients (Kin) of 4.52 ± 0.2 and 1.5 ± 0.016 µl/g·min, respectively. Using 15F peptide, known to be able to cross the BBB, as positive control, we consider satisfactory the ~ 3 fold lower Kin of $^{125}$I-15F-NPs as compared to $^{125}$I-15F. Comparable values of clearance of $^{125}$I labeled compounds from blood were found (Figure 4.13) and consequently similar values of $t_{1/2}$ were obtained (Table 4.2). Biodistribution of $^{125}$I-REG (Figure 4.14) showed lower values of % ID/g in kidney, brain and blood than $^{125}$I-15F along with an increased accumulation in the liver. Unlike $^{125}$I-15F, low levels in blood and high levels in liver suggested a rapid blood clearance through liver accumulation with the hepatobiliary system as predominant route of excretion of NPs. $^{125}$I-REG-NPs showed similar uptake levels to those found for $^{125}$I-15F-NPs. Instead, the uptake in the brain was 6 fold lower (0.006 %ID/g). Multiple-time regression analysis (Figure 4.15) confirmed lower entrance of these in the brain with Ki values of 1.7±0.4 and 0.44 ± 0.1 for $^{125}$I-REG and $^{125}$I-REG-NPs, respectively. Moreover, in concordance with biodistribution data (high accumulation of REG in the liver and consequently low level in blood), low $t_{1/2}$ (4 ± 0.9) and high clearance (12.6 ± 1.7) values were obtained (Table 4.2). Since REG peptide is able to cross BBB just like 15F and in the light of the low values of REG blood-to-brain data entry, we hypothesized an alteration of the transcytosis ability of the REG peptide due to the radionuclide insertion in the lysine residues. Indeed, the rigid β-hairpin structure and the area of the flexible region including residues R13, R19, K20 and K22, that are supposed interact with the LA domain of LDLR family, both contains lysine residues. Moreover, the alteration of lysine probably decreases hydrophylicity of the REG peptide, as reflected in a dramatically increased liver uptake and retention [18].

Table 4.2 Pharmacokinetic parameters of $^{125}I$ labeled and peptides-functionalized NPs after iv administration in rats

| **Formulation** | **$K_i$ (µl/g·min)** | **$t_{1/2}$ (min)** | **CL (ml/min)** |
|---|---|---|---|
| 15F | 4.52 ± 0,2 | 6 ± 0,42 | 2,1 ± 0,3 |
| 15F-NPs | 1.5 ± 0.016 | 4,35 ± 1,6 | 2,66 ± 0,21 |
| REG | 1,7 ± 0,4 | 4 ± 0,9 | 12,6 ± 1,7 |
| REG-NPs | 0,44 ± 0,1 | 10,6 ± 2,6 | 1,5 ± 0,55 |

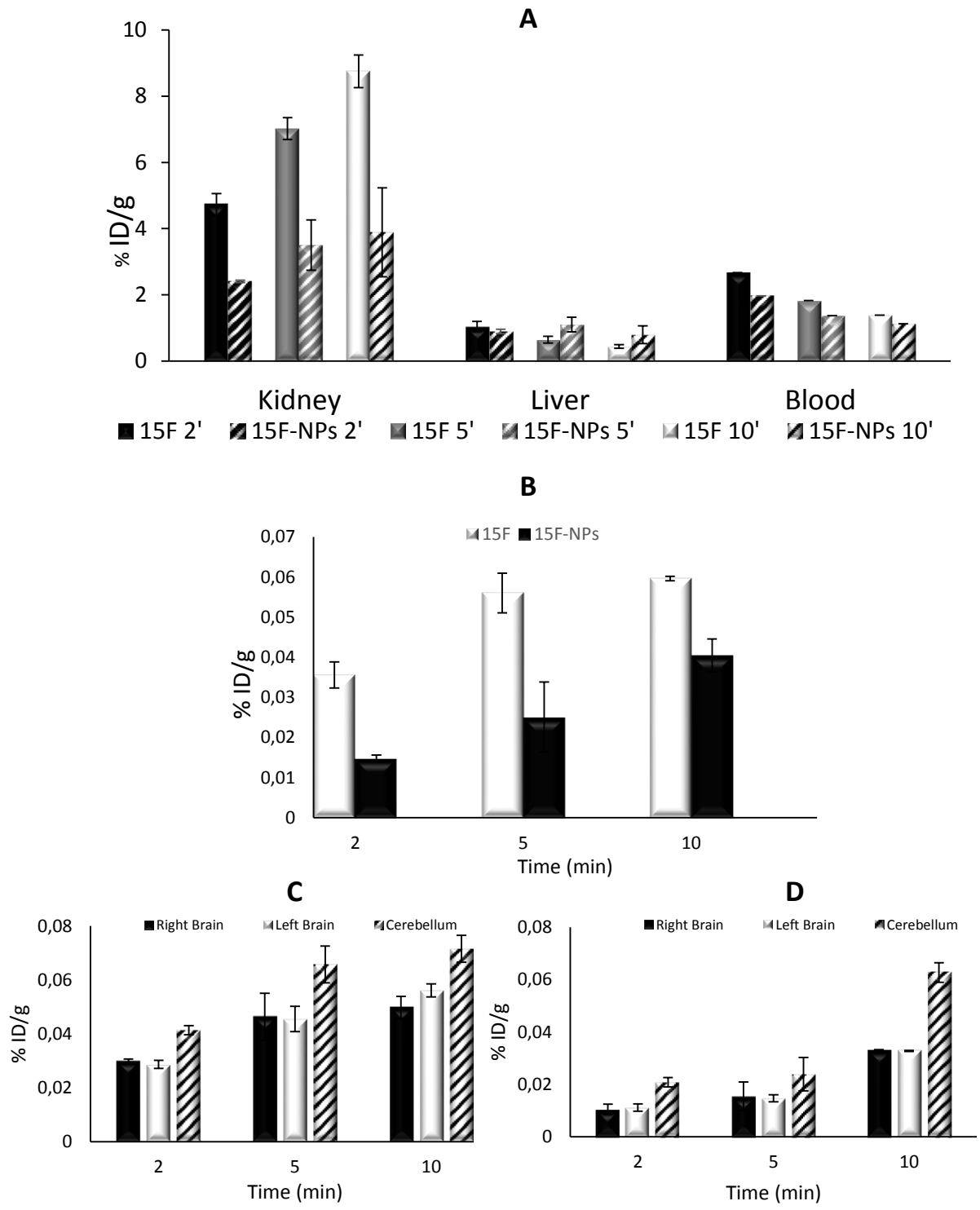


Figure 4.12 $^{125}$I-15F and $^{125}$I-15F-NPs biodistribution in mouse organs, harvested from each animal after exsanguination, washed with clean buffer saline and measured by scintillation counting to determinate total associated radioactivity. (A) kidney, liver, blood, plasma; (B) whole brain; (C) $^{125}$I-15F and (D) $^{125}$I-15F-NPs biodistribution in right, left brain and cerebellum

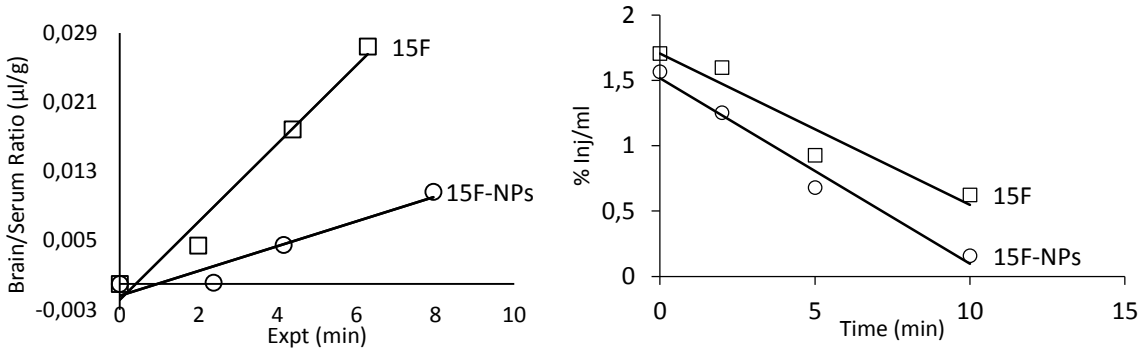


Figure 4.13 Multiple-time regression analysis for 15F and 15F-NPs. (Left) Blood-to-brain entry of $^{125}$I-15F and $^{125}$I-15F-NPs into mouse brain after iv administration. The slope of the regression line between brain/serum ratio and exposure time is $K_i$ (µl/g·min), the unidirectional influx rate reflecting blood-to-brain entry. (Right) Drug Clearance (DC) from blood of $^{125}$I-15F and $^{125}$I-15F-NPs; the half-time disappearance ($t_{1/2}$) calculated from the slope, and the volume of distribution calculated from the intercept of the resulting line (Data are shown in Table 4.2, expressed as means ± SD)

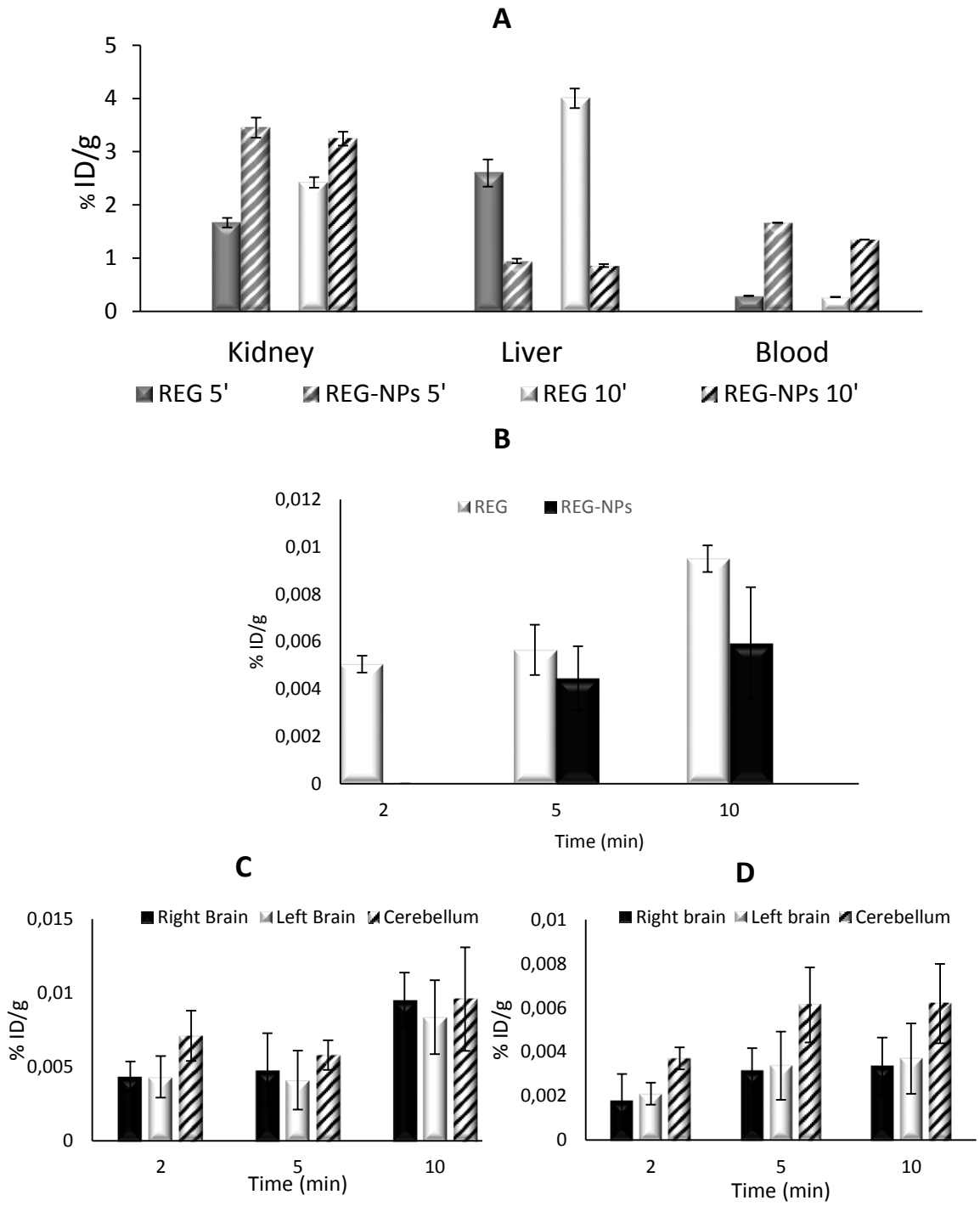


Figure 4.14 $^{125}$I-REG and $^{125}$I-REG-NPs biodistribution in mouse organs harvested from each animal after exsanguination, washed with clean buffer saline and measured by scintillation counting to determinate total associated radioactivity. (A) kidney, liver, blood, plasma; (B) whole brain; (C) $^{125}$I-REG and (D) $^{125}$I-REG-NPs biodistribution in right, left brain and cerebellum

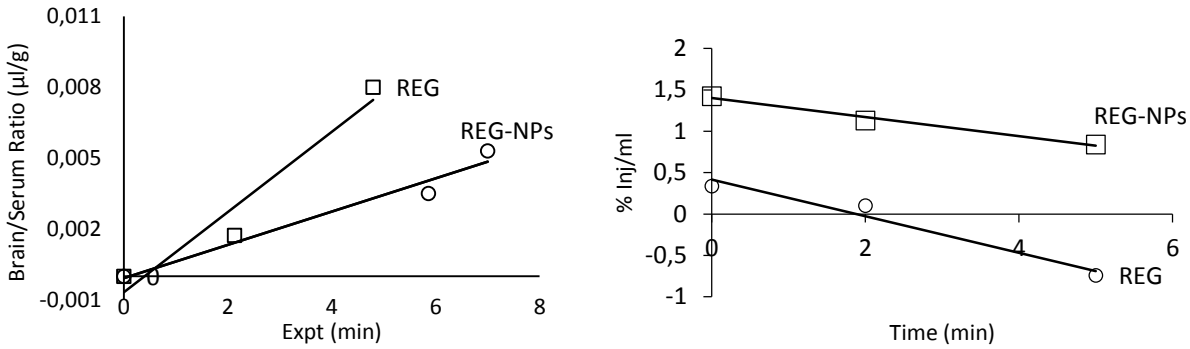


Figure 4.15 Multiple-time regression analysis for REG and REG-NPs. (Left) Blood-to-brain entry of 125I-REG and 125I-REG-NPs into mouse brain after iv administration. The slope of the regression line between brain/serum ratio and exposure time is Ki (µl/g·min), the unidirectional influx rate reflecting blood-to-brain entry. (Right) Drug Clearance (DC) from blood of 125I-REG and 125I-REG-NPs; the half-time disappearance (t1/2) calculated from the slope, and the volume of distribution calculated from the intercept of the resulting line (Data are shown in Table 4.2, expressed as means ± SD)

## 4.4 Concluding remarks

This chapter describes and discusses various approaches and methods for the radiolabelling of NPs for PET-CT imaging and gamma counting, respectively, using radionuclide positron and gamma emitters. These techniques represent an ideal tool for investigations of pharmacological profiles of the drug delivery system.

Since new approaches need to be explored for investigate the *in vivo* fate of the NPs, this chapter give rise to a new strategy for conjugation of polymeric NPs with $^{18}F$ for non-invasive imaging by means of PET. Otherwise, NPs radiolabelling through peptide conjugation, was also performed with $^{125}I$ because its high specific radioactivity allows to measure very low concentrations of the substance under investigation.

*In vivo* and ex vivo pharmacokinetics and biodistribution studies in rats performed injecting by iv bolus, radiolabeled NPs, have allowed a semi-quantitative measurement of the organ biodistribution of the system in mice. Both NPs formulations, functionalized with 15F and REG, showed stability in biological environments with no accumulation in liver and low accumulation in kidney. This stealthy behaviour of NPs is due to external hydrophilic coating that allows avoid recognition by reticuloendothelial system and so rapid blood clearance through liver accumulation. In this way, NPs blood circulation half-life was increased and organs uptake 2 hours after injection was found slightly lower than after 20 minutes. This prolonged blood circulation is a promising result because it can result in a higher uptake by targeted tissue.

Additionally, a special attention was given to quantitatively brain uptake of NPs by using a theoretical model of blood-brain exchange. The pharmacokinetic study was carried out to

study the influx of the radiolabeled and peptides functionalized NPs across the BBB after injection. Multiple-time regression analysis was adapted to assess the fraction of the administered dose that is distributed within the BBB complex or is excreted from the body, based on a two-compartment mathematical model. 15F-NPs showed satisfactory values of penetration into brain tissues as compared to peptides known to be efficiently transported across the BBB. Along with unidirectional influx rate, comparable values of clearance from blood and consequently similar values of $t_{1/2}$ were found.

On the other hand, biodistribution of REG-NPs in liver and kidney showed similar uptake levels to those found for 15F-NPs but on the contrary, the uptake in the brain was rather lower. In the light of the low values of REG-NPs blood-to-brain data entry obtained by *in vivo* and ex vivo studies, we hypothesized an alteration of the transcytosis ability of the REG peptide due to the radionuclide insertion in the lysine residues.

The promising results obtained evaluating the potential of the peptide functionalized NPs as brain targeting drug delivery system, along with the possibility to select the target by functionalizing NPs with any family of peptides, suggested that the nanoparticulate system might have great potential for glioma therapy in clinical applications. Next chapter (Chapter V) presents the impact that the developed nano-platform had in terms of contribution and innovation in our research group. The outcome was the foundation of a company, Sagetis Biotech, devotes to developing innovative drug delivery technologies and with the aim to improve our system and to explore new possible applications for the unmet medical needs.

## 4.5 References


1. D. E. Owens and N. a Peppas, Opsonization, biodistribution, and pharmacokinetics of polymeric nanoparticles., Int. J. Pharm. 307**,** 93–102 **(2006)**

2. S. M. Moghimi, a C. Hunter and J. C. Murray, Long-circulating and target-specific nanoparticles: theory to practice., Pharmacol. Rev. 53**,** 283–318 **(2001)**

3. M. H., The enhanced permeability and retention (EPR) effect in tumor vasculature: the key role of tumor-selective macromolecular drug targeting., Ad. Enzym. Regul 41**, (2001)**

4. D. R., in Encycl. Mol. Cell Biol. Mol. Meidicne edited Wiley-VCH, 163–203 **(**2005**)**

5. X. J. Feng Xu, Wei Lu, Hongbing Wu, Li Fan, Xiaoling Gao, Brain delivery and systemic effect of cationic albumin conjugated PLGA nanoparticles, J. Drug Target. 17**,** 423–434 **(2009)**

6. L. Costantino, F. Gandolfi, G. Tosi, F. Rivasi, M. A. Vandelli and F. Forni, Peptide-derivatized biodegradable nanoparticles able to cross the blood-brain barrier., J. Control. Release 108**,** 84–96 **(2005)**

7. et al. Ke W, Shao K, Huang R, Han L, Liu Y, Li J, Gene delivery targeted to the brain using an Angiopep-conjugated polyethyleneglycol-modified polyamidoamine dendrimer, Biomaterials 30**,** 6976–85 **(2009)**

8. et al. Huang R, Ke W, Han L, Liu Y, Shao K, Jiang C, Lactoferrin-modified nanoparticles could mediate efficient gene delivery to the brain in vivo, Brain Res Bull 81**,** 600–4 **(2010)**

9. T. Reiner, E. J. Keliher, S. Earley, B. Marinelli and R. Weissleder, Synthesis and in vivo imaging of a 18F-labeled PARP1 inhibitor using a chemically orthogonal scavenger-assisted high-performance method., Angew. Chem. Int. Ed. Engl. 50**,** 1922–5 **(2011)**

10. B. E. O.-G. and F. de M. R. Enrique Morales-Avila, Guillermina Ferro-Flores, in Mol. Imaging edited Prof. Bernhard Schaller (Ed.), 15–38 **(**2012**)**

11. K. Stockhofe, J. M. Postema, H. Schieferstein and T. L. Ross, Radiolabeling of Nanoparticles and Polymers for PET Imaging., Pharmaceuticals (Basel). 7**,** 392–418 **(2014)**

12. N. K. Devaraj, E. J. Keliher, G. M. Thurber, M. Nahrendorf and R. Weissleder, 18F labeled nanoparticles for in vivo PET-CT imaging., Bioconjug. Chem. 20**,** 397–401 **(2009)**

13. R. H. S. and R. E. Counsell, Radioiodination techniques for small organic molecules, Chem. Rev. 82**,** 575–590 **(1982)**

14. R. G. Blasberg, J. D. Fenstermacher and S. Patlak, Transport of α-Aminoisobutyric Acid Across Brain Capillary and Cellular Membranes, 8–32 **(1983)**

15. C. S. Patlak, R. G. Blasberg and J. D. Fenstermacher, Graphical evaluation of blood-to-brain transfer constants from multiple-time uptake data., J. Cereb. Blood Flow Metab. 3**,** 1–7 **(1983)**

16. I. van Rooy, S. Cakir-Tascioglu, W. E. Hennink, G. Storm, R. M. Schiffelers and E. Mastrobattista, In vivo methods to study uptake of nanoparticles into the brain., Pharm. Res. 28**,** 456–71 **(2011)**

17. B. Kuhnast, S. Klussmann, F. Hinnen, R. Boisgard, B. Rousseau, J. P. Frste, B. Tavitian and F. Doll, Fluorine-18- and iodine-125-labelling of spiegelmers, J. Label. Compd. Radiopharm. 46**,** 1205–1219 **(2003)**

18. X. Chen, R. Park, A. H. Shahinian, J. R. Bading and P. S. Conti, Pharmacokinetics and tumor retention of 125I-labeled RGD peptide are improved by PEGylation, Nucl. Med. Biol. 31**,** 11–19 **(2004)**

19. Z. Wu, Z.-B. Li, W. Cai, L. He, F. T. Chin, F. Li and X. Chen, 18F-labeled mini-PEG spacered RGD dimer (18F-FPRGD2): synthesis and microPET imaging of alphavbeta3 integrin expression., Eur. J. Nucl. Med. Mol. Imaging 34**,** 1823–31 **(2007)**

20. H. Furumoto, K., Ogawara, K., Yoshida, M., Takakura, Y. and T. M., Higaki, K., and Kimura, Biliary Excretion of Polystyrene Microspheres Depends on the Type of Receptor-Mediated Uptake in Rat Liver, Biochim. Biophys. Acta 1562**,** 221–226 **(2001)**

21. P. D. . Michelle Longmire, Peter L. Choyke, M.D., and Hisataka Kobayashi, M.D., Clearance Properties of Nano-sized Particles and Molecules as Imagin Agents: Consideration and Caveats, 3**,** 703–717 **(2012)**

22. S. Guerrero, J. R. Herance, S. Rojas, J. F. Mena, J. D. Gispert, G. a Acosta, F. Albericio and M. J. Kogan, Synthesis and in vivo evaluation of the biodistribution of a 18F-labeled conjugate gold-nanoparticle-peptide with potential biomedical application., Bioconjug. Chem. 23**,** 399–408 **(2012)**

23. E. Vegt, M. de Jong, J. F. M. Wetzels, R. Masereeuw, M. Melis, W. J. G. Oyen, M. Gotthardt and O. C. Boerman, Renal toxicity of radiolabeled peptides and antibody fragments: mechanisms, impact on radionuclide therapy, and strategies for prevention., J. Nucl. Med. 51**,** 1049–58 **(2010)**

# CHAPTER V.

## Impact, applications and possible trends

This work gives rise to a new system capable to solve some of the major bottlenecks found in polymeric nanoparticulate systems designed for brain targeting drug delivery.

The novel drug delivery platform described in this thesis represents an efficient term for comparison with the mainly used nanoparticles system based in PLA-PLGA. Although NPs are composed by two or more different polymers (P, 2P or 3P), the preparation method is simplified and it is carried out in only one step and without emulsifier.

The polymer used is new and its special characteristics and innovative character lead to a considerable improvement in drug loading and in controlled release.

The considerable increase of PTX encapsulated into nanocarriers makes the system suitable for intravenous administration since no very concentrated solutions can be injected. Specifically, the high drug contents achieved are an absolute novelty for block polyester-based nanoparticles. Similar values of PTX cargo are accomplished by other authors, employing polyester block copolymers, but for micellar carriers [1]. The use of drug-loaded polymeric micelles is limited by their low stability in aqueous solution; stability that becomes even lower when the drug loading content increases [2]. The poor stability also was remarked in blood as well as insufficient binding and uptake by cells [3]. The inherent instability of micelles, along with their rapid clearance from circulation remains a significant challenge.

[1] G. Gaucher, R. H. Marchessault and J.-C. Leroux, Polyester-based micelles and nanoparticles for the parenteral delivery of taxanes., J. Control. Release 143, 2–12 (2010)

[2] H. M. Burt, X. Zhang, P. Toleikis, L. Embree and W. L. Hunter, Development of copolymers of poly ( D , L -lactide ) and methoxypolyethylene glycol as micellar carriers of paclitaxel, 16, 161–171 (1999)

[3] S. C. Owen, D. P. Y. Chan and M. S. Shoichet, Polymeric micelle stability, Nano Today 7, 53–65 (2012)

For many polyester-based NPs such as for polymeric micelles, very fast complete release or biphasic profile characterized by burst release, is frequently observed [4, 5, 6]. The release behaviour of PTX from the NPs developed in this work, exhibits an approximately first-order profile, without initial burst, and characterized by a slow and constant release. The improved release profile, along with the possibility to control the release rate by setting the hydrophobic character of the NPs, represents an important advance in the polyester-based NPs systems field.

The flexibility in design of nanoparticle delivery system offers an opportunity to engineer the components based on the desired application. As a result, the surface can be modified with PEG allowing to reduce nonspecific interactions with proteins, resulting in increased blood circulation times.

Moreover, depending on the target, NPs can be easily functionalized with the appropriate family of peptide to enhance cellular uptake and accumulation in tumor tissue through binding and endocytosis.

In this scenario, this whole thesis has sought to demonstrate that peptide functionalized and PTX loaded NPs are promising candidates for glioma therapy in clinical applications, given their loading capacity and efficacious targeting, which improve therapeutic index and avoid the adverse effect of an uncontrolled release.

[4] Q. Hu, G. Gu, Z. Liu, M. et al., F3 peptide-functionalized PEG-PLA nanoparticles co-administrated with tLyp-1 peptide for anti-glioma drug delivery., Biomaterials 34, 1135–45 (2013)

[5] X. He, J. Ma, A. E. Mercado, W. Xu and E. Jabbari, Cytotoxicity of Paclitaxel in biodegradable self-assembled core-shell poly(lactide-co-glycolide ethylene oxide fumarate) nanoparticles., Pharm. Res. 25, 1552–62 (2008)

[6] H. Xin, L. Chen, J. Gu, X. et al., Enhanced anti-glioblastoma efficacy by PTX-loaded PEGylated poly(ε-caprolactone) nanoparticles: In vitro and in vivo evaluation., Int. J. Pharm. 402, 238–47 (2010)

The degree of contribution and innovation of this work paved the way to the birth of a company, *Sagetis Biotech*, devotes to developing innovative drug delivery technologies. Starting from the results here obtained, *Sagetis Biotech* put a great deal of effort into this project to improve the system with the aim to lead up the polymeric drug delivery platform to the clinical trials.

First requirement, in view of the scaling up the process, consisted in plentiful raw materials to be employed for production in industry. The fabrication methods needed to be modified and adapted to the large-scale production. To perform the scaling up, *Sagetis Biotech* decided to synthetize polymers without microwave to obtain most purified starting materials. Thanks to key partners for animal testing, a slightly modified nanoparticulate system, here developed, was further *in vivo* characterized before to start preclinical research. Pharmacodynamics, pharmacokinetics, ADME and toxicity studies through animal testing are currently in progress.

Thanks to the flexibility in the design, the technology here developed has proved to be similarly efficient in other fields different from brain delivery. The same base components, engineered as required, have been employed for new applications with the aim to satisfy the unmet medical needs. Among them, a functionalized PDMS surface used as antibacterial coating and able to avoid biofilm formation was customized by modifying the NPs here developed. In view of its use as a tracheal prosthesis, the PDMS surface was functionalized with the drug loading nanoparticulate system to treat scarring tissue or granuloma formation. This promising modification consists in modifying P block co-polymer to obtain superficially aminated NPs that can be easily immobilized on a previously functionalized PDMS substrate.

The wide range of possible applications is due to the flexibility in the design of the developed nanoparticulate system. Potentially, the same technology could be extended to many fields and with different purposes.

A further application of the discussed nano-platform concerns a new mucus-barrier penetrating system that allows NPs to be slippery into the mucus barrier avoiding rapid mucus clearance. Superficially thiolated and PEGylated NPs opens opportunities for the system to be used for targeted drug delivery in mucus-coated areas.

In addition to the impact so considerable as to lead to *Sagetis Biotech* foundation, the proposals of this thesis demonstrate a wide prospective of applications that can be on-demand and easily customized, depending only on the desired application.

# CHAPTER VI.

## Conclusions

A custom-tailored, polymeric drug delivery system for the anticancer drug PTX, intended to be intravenously administered, capable of improving the therapeutic index of the drug and devoid of the adverse effects of an uncontrolled release has been developed, optimized and characterized.

- A novel block co-polymer (P) has been successfully synthetized to obtain via nanoprecipitation or emulsification-solvent evaporation method, a very monodisperse PTX-NPs population. A clear correlation between NPs characteristics and formulation parameters has been found in order to entirely customize NPs in terms of size, zeta-potential, drug loading and release profile.

- PTX-loaded NPs have been proved to be spherical in shape at the desired size and polydispersity ranges and with a surrounding PEG corona on the surface. Due to the strong lipophilic interactions of the drug with the hydrophobic inner region of NPs, PTX content has been considerably increased and its amorphous physical state has been confirmed by DSC.

- *In vitro* experiments have demonstrated that NPs release PTX with an approximately first-order profile and without initial burst. The total cargo of loaded PTX has been shown to change the hydrophobic character of the NPs, allowing to set the release profile in a modulated and controlled way. Biocompatibility and *in vitro* anti-tumoral activity against a human primary glioblastoma cell line have been assessed. It has been also demonstrated that the cytotoxicity against tumoral cells is time- and drug concentration-dependent.

PTX loaded NPs have been satisfactorily functionalized with an appropriate family of peptides for dual-targeting purposes to shuttle drug from across the BBB, and then target glioma cells.

- A novel biodegradable block co-polymer (2P) has been successfully synthetized and in combination with P, has been employed to produce in one step and via modified nanoprecipitacion emulsifier-free method, a very monodisperse peptide functionalized and PTX loaded NPs population. High drug loading and *in vitro* PTX controlled release have been also corroborated.

- The functionalization of NPs has been carried out employing a family of peptides known to be efficiently transported across BBB by a membrane receptor (LRP) that also is over-expressed on human glioma cells. Crosslinking via sulfhydryl groups has been assessed as method for coupling NPs and peptides.

- The developed strategy has proved to induce cellular uptake by active transport both in endothelial cells and glioma cells.

- *In vitro* co-localization experiments performed on human primary glioblastoma cells suggest that the mechanism used by the peptide-functionalized NPs is LRP-1 dependent.

- The dual-targeting effect has been optimized and an enhanced *in vitro* anti-tumoral activity against glioma cells, compared with non-functionalized-PTX-NPs, has been demonstrated.

- Transcytosis experiments using an *in vitro* BBB model, have demonstrated that a significant increased transendothelial transport ratio of PTX is achieved when the drug is loaded in the peptide functionalized NPs.

The relevant *in vivo* pharmacokinetics, biological profile and biodistribution properties of the developed nanocarriers have been assessed.

- Various novel strategies and methods including the synthesis and purification of the optimized NPs, labeled with radionuclide gamma or positron emitters to perform PET-CT and gamma counting studies, respectively, have been explored.

- *In vivo* and ex vivo characterizations have been carried out through a semi-quantitative measurement of the organ biodistribution. Peptide functionalized NPs can be considered stable in biological environments with a pronounced lower uptake in the liver compared to kidneys. NPs show a stealthy behavior and the approximately constant uptake in major organs demonstrates no phagocytosis of the circulating NPs by the RES components of the liver, suggesting that rapid blood clearance through liver accumulation has been avoided.

- In order to evaluate the potential of peptide functionalized NPs as a brain targeted drug delivery system, special attention has been given to brain uptake by using a theoretical model of blood-brain exchange, with the aim to study the influx of the NPs across the BBB after iv injection. Multiple-time regression analysis, based on a two-compartment mathematical model has evidenced that developed NPs enter the brain with satisfactory levels of penetration when compared to peptides known to be efficiently transported across the BBB. Along with the unidirectional

influx rate, comparable values of clearance from blood and consequently similar values of $t_{1/2}$ have been found. Also, it has been ascertained that when the radionuclide insertion takes place in the peptide regions that are supposed to interact with the BBB receptors, low values of blood-to-brain entry are achieved, hypothesizing an alteration of the transcytosis ability of the labeled peptide.

# List of Publications and Presentations

## Publications and Patents

P. P. Di Mauro and S. Borrós, **Development of High Drug Loaded and Customizing Novel Nanoparticles for Modulated and Controlled Release of Paclitaxel.** *Pharmaceutical Research* (2014)

P. P. Di Mauro, A. Cascante, P. Brugada-Vila , J. Llop , S. Borros, **Peptide-functionalized and high drug loaded novel nanoparticles as dual-targeting drug delivery system for modulated and controlled release of paclitaxel to brain glioma.** *Biomaterials* (submitted)

P. P. Di Mauro, S. Borros, J. LLop **Novel $^{18}$F labeling strategy for polyester-based NPs for *in vivo* PET-CT imaging.** *Bioconjugate Chemistry* (submitted)

S. Borros, P. P. Di Mauro, **Polymeric Nanoparticles for drug delivery.** WO Patent 2012153286, filed May 09, 2012 and issued November 15, 2012

## Seminars and Courses

07/2014 **41st Annual Meeting of the Controlled Release Society (CRS).** Attendee, Chicago, IL, USA.

07/2014 **Neurogune 2014, 2nd Basque Neuroscience meeting.** Poster presentation: Neurotoxicity and brain permeability of targeted polymeric nanoparticles. Gipuzkoa Science and Technology Park, Donostia - San Sebastian, Spain

06/2014 **European Society of Toxicology In Vitro (ESTIV) 2014 International Conference.** Poster presentation: Permeability and toxicological profiles of targeted nanoparticles in Blood-Brain Barrier in vitro models for Brain Drug Delivery. Egmond aan Zee, The Netherlands

05/2013 **EU European Project, Alexander. Citotoxicity Workshop.** Mucus Permeating Nanoparticulate drug delivery System. Institute Jozef Stefan, Ljubljana, Slovenia.

11/2012 **EU European Project, Alexander. Workshop.** Oral and poster presentation: Development of biodegradable polyester nanoparticles for drug delivery to mucosal tissues. Frankfurt, Germany.

05/2012 **European Summit for Clinical Nanomedicine (CLINAM).** Poster Presentation: Design of Targeted Polyester Nanoparticles for Drug Delivery to the Brain. Basel, Switzerland.

02/2012 **12th European Symposium on Controlled Drug Delivery.** Poster Presentation: Design of Targeted Polyester Nanoparticles for Drug Delivery to the Brain. Enschede, The Netherlands.

09/2010 **Summer School of Medicine 2.** "The whole process from ideas to drug, new trends in pharmaceutical innovation" Toulouse, France.